Correlative microscopic characterization of nanoscale assemblies at interfaces

Correlative Microscopic Characterization of Nanoscale Assemblies at Interfaces

PROEFSCHRIFT

ter verkrijging van de graad van doctor aan de Technische Universiteit Eindhoven,
op gezag van de Rector Magnificus prof. dr. ir. F.P.T. Baaijens,
voor een commissie aangewezen door het College van Promoties,
in het openbaar te verdedigen op 15 december 2020 om 13:30 uur

door

Michael Alfonsus Beuwer

geboren te Eindhoven

Dit proefschrift is goedgekeurd door de promotoren en de samenstelling van de promotiecommissie is als volgt:

voorzitter:	prof. dr. ir. G. M. W. Kroesen
1e promotor:	dr. ir. P. Zijlstra
copromotor:	prof. dr. ir. M. W. J. Prins
leden:	prof. dr. ir. I. K. Voets
	prof. dr. M. Fleischer (Eberhard Karls Universität Tübingen)
	prof. dr. ir. S. J. T. van Noort (Universiteit Leiden)
	prof. dr. E. W. Meijer

Het onderzoek of ontwerp dat in dit proefschrift wordt beschreven is uitgevoerd in overeenstemming met de TU/e Gedragscode Wetenschapsbeoefening

"Growth comes at the point of resistance. Skills come from struggle."
- Steve Magness

Correlative microscopic characterization of nanoscale assemblies at interfaces
Eindhoven University of Technology, 2020

Cover design by M. A. Beuwer

A catalogue record is available from the Eindhoven University of Technology Library
ISBN: 978-94-641-9072-4

EINDHOVEN UNIVERSITY OF TECHNOLOGY

ICMS INSTITUTE FOR COMPLEX MOLECULAR SYSTEMS

Abstract

All imaging methods have their own advantages and disadvantages. Depending on the system and aim of the experiment the optimal method is often selected. In this thesis we combine orthogonal imaging methods to further enhance the amount of information that can be extracted from a sample. We particularly integrate atomic force microscopy (AFM), fluorescence and scattering microscopy, and optical spectroscopy into a single instrument. We used this integrated instrument to study the correlation between optical and structural properties of both soft and hard self-assembled materials.

In **Chapter 2** the setup is described, as well as a comparison of spectroscopic techniques and a thorough description of different available AFM modes. We combine these methods for correlated measurements and describe the alignment procedure and the model systems investigated in this thesis.

In **Chapter 3,** we describe how our correlated setup is applied to soft supramolecular polymers. Using correlated microscopy we study fiber-entanglement by relating fluorescence intensity variations to nanometer scale structure. The persistence length, or stiffness, of the polymers is analyzed for the single unentangled polymers and compared to a model.

Chapter 4 and **Chapter 5** discuss self-assembled gold nanoparticle dimers and relate their structure to their optical properties. When used as biosensors, the plasmon shift not only depends on the size and refractive index of the analyte, but also strongly on binding location. In **Chapter 4 w**e show the correlation between binding location and plasmon shift for single nanospheres binding to a single gold nanorod. For nanorod dimers the enhanced near-field in the gap region is stronger than for single rods. In **Chapter 5** we investigate the optical properties of self-assembled nanorod dimers and investigate the bonding and antibonding mode as a function of dimer angle. We find that the theoretical refractive-index sensitivity of nanorod dimers is not reached, because of limited accessibility of the gap region due to steric effects of the linker molecules.

Chapter 6 summarizes the findings of the thesis, discusses the impact for applications, and lists directions for further research.

List of abbreviations

Abbreviation	Meaning
AFM	Atomic Force Microscope
APTES	(3-aminopropyl)triethoxysilane
BEM	Boundary Element Method
BTA	1-3-5,-Benzenetricarboxamide
CM	Contact Mode
CMOS	Complementary Metal-Oxide-Semiconductor
Cryo-EM	Cryo-Electron Microscope
CTAB	Cetyl Trimethyl Ammonium Bromide
EM	Electron Microscope
EMCCD	Electron Multiplying Charge Coupled Device
FoM	Figure of Merit
LSPR	Longitudinal Surface Plasmon Resonance
MTPMS	(3-mercaptopropyl)trimethoxysilane
NCM	Non-Contact Mode
OM	Optical Microscopy
PALM	Photo Activated Localization Microscopy
PFTM	Peak Force Tapping Mode
RIU	Refractive Index Unit
STED	Stimulated Emission Depletion
STORM	Stochastic Optical Reconstruction Microscopy
STM	Scanning Tunneling Microscope
SPR	Surface Plasmon Resonance
TIR	Total Internal Reflection
TIRF	Total Internal Reflection Fluorescence

Contents

Chapter 1

Introduction

1.1 History of microscopy

Already in the 13th century lenses in the form of water-filled glass spheres were used to magnify objects by gem cutters. In the 17th century Robert Hooke used glass balls as lenses with a much shorter focal length to observe microscopic fungi. He later developed a microscope that had two convex lenses and used it to study biological species like sponges, fungi, flies, and lice. His detailed observation of these organisms with an early microscope were catalogued in the first illustrated book on microscopy named "micrographia".[1] Hooke's superb drawings with never observed details of microscopic species gave him a place in the history of science.

Around the same time Antoni van Leeuwenhoek was the first to observe bacteria using a single-lens microscope. He developed the ability to make very small lenses (only 1 mm in diameter) that were embedded in a small metal plate. The sample was placed on a small pin positioned on a screw that enabled Van Leeuwenhoek to position and focus the sample close to the lens. The magnifications that he achieved were approximately 250, depending on the quality of the lens. He used this single-lens microscope to describe for the first time bacteria, the human fertilization process, and red blood cells.

From then on the field gradually developed by the introduction of better lenses, and microscopes employing multiple lenses achieved higher magnifications. The craftmanship to keep improving the quality of the lenses and decrease aberration effects led to diffraction limited microscopes that we use in research labs since the early 20th century. Diffraction limited microscopes achieve magnifications of up to 1000x, and optical resolutions of a few hundred nanometers. This is enough to resolve for example biological cells, bacteria, and dust.

The urge to visualize even smaller structures is however hindered by the diffraction limit of light, which sparked the development of complementary techniques based on different approaches. A key event was the development of the electromagnetic lens in 1926 by Hans Busch. This electromagnetic lens uses several electromagnets to focus a stream of charged particles such as electrons by the Lorentz force. The first prototype electron microscope, with 400x magnification, was developed in 1931 by Ernst Ruska and Max Knoll.[2]

Electron microscopes achieve a higher resolution than optical microscopes by using electrons as the illumination source, which exhibit a shorter wavelength (the so-called De Broglie wavelength) compared to photons. The wavelength of the incident electrons depends inversely on the energy to which the electrons are accelerated in the microscope. Typical electron microscopes use acceleration voltages of several hundreds of kilovolt, leading to an illumination wavelength of several picometers. This provides electron microscopes with a resolution of around 1 picometer, enabling imaging at the atomic level.

With the invention of the scanning tunneling microscope (STM) in 1981 the elusive goal of imaging individual atoms on opaque surfaces was achieved.[3] STM uses a very sharp conducting tip brought very near to a surface and monitors the tunneling current as a function of tip position as the tip's position scans across the surface. The STM technique bypassed the diffraction limit of light and achieved higher sensitivity than the electron microscope while utilizing much lower energy. It was soon realized however that STM was not an ideal method to study biological objects because the surface of the sample should be conductive.

The requirement that the surface must be conductive was overcome in 1986 with the invention of a variation of the STM known as the Atomic Force Microscope (AFM) by Gerd Binnig, Calvin Quate and Christopher Gerber.[4] An AFM images the topography of a sample by scanning the sharp tip across the sample and recording the deflection of the cantilever to which the tip is connected. AFM has the ability to image conductive and non-conductive surfaces beyond the diffraction limit with molecular and atomic resolution both in air and in liquid.

Each of the described imaging methods carries its own advantages and disadvantages, and often a certain method is chosen taking into account the required resolution (both spatial and temporal), sample stability, and chemical specificity. However, as research extends to the smallest length scales where complex systems are studied, individual microscopy techniques do not supply sufficient information to understand the interactions, structure or dynamic mechanisms. Combining different microscopy techniques, i.e. correlative microscopy, has emerged in the past years and

employs the respective advantage of two or more methods that can be directly compared and provide complementary information.

Correlated microscopy is widely employed in biology where the high spatial resolution of AFM or EM is combined with the chemical specificity of fluorescence microscopy. In this thesis we expand the scope of correlative microscopy by integrating fluorescence microscopy, atomic force microscopy, and optical spectroscopy in a single instrument. We apply this approach to nanostructured assemblies on solid-liquid interfaces. In this chapter we firstly discuss the physical principles that dictate the temporal and spatial resolution of commonly used microscopy techniques, i.e. optical microscopy, electron microscopy, and atomic force microscopy. We discuss their advantages and disadvantages, and typical applications. We finish this introductory chapter by highlighting the nanostructures investigated in this thesis, namely self-assembled supramolecular polymers and self-assembled nanoparticles.

1.2 Optical microscopy

Optical microscopy is a powerful tool that started in the 17th century using simple devices that use natural light or candles for illumination through one or two lenses, as pioneered by Antoni van Leeuwenhoek and Robert Hooke. Currently optical microscopy has evolved into a wide range of complementary approaches with advanced illumination and detection approaches.

Far-field optical microscopy is limited by the diffraction of light, meaning it cannot resolve structures smaller than approximately half the wavelength of light. The resolution of an optical microscope is determined to which extent two closely spaced point-like objects that emit incoherently can be separated in the image. Diffraction of the circular aperture of a microscope lens results in an Airy disk in the image plane. As the two objects approach each other their Airy disks start overlapping. The most often used criterion for optical resolution is the one defined by Ernst Abbe, given by

$$r_{\mathrm{Abbe}} = \lambda/2\mathrm{NA}. \tag{1.1}$$

Here, λ is the wavelength of light and $\mathrm{NA} = n \sin\theta$ the numerical aperture, with n the refractive index of the medium and θ the maximum half-angle of the cone of light that can enter the lens (see **Figure 1.1a**). The criterion states that, to resolve two diffraction-limited spots, they need to be spaced by a distance so that their half-maxima overlap in space, see **Figure 1.1b**. Using state-of-the-art objective lenses with a numerical aperture NA~1.5 in combination with green light we find a typical resolution of 180 nm which is routinely achieved using any research-grade microscope.

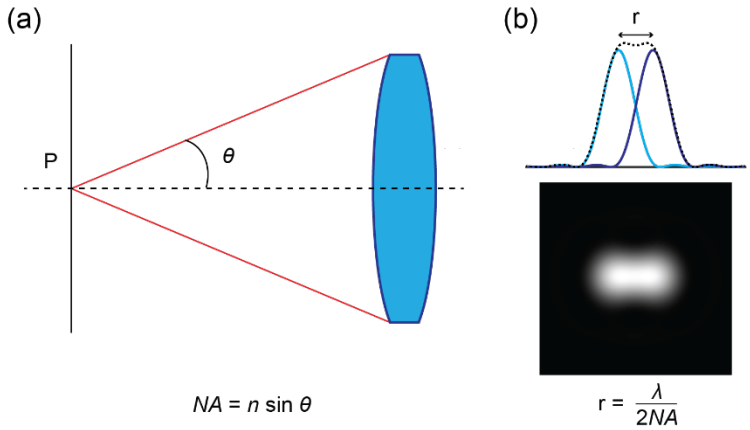

Figure 1.1 (a) Schematic of a lens showing how its numerical aperture NA depends on the refractive index of the medium n and the half-angle θ of the illuminating light-cone. **(b)** Resolution definition based on the Abbe criterion.

The most important component of a setup capable of diffraction-limited imaging is a high-quality objective, provided that it is combined with a stable light source and a sensitive detector. Commonly used diffraction-limited microscopy techniques detect a variety of signals such as absorption, elastic and inelastic (e.g. Raman) scattering, higher harmonics, photoluminescence, or fluorescence.

Fluorescence microscopy is especially used in the domains of biology and physical chemistry due to its chemical specificity. This specificity is typically achieved by labelling chemical groups with a fluorescent dye. Furthermore, the technique is inherently dark-field because a dichroic mirror separates the excitation light from the Stokes-shifted emission. The simplest optical configuration to perform fluorescence microscopy is the epi-fluorescence microscope. Here, the excitation beam is focused at the back aperture of the objective lens resulting in illumination with a nearly collimated excitation beam that propagates into the sample. The Stokes shifted fluorescence is then collected by the objective and passes through the dichroic mirror onto a camera. Though simple in its optical layout, epi-fluorescence microscopy suffers from background signals and limited signal-to-noise ratio since the whole sample is excited by the collimated illumination beam.

This limitation can be largely solved by illumination via total internal reflection. Herein light is directed toward the sample at an angle exceeding the critical angle $\theta_c = \arcsin n_2/n_1$, where n_1 and n_2 are the refractive indices of the two media, usually glass and water. The excitation beam undergoes total internal reflection at the interface resulting in an evanescent field at the opposing side of the interface. The evanescent field only penetrates typically 100 nm into the medium, thus limiting the excitation

volume to a thin sheet near the glass-water interface. This reduces photobleaching and background signals of solution-phase fluorophores and typically results in superior signal-to-noise ratio compared to epi-fluorescence microscopy.

The drawback of TIR microscopy is that the excitation volume does not extend into the sample so the technique is limited to imaging structures at the glass-water interface. Confocal microscopy overcomes this limitation because here the excitation beam is strongly focused into the sample by the objective lens. The collected signal is then wavelength-filtered before passing through a pinhole and falling on a point-detector. The pinhole blocks emission that originated from outside the focal plane (optical sectioning) and results in similar signal-to-noise ratios as TIR microscopy. The largest advantage of confocal microscopy over TIR microscopy is the ability to scan the sample in 3D, whereas in TIR only sections close to the interface can be imaged. However, image generation requires either beam- or sample-scanning, making confocal microscopy the slowest of the three approaches described above.

Commonly used fluorophores (e.g. ATTO or Alexa dyes) result in ~10^3-10^4 detected photons per second. Combined with currently available detector technologies such as electron multiplying charge coupled devices (EMCCD) and complementary metal-oxide-semiconductor (CMOS) cameras this makes fluorescence microscopy the golden standard to study dynamics in biological and soft-matter samples. However, the combination of chemical specificity and temporal resolution comes at the expense of the ability to obtain high resolution images. In the past two decades, different techniques have been developed to obtain optical images with sub-diffraction-limited resolution. Examples of these superresolution microscopy techniques are stochastic optical reconstruction microscopy (STORM),[5] photo-activated localization microscopy (PALM)[6] and stimulated emission-depletion (STED).[7]

STORM and PALM usually use TIR excitation and operate under conditions where only a small number of individual fluorophores is emissive in each frame. These emitting fluorophores can then be localized by fitting the corresponding point spread function with a two-dimensional Gaussian function, see **Figure 1.2a**. This is repeated for many camera frames until nearly all fluorophores have been 'on' at least once and the sample image can be "reconstructed" from all localizations. For reasonably bright fluorophores the localization precision σ is shot-noise limited and only depends on the number of detected photons N and the standard deviation of the point spread function s as $\sigma = s/\sqrt{N}$, where $s = r_{abbe}/(2\sqrt{2}\ln 2)$. This results in a typical lateral localization precision for STORM and PALM of 10-20 nm for a few thousand detected photons (see **Figure 1.2b**), whereas axial precisions of 20-50 nm have been achieved.[8] Although super-resolution reconstruction takes minutes to hours because thousands of frames need to be collected, it is compatible with any wide-field optical microscope.

Stimulated emission depletion (STED) microscopy achieves sub-diffraction-limited resolution by the use of an extra laser beam in a confocal microscope, the so-called depletion beam. The excitation beam with a regular Gaussian beam profile is overlapped with a red-shifted doughnut-shaped STED beam that brings fluorophores back to the ground state using stimulated emission (see **Figure 1.2c**). The STED beam is typically on the red wing of the emission spectrum of the dye, allowing the stimulated photons to be wavelength filtered whereas the fluorescence photons are detected on a point-detector. The effective excitation volume of the beam is then reduced by the presence of the doughnut, resulting in an intensity-dependent lateral resolution that is typically 20-70 nm (see **Figure 1.2d**) and an axial resolution of 40-150 nm.[9]

Compared to STORM and PALM, where images can only be reconstructed after the majority of dyes has entered the "on-state" at least once, STED has a higher temporal resolution on the order of 0.1-1 second. However, STED microscopy does require especially photostable dyes to sustain extended exposure to the high-power STED beam.

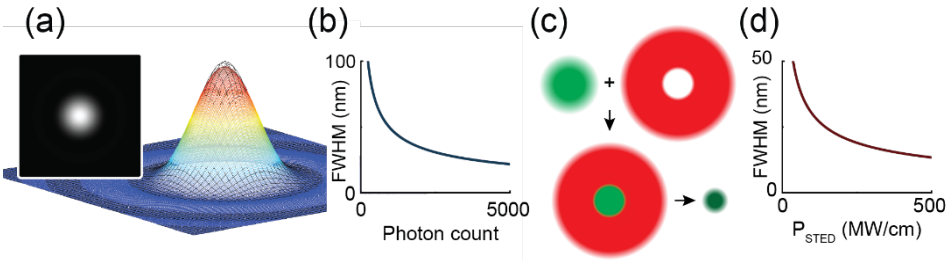

Figure 1.2 Resolution dependence of superresolution techniques. (a) Point spread function in 2D (left inset) and 3D (colored pattern) with a 2D Gaussian fit (mesh). **(b)** Schematic dependence of the FWHM of the 2D Gaussian fit on the photon count. **(c)** Principle of STED. A Gaussian excitation beam (green spot) is overlapped with a doughnut-shaped beam (red). Due to stimulated emission the effective spot size is equal to the size of the hole of the red beam (dark green spot). **(d)** Schematic dependence of the FWHM as a function of STED power.

1.3 Atomic force microscopy

Although optical microscopy gives easy access to dynamics and provides chemical specificity, it requires robust fluorescent labelling protocols and is not yet suitable to resolve length-scales shorter than ~20 nm. Atomic force microscopy (AFM)[4] on the other hand is a scanning probe microscopy technique used to map sample topography with (sub-)nanometer resolution. A sharp tip located at the end of a cantilever is scanned over the sample, where a feedback mechanism is used to map changes in the cantilever deflection. Here, cantilever deflection directly relates to sample height

and/or tip-sample interaction forces. The spatial resolution of AFM then mainly depends on the sharpness of the tip and the mechanical properties of the sample. Sharp tips have even been used to obtain atomic resolution.[10,11] Typical resolutions using standard silicon cantilever tips however are in the range of a few nanometers.

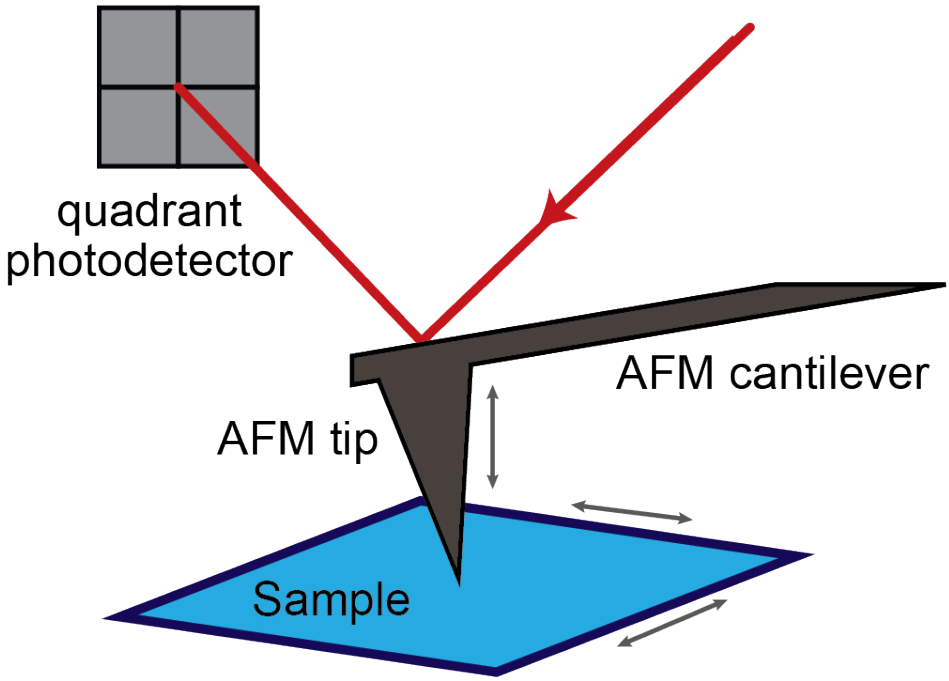

Figure 1.3 Working principle of the AFM. An AFM tip at the end of a cantilever scans over the sample. Changes in sample topography result in deflection of the cantilever. These deflections are measured by a laser beam reflecting off the cantilever onto a quadrant photodetector. To measure sample topography while scanning a feedback system is used.

The working principle of an AFM is shown in **Figure 1.3**. It consists of several essential components, i.e. a soft cantilever spring with a sharp tip, a method to measure cantilever deflection, a feedback system to maintain and monitor a certain deflection, and a scanning stage to construct an image of the sample topography.[12] AFM can be operated in different modes which differ mainly in the feedback system used. In contact mode, the tip remains in close contact with the surface and the tip-sample force is used as a feedback mechanism. Cantilever deflection is directly related to force and is monitored optically using a quadrant photodetector that monitors displacement of a reflected laser beam. By keeping either force or height constant a topographical image is formed by scanning the tip over the surface. Contact mode generates high resolution topography measurements but produces nanonewton lateral forces on the sample. For hard materials the damage is minimal, but for soft materials, e.g. biological samples,

contact mode causes irreversible damage. In non-contact[13] and tapping mode[14] the lateral forces are virtually eliminated and indentation forces significantly reduced because the tip is only transiently in contact with the substrate.[14]

AFM also allows for measurement in liquid,[15] which eliminates capillary forces of absorbed water layers on the sample. The thin water layer causes adhesion of the tip resulting in a large force when the tip 'snaps into' the surface. Eliminating these forces in liquid reduces damage to the sample further, making imaging of soft biological samples now routinely possible.[16] Furthermore, AFM in fluids allows the study of biological molecules in a buffer solution that mimics their native environment. This makes non-contact and tapping modes in fluid suitable for soft and biological samples, and they have been used to image actin[17], microtubules[17], DNA[16,18,19], and live cells.[20]

Conventional AFM is slower than most optical methods because it requires tip-scanning. Although the scanning of the tip itself can be rapid, the imaging rate is limited by the feedback mechanisms that makes the tip carefully follow the sample topography. Optimization of the cantilever length and stiffness, and electronics for high-speed feedback has enabled AFM with a temporal resolution of 10 frames per second allowing for single-protein dynamics to be studied.[21]

1.4 Electron microscopy

Electron microscopy also allows for imaging on picometer length scales as it uses electrons rather than photons for imaging. In an electron microscope, first developed by Knoll *et al.*,[2] electrons are accelerated by an electron gun and focused by electromagnetic coils onto the sample. The electrons are characterized by their De Broglie wavelength $\lambda = h/p = h/\sqrt{2meV}$, with h Planck's constant and p, m and e are the electrons momentum, mass, and charge respectively. The velocity of the incident electrons is determined by the potential difference V across which they are accelerated in the microscope (typically 100-300 keV). Under typical conditions this results in a De Broglie wavelength in the range of 1-5 picometer. In combination with advanced aberration correction techniques this enables imaging at atomic resolution.[24]

Though high resolution is reached in electron microscopy, it is operated in vacuum and the damage caused by the high energy electrons makes it ill-suited to image soft samples. In cryo-electron microscopy (cryo-EM) the sample is frozen, preserving biomolecules closer to their native state,[25] which has allowed for the analysis of the structure of small proteins down to 3 Å in resolution.[26,27] The main challenge in EM studies of soft matter samples is the low signal-to-noise ratio due to the low electron

density of the material, necessitating the averaging of many images to resolve a single protein with sufficient signal-to-noise ratio.[28]

Whereas the spatial resolution of electron microscopy is superior to diffraction-limited optical microscopy methods, it lacks chemical specificity, often operates under vacuum conditions, and is not easily operated at ambient conditions in fluid. Nevertheless EM is often employed to study the topography and crystallinity of nanostructures. In this thesis we focus instead on the correlation of optical microscopy methods with AFM due to its easier method of operation, direct integration with the optical setup and its suitability for measurements on soft samples in aqueous buffers.

1.5 Correlative microscopy

Figure 1.4 summarizes the temporal and spatial resolutions of the above described microscopy techniques, whereas **Table 1.1** lists the main advantages and disadvantages of each method. Both AFM and electron microscopy (EM) have atomic resolution, making them ideal to resolve sample topography with superior spatial resolution. However, they exhibit a limited temporal resolution of seconds to minutes and provide little chemically specific information particularly for organic samples. Optical microscopy on the other hand exhibits a limited spatial resolution due to the diffraction limit of light but gives access to millisecond temporal resolution. In addition, it provides chemically specific information due to the fluorophore labels that can be conjugated via specific chemical reactions.

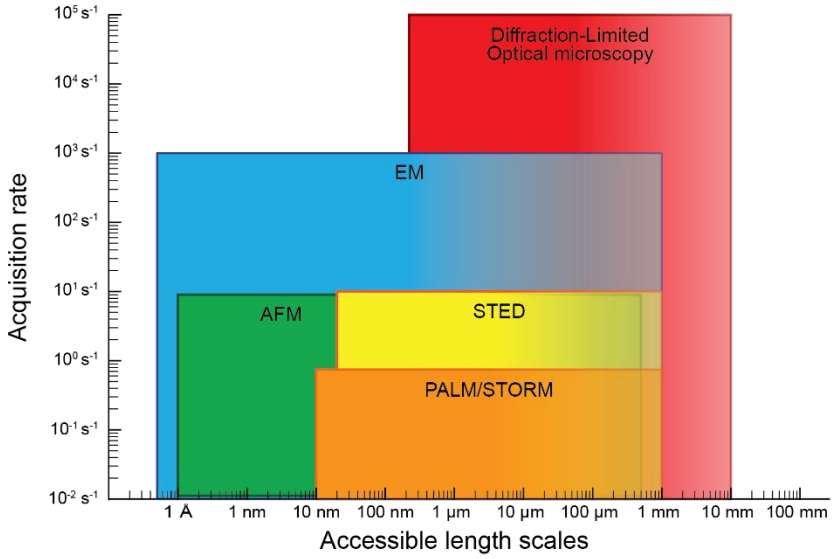

Figure 1.4 Acquisition rate and accessible length scales for atomic force microscopy, electron microscopy, superresolution techniques PALM, STORM and STED, and diffraction-limited optical microscopy.

Combining different microscopies to take advantage of their strong points has led to the development of a wide range of correlative techniques. For example, combining the chemical specificity and time resolution of optical microscopy with the high spatial resolution provided by AFM results in a wealth of new information. Typical workflows for correlative microscopy can be separated in two classes:

(1) sequential imaging in separate devices, or

(2) an integrated approach where both imaging modalities are combined on the same setup.

In the first approach, Maubach *et al.* aligned DNA molecules using electrodes, visible both optically and in AFM. By sequential imaging they developed a new method for the self-assembled positioning of molecular structures on chip surfaces.[33] Also in early fibronectin fibrillogenesis the conformation of single polymers could not be observed because they were smaller than the diffraction-limited optical resolution, but visual overlay with separately obtained AFM images enabled the correlation of chemically specific information with nanoscale topography.[34]

Table 1.1 Spatial and temporal resolution of different microscopy methods and their main advantages and disadvantages

	OM	STORM/PALM	STED	AFM	EM
Temporal resolution	µs [22,23]	minutes [29]	seconds [6]	seconds [8]	seconds [31]
Spatial resolution	200 nm	10 nm [5]	20 nm [7]	atomic [30]	atomic [32]
Advantages	chemical specificity; high temporal resolution	Chemical specificity; Nanometer spatial resolution		High spatial resolution; No labelling required	
Drawbacks	Low spatial resolution	Low temporal resolution		Slow acquisition; Low chemical specificity	Low contrast on biological samples; Low chemical specificity

An integrated approach enables the simultaneous or consecutive imaging of a nanostructure by optical and atomic-force microscopy. Correlative measurements in the same sample area require the proper positioning of the AFM's tip with respect to the optical axis of the microscope. For large structures the optical image of the cantilever as a whole can be used for alignment,[37] resulting in a co-localization of the optical and AFM images with micrometer accuracy. Nanoscale structures however require a more accurate overlap, Kolodny *et al.* spatially correlated the AFM tip to their fluorescence excitation spot by scanning the sample while simultaneously recording the scattering from the AFM tip.[38] Alignment in post-processing can also be employed, where cross-correlation between the fluorescence and AFM image enables accurate alignment of the excitation laser with the AFM probe.[39]

Two typical examples showing the power of correlative microscopy are shown in **Figure 1.5**. AFM correlated with STED microscopy enabled Cosentino and colleagues to investigate the formation of amyloid aggregates with high spatial resolution and chemical specificity (**Figure 1.4a-b**). Only a fraction of the aggregates was visible in STED images, indicating that the fluorescently labeled molecules did not participate in the aggregation process via the same pathway as the unlabeled molecules.[35] **Figure 1.5c-f** on the other hand depicts correlated electron microscopy and super-resolution fluorescence microscopy of histone proteins.[36] By correlating both techniques the authors demonstrated the possibility to identify histone proteins in electron micrographs using the chemical specificity supplied by the fluorescence images.

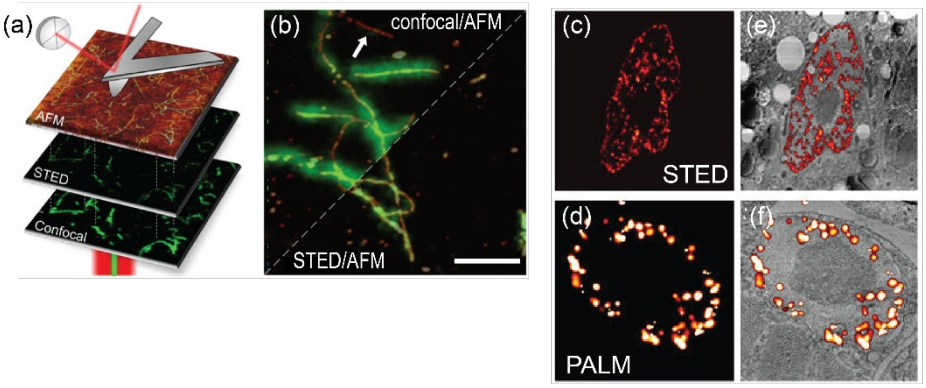

Figure 1.5 Examples of correlated microscopy. (a) AFM correlated with both STED and confocal microscopy showing **(b)** amyloid fibrils in diffraction-limited and superresolution with their height profile. The arrow points to a fibril not visible in fluorescence microscopy.[35] **(c)** STED and **(d)** PALM images of histone proteins overlayed on (e-f) electron microscopy images of the cell nucleus.[36]

1.6 Model systems: nanoscale assemblies

Correlative microscopy has largely been applied to biological samples.[28,33,34,40,41] In this thesis we demonstrate its applicability to obtain detailed information on synthetic nanomaterials as well. We particularly focus on self-assembled synthetic nanomaterials because tight control over the assembly process and pathways provides emerging functionalities that are often not accessible using only the individual building blocks. To investigate synthetic self-assembled materials we integrated three modalities on a single device:

(1) optical microscopy,

(2) optical spectroscopy, and

(3) atomic force microscopy.

Integration on a single device removes sample transport and alignment procedures to enable the study of the same assembled structures using the different techniques. We apply this integrated approach to study self-assembled nanomaterials at solid-liquid interfaces. Below we shortly highlight the two nanomaterials that were employed in this thesis, namely nanoscale polymeric assemblies and nanoparticle assemblies.

1.6.1 Model system I: polymeric assemblies

Unlike conventional bonded polymers, supramolecular polymers engage in a variety of non-covalent interactions that define their properties. Supramolecular polymers consist of monomers that self-assemble through non-covalent interactions such as hydrogen bonding, hydrophobic interactions, van der Waals forces, electrostatic interactions and pi-pi interactions. Biological supramolecular structures are well-known, e.g. actin and microtubules. Synthetic variants of these biological counterparts are interesting from both a fundamental perspective, where full control over their chemistry allows to introduce a large variety of properties and function, whereas from an application perspective these assemblies result in emerging functionalities now used in e.g. cosmetics and ink-jet printing.[42] In biological supramolecular polymers dynamics are also important, such as the polymerization and depolymerization of actin as a driving factor in cytokinesis[43] and cell motility.[44]

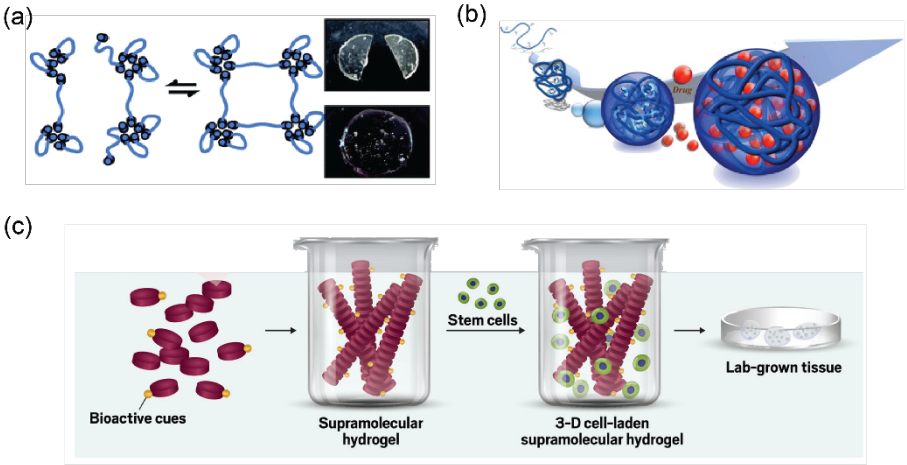

Figure 1.6 Examples of applications of supramolecular polymers for **(a)** self-healing materials,[45] **(b)** drug delivery,[46] and **(c)** tissue engineering.[47]

A supramolecular assembly typically results in non-covalent and dynamic interactions between chemical moieties that make up the core of the polymer (in dark grey in **Figure 1.6a**), surrounded by side-groups that provide solubility. Their dynamic behavior, caused by the non-covalent bonds between monomers, plays a principal role in these applications. An example is shown in **Figure 1.6a**, where the dynamic nature of the material provides self-healing properties. First reported by Cordier *et al.*,[48] when fractured surfaces were brought into contact, reformation of hydrogen bonds resulted in recovery of elasticity. Tee *et al.*[49] showed applications in biomimetics and soft

robotics for hydrogels composed of supramolecular polymers that showed both mechanical and electrical self-healing.

Importantly, a large range of approaches is available to conjugate biocompatible and bioactive side-groups making them ideal candidates for applications in biological environments. For example, therapeutics can be incorporated in supramolecular assemblies to provide drug-delivery vehicles that are disassembled in a certain biological environment resulting in drug release (**Figure 1.6b**). Examples are the delivery of growth factor for cartilage regeneration by peptide amphiphiles[42] and the ability of 1,3,5-benzenetricarboxamide (BTA) polymers to simultaneously transport siRNA and hydrophobic particles into cells.[50] For the latter application the positively charged hydrophilic interfacial groups electrostatically bind RNA, whereas the hydrophobic interior encapsulates the hydrophobic particles.

Biocompatibility and tunability make supramolecular polymers also ideal for tissue engineering applications (**Figure 1.6c**). Cells are grown on biologically active supramolecular assemblies resulting eventually in the growth of bioartificial tissues and even organs. Dankers *et al.*[51] use fibrous supramolecular membranes to create a bioartificial kidney. They show that renal tubular cells grow on these structures as opposed to the lack of cell growth on microporous polycarbonate membranes

Supramolecular polymers have largely been studied at the ensemble level. Single-molecule studies have so far focused on electron microscopy,[52] where samples need freezing and high vacuum to provide enough contrast. Recently, super-resolution microscopy was applied to study the dynamic behavior of individual polymers at a spatial resolution of several tens of nanometers. However, the polymers are typically only a few nanometers in diameter that is not resolved using super-resolution imaging. In **Chapter 3** we show how correlative microscopy (AFM + fluorescence) can be employed to study the structure and mechanical properties of supramolecular polymers at the single-molecule level.

1.6.2 Model system II: particle assemblies

Nanometer sized metal particles possess unique optical properties arising from the resonant coupling of incident light to the conduction electrons in the particle (**Figure 1.7a**). The collective motion of the conduction electrons is called a surface plasmon resonance and results in locally enhanced optical fields and strong scattering and absorption (**Figure 1.7b,d**). The wavelength of the plasmon resonance depends on the shape, size, material and local environment of the particle.[53] This tunability combined with advances in bottom-up and top-down synthesis methods[54] have sparked research

into applications ranging from sensing[53] and cancer treatment[55] to nanoantennas[56] and labels for tracking.[57]

Their photostability, chemical inertness, and versatile functionalization chemistry using gold-thiol bonds[58] makes plasmonic particles ideally suited for sensing applications. Biosensing can be achieved by e.g. employing the large local intensity enhancements for plasmon-enhanced fluorescence sensing[59] or sensing by surface-enhanced Raman scattering.[60] A particularly attractive sensing modality employs the sensitivity of the plasmon resonance for the dielectric function of the local environment, resulting in a red-shift of the plasmon resonance when a biomolecule is nearby (**Figure 1.7c-d**). This sensing modality is "label-free" because it does not rely on fluorescently labelled analyte. Recent advances in optical detection and spectroscopy of metallic particles, and their robust functionalization with biologically active receptors has even allowed for the detection of single proteins by sensitively detecting plasmon shifts in an optical microscope.[61,62,63,64]

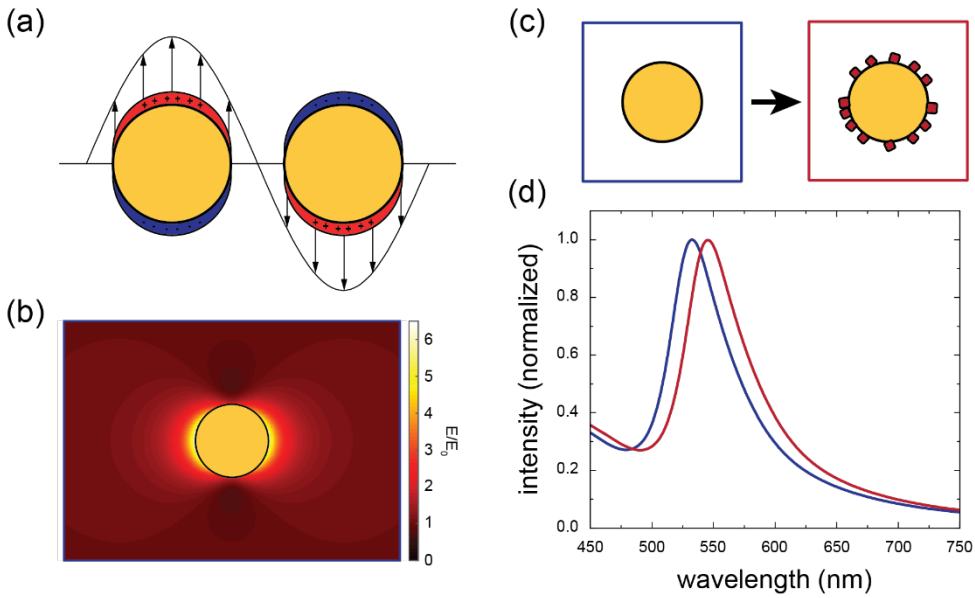

Figure 1.7 Plasmonic sensing (a) Schematic of the localized surface plasmon resonance excitation for gold nanospheres. **(b)** Near-field of an excited gold nanosphere at its plasmon resonance wavelength. **(c)** Binding of single molecules to gold nanosphere. **(d)** Scattering spectra of the gold nanosphere **(b**, blue curve) and upon binding of single molecules (red curve).

The sensitivity of plasmon sensors largely depends on the overlap between the locally enhanced electric field and the biomolecular analyte. Higher and more confined local fields typically result in improved sensitivity owing to the stronger interaction between the plasmon resonance and the molecule. The material and shape of the

metallic particle give some control over the locally enhanced electric fields and scattering spectra, but a substantially larger effect has been observed when two particles are coupled by placing them in close proximity (**Figure 1.8a**). The degree of coupling and resulting optical response strongly depends on the assembly's geometry, and in some cases results in the appearance of new resonances associated with coupled plasmons (see **Figure 1.8b**).

The appearance of new resonances can be understood by considering the two plasmon resonances in the individual particles to hybridize, much like atomic orbitals do. This plasmon hybridization results in bonding and anti-bonding modes whose energy depends on the type of mode and the proximity between the particles (i.e. their coupling strength). In **Figure 1.8c** the symmetric and asymmetric bonding and antibonding modes are shown for nanosphere dimers. The symmetric bonding mode and the asymmetric antibonding mode have a dipole moment parallel to the dimer longitudinal axis, where the bonding mode has the lowest energy and a net dipole moment. In contrast, for the asymmetrical antibonding mode the dipoles cancel each other out. For the symmetric antibonding mode and asymmetric bonding mode, the dipole moment is oriented perpendicular to the dipole longitudinal axis. Here, the symmetric antibonding dipole moment is higher in energy with a net dipole moment, whereas in asymmetric bonding mode the dipole moments cancel each other out.[65]

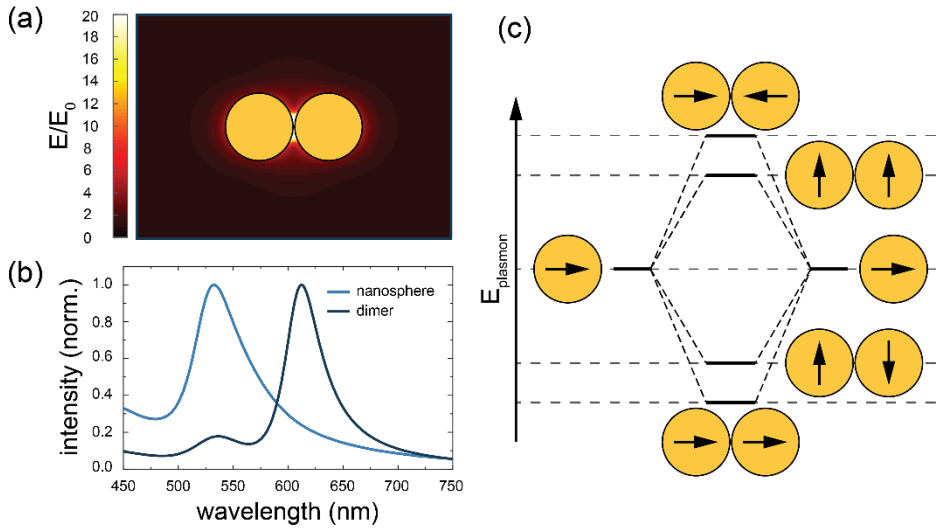

Figure 1.8 Far-field and near-field response of a gold nanosphere dimer. (a) Near-field upon longitudinally polarized excitation of a gold nanosphere dimer. **(b)** Scattering spectra of a single gold nanosphere (light blue line) and a gold nanosphere dimer (dark blue line). **(c)** Plasmon hybridization schematic of gold nanosphere dimers showing the corresponding energy levels of the bonding and antibonding modes under transverse and longitudinal excitation.

Such hybridized plasmon modes show great promise for sensing as they provide control over the wavelength at which the resonance occurs (allowing one to tune the resonance to e.g. a biologically transparent window) and they provide unsurpassed enhancements of the near-field intensity. This has been used to improve both plasmon-enhanced fluorescence sensors[66] and label-free sensing.[67]

The rational design of plasmon-based sensors however requires structure-function relationships that correlate the optical properties and spectra of particle assemblies to their precise topography. Typical particle-sizes employed are 10-100 nm in diameter, which are not resolved using optical microscopy. A correlative approach is therefore highly appropriate to investigate the correlation between the geometry of individual assemblies and their optical response. In **Chapter 4** and **Chapter 5** of this thesis we investigate the optical response of different configurations of self-assembled nanoparticle heterodimers and investigate the correlation between geometry and sensing performance.

1.7 Research goal and outline of the thesis

The aim of this research is to study different systems and their relation between structure and function using correlative microscopy techniques. We aim to quantify the structure of nanoscale assemblies at the glass-fluid interface and their optical properties through wide-field and spectroscopic measurements. At the glass-liquid interface we can simultaneously image the structure of the sample from the tip and its optical properties through the transparent glass coverslip. The combination of orthogonal techniques allows us to combine their advantages opening up more applications and further our understanding of the samples. The long term aim is to optimize and expand our correlated setup as a tool for a broad variety of structure-function relationships.

In **chapter 2** the experimental setup is described, where we discuss atomic force microscopy and spectroscopy in detail. The different AFM modes and their working principle is discussed as well as the optimal mode for soft samples. We compare spectroscopy techniques and discuss their respective (dis)advantages. Finally, we describe how we correlate AFM to optical and spectroscopic imaging.

In **Chapter 3** we study dye-labeled supramolecular polymers absorbed to a glass surface and quantify their persistence length. Using correlated AFM and wide-field total internal reflection fluorescence microscopy we identify single unentangled polymers and perform persistence length analysis to quantify their stiffness.

In **Chapter 4** we discuss gold nanorods and their application in sensing. Sensitivity depends on nanoparticle shape, size and the refractive index of local environment. We show the location-dependent sensitivity of nanorods by binding gold nanospheres. The binding location is determined by atomic force microscopy and correlated to plasmon shift, to find the dependence of the plasmon shift on binding location. We compare measurements to calculations to find the influence of size dispersion of both the nanorod and nanosphere on the experimental results.

In **chapter 5** the sensitivity of gold nanorod dimers is investigated. Self-assembly of dimers results in a variety of angles in between the dimer. Dimer dimensions and angles are measured by atomic force microscopy and correlated to plasmon shift as well as compared with calculations. We calculate and measure sensitivity for bonding and antibonding modes and asses the effect of the linker molecules on their sensing capabilities.

Finally, **chapter 6** summarizes the conclusions and presents an outlook.

References

1. Gest, H. The discovery of microorganisms by Robert Hooke and Antoni van Leeuwenhoek, Fellows of the Royal Society. *Notes Rec. Soc. Lond.*, **2004**, *58(2)*, 187-201.
2. Ruska, E.; Knoll, M. Die magnetische Sammelspule für schnelle Elektronenstrahlen. Z. Techn. Physik, **1931**, *12*, 380-400.
3. Parot, P.; Dufrêne, Y. F.; Hinterdorfer, P.; Le Grimellec, C.; Navajas, D.; Pellequer, J-L.; Scheuring, S. Past, present and future of atomic force microscopy in life sciences and medicine. *J. Mol. Recognit.*, **2007**, *20*, 418-431.
4. Binnig, G.; Quate, C. F.; Gerber, C. Atomic Force Microscope. *Phys. Rev. Lett.* **1986**, *56,* 930-934.
5. Olivier, N.; Keller, D.; Gönczy, P.; Manley, S. Resolution doubling in 3D-STORM imaging through improved buffers. *PLoS ONE*, **2013**, *8(7),* e69004.
6. Schneider, J.; Zahn, J.; Maglione, M.; Sigrist, S. J.; Marquard, J.; Chojnacki, J.; Kräussluch, H-G.; Sahl, S. J.; Engelhardt, J.; Hell, S. W. Ultrafast, temporally stochastic STED nanoscopy of millisecond dynamics. *Nat. Methods*, **2015**, *12*, 827-832.
7. Göttfert, F.; Wurm, C.A.; Mueller, V.; Berning, S.; Cordes, V. C.; Honigmann, A.; Hell, S. W. Coaligned dual-channel STED nanoscopy and molecular diffusion analysis at 20 nm resolution. *Biophys. J.*, **2013**, *105*, L01-L03.
8. Miyagi, A.; Tsunaka, Y.; Uchihashi, T.; Mayanagi, K.; Hirose, S.; Morikawa, K.; Ando, T. Visualization of intrinsically disordered regions of proteins by high-speed atomic force microscopy. *Chem. Phys. Chem.*, **2008**, *9*, 1859-1866.
9. Maglione, M.; Sigrist, S. J. Seeing the forest tree by tree: super-resolution light microscopy meets the neurosciences. *Nat. Neurosci.*, **2013**, *16*, 790-797.
10. Binnig, G; Gerber, C.; Stoll, E.; Albrecht, T. R.; Quate, C. F. Atomic resolution with atomic force microscope. *Europhys. Lett.*, **1987**, *3*, 1281-1286.
11. Alexander, S.; Hellemans, L.; Marti, O.; Schneir, J.; Elings, V.; Hansma, P. K.; Longmire, M.; Gurley, J. An atomic-resolution atomic-force microscope implemented using an optical lever. *J. Appl. Phys.*, **1989**, *65*, 164-167
12. Rugar, D.; Hansma, P. Atomic force microscopy. *Phys. Today* **1990**, *43(10)*, 23-30.
13. Martin, Y.; Williams, C. C.; Wickramasinghe, H. K. Atomic force microscope-force mapping and profiling on a sub 100-Å scale. *J. Appl. Phys.* **1987**, *61,* 4723-4729.
14. Zhong, Q.; Innis, D.; Kjoller, K.; Elings, V. B. *Surf. Sci. Lett.* **1993**, *290*, L688-L692.
15. Marti, O.; Drake, B.; Hansma, P. K. Atomic force microscopy of liquid-covered surface: atomic resolution images. *Appl. Phys. Lett.* **1987**, *51*, 484-486.
16. Hansma, P. K.; Cleveland, J. P.; Radmacher, M.; Walters, D. A.; Hillner, P. E.; Bezanilla, M. Fritz, M.; Vie, D.; Hansma, H. G.; Prater, C. B.; Massie, J.; Fukunaga, L.; Gurley, J.; Elings, V. Tapping mode atomic force microscopy in liquids. *Appl. Phys. Lett.* **1994**, *64*, 1738-1740.
17. Fritz, M.; Radmacher, M.; Cleveland, J. P.; Allersma, M. W.; Stewart, R. J.; Gieselmann, R.; Janmey, P.; Schmidt, C. F.; Hansma, P. K. Imaging globular and filamentous proteins in physiological buffer solutions with tapping mode atomic force microscopy. *Langmuir*, **1995**, *11*, 3529-3535.
18. Hansma, H. G.; Laney, D. E.; Bezanilla, M.; Sinsheimer, R. L.; Hansma, P. K. Applications for atomic force microscopy of DNA. *Biophys. J.*, **1995**, *68*, 1672-1677.
19. Yang, C-W.; Hwang, I-S.; Chen, Y. F.; Chang, C. S.; Tsai, D. P. Imaging of soft matter with tapping-mode atomic force microscopy and non-contact-mode atomic force microscopy. *Nanotechnology*, **2007**, *18*, 084009.
20. Plomp, M.; Leighton, T. J.; Wheeler, K. E.; Hill, H. D.; Malkin, A. J. *In Vitro* high-resolution structural dynamics of single germinating bacterial spores. *Proc. Natl. Acad. Sci. U.S.A.*, **2007**, *104*, 9644-9649.
21. Ando, T. High speed AFM imaging. *Curr. Opin. Struct. Biol.* **2014**, *28*, 63-68. Ruska, E.; Knoll, M. Die magnetische Sammelspule für schnelle Elektronenstrahlen. Z. Techn. Physik, **1931**, *12*, 380-400.
22. Nan, X.; Sims, P. A.; Xie, X. S. Organelle tracking in a living cell with microsecond time resolution and nanometer spatial resolution. *ChemPhysChem*, **2008**, *9*, 707-712.
23. Ueno, H.; Nishikawa, S.; Lino, R.; Tabata, K. V.; Sakakihara, S.; Yanagida, T.; Noji, H. Simple dark-field microscopy with nanometer spatial precision and microsecond temporal resolution. *Biophys. J.*, **2010**, *89*, 2014-2023.

24. Erni, R.; Rossell, M. D.; Kisielowski, C.; Dahmen, U. Atomic-resolution imaging with a sub-50-pm electron probe. *Phys. Rev. Lett.,* **2009**, *102*, 096101.
25. Adrian, M.; Dubochet, J.; Lepault, J.; McDowall, A.W. Cryo-electron microscopy of viruses. *Nature*, **1984**, *308*, 32-36.
26. Lu, P.; Bai, X.; Ma, D.; Xie, T.; Yan, C.; Sun, L.; Yang, G.; Zhao, Y.; Zhou, R.; Schers, S.H.W.; Shi, Y. Three-dimensional structure of human γ-secretase. *Nature,* **2014**, *512*, 166-170.
27. Khoshouei, M.; Radjainia, M.; Baumeister, W.; Danev, R. Cryo-EM structure of haemoglobin at 3.2 Å determined with the Volta phase plate. *Nat. Comm.*, **2017**, *8*, 16099.
28. Sigworth, F. J.; Principles of cryo-EM single-particle image processing. *Microscopy*, **2016**, *65*, 57-67.
29. Zhu, L.; Zhang, W.; Elnatan, D.; Huang, B. Faster STORM using compressed sensing. *Nat. methods*, **2012**, *9*, 721-723.
30. Giessibl, F. J. Atomic resolution of the silicon (111)-(7x7) surface by atomic force microscopy. *Science,* **1995**, *267*, 68-71.
31. Zewail, A. H. Four-dimensional electron microscopy. *Science*, **2010**, *328*, 187-193.
32. Takayanagi, K.; Kim, S.; Lee, S.; Oshima, Y.; Tanaka, T.; Tanishiro, Y.; Sawada, H.; Hosokawa, F.; Tomita, T.; Kaneyama, T.; Kondo, Y. Electron microscopy at a sub-50 pm resolution. *J. Electron Microsc.*, **2011**, *60*, S239-S244.
33. Maubach, G.; Fritzsche, W.; Precise positioning of individual DNA structures in electrode gaps by self-organization onto guiding microstructures. *Nano Lett.*, **2004**, *4*, 607-611.
34. Gudzenko, T.; Franz, C. M. Studying early stages of fibronectin fibrillogenesis in living cells by atomic force microscopy. *Mol. Biol. Cell*, **2015**, *26*, 3190-2104.
35. Cosentino, M.; Canale, C.; Bianchini, P.; Diaspro, A. AFM-STED correlative nanoscopy reveals a dark side in fluorescence microscopy imaging. *Sci. Adv.*, **2019**, *5*, eaav8062.
36. Watanabe, S.; Punge, A.; Hollopeter, G.; Willig, K. I.; Hobson, R. J.; Davis, M. W.; Hell, S. W.; Jorgensen, E. M. Protein localization in electron micrographs using fluorescence microscopy. *Nat. Methods*, **2011**, *8*, 80-84.
37. Brown, A. E. X.; Hategan, A.; Safer, D.; Goldman, Y. E.; Discher, D. E. Cross-correlated TIRF/AFM reveals asymmetric distribution of force-generating heads along self-assembled, "synthetic" myosin filaments. *Biophys. J.*, **2009**, 1952-1960.
38. Kolodny, L. A.; Willard, D. M.; Carillo, L. L.; Nelson, M. W.; Van Orden, A. Spatially correlated fluorescence/AFM of individual nanosized particles and biomolecules. *Anal. Chem.*, **2001**, *73*, 1959-1966.
39. Moores, A. N.; Cadby, A. J.; Simultaneous AFM and fluorescence imaging: a method for aligning an AFM-tip with an excitation beam using a 2D galvanometer. *Rev. Sci. Instrum.*, **2018**, *89*, 023708.
40. Thiberge, S.; Nechushtan, A.; Sprinzak, D.; Gileadi, O; Behar, V.; Zik, O.; Chowers, Y.; Michaeli, S.; Schlessinger, J.; Moses, E. Scanning electron microscopy of cells and tissues under fully hydrated conditions. *Proc. Natl. Acad. Sci. USA*, **2004**, *101*, 3346-3351.
41. Ebenstein, Y.; Mokari, T.; Banin, U. Fluorescence quantum yield of CdSe/ZnS nanocrystals investigated by correlated atomic force and single-particle fluorescence microscopy. *Appl. Phys. Lett.*, **2002**, *80*, 4033-4035.
42. Bosman, A. W.; Sijbesma, R. P.; Meijer, E. W. Supramolecular polymers at work. *Mater. Today*, **2004**, *7*, 34-39.
43. Pollard, T. D. Mechanics of cytokinesis in eukaryotes. *Curr. Opin. Cell Biol.*, **2010**, *22*, 50-56.
44. Pollard, T. D.; Borisy, G. G. Cellular motility driven by assembly and disassembly of actin filaments. *Cell*, **2003**, *112*, 453-465.
45. Herbst, F.; Seiffert, S.; Binder, W. H. Dynamic supramolecular poly(isobutylene)s for self-healing materials. *Polym. Chem.*, **2012**, *3*, 3084.
46. Cheng, C-C.; Chang, F-C.; Kao, W-Y.; Hwang, S-M.; Liao, L-C.; Chang, Y-J.; Liang, M-C.; Chen, J-K.; Lee, D-J. Highly efficient drug delivery systems based on functional supramolecular polymers: *in vitro* evaluation. *Acta Biomater.*, **2016**, *33*, 194-202.
47. Arnaud, C. Roxanna Kieltyka. Supramolecular sage is developing polymeric scaffold material for growing tissue in the lab. *C&EN*, **2018**, *96*.
48. Cordier, P.; Tournilhac, F.; Soulié-Ziakovic, C.; Leibler, L. Self-healing and thermoreversible rubber from supramolecular assembly. *Nature*, **2008**, *451*, 977-980.

49. Tee, B. C.-K.; Wang, C.; Allen, R.; Bao, Z. An electrically and mechanically self-healing composite with pressure- and flexion-sensitive properties for electronic skin applications. *Nat. Nanotechnol.*, **2012**, *7*, 825– 32.
50. Bakker, M. H.; Lee, C. C.; Meijer, E. W.; Danker, P. Y. W.; Albertazzi, L. Multicomponent supramolecular polymers as a modular platform for intracellular delivery. *ACS Nano*, **2016**, *10*, 1845-1852.
51. Dankers, P. Y. W.; Boomker, J. M.; Huizing-van der Vlag, A.; Smedts, F. M. M.; Harmsen, M. C.; Van Luyn, M. J. A. The use of fibrous, supramolecular membranes and human tubular cells for renal epithelial tissue engineering: towards a suitable membrane for a bioartificial kidney. *Macromol. Biosci.*, **2010**, *10*, 1345-1354.
52. Lehn, J-M. Supramolecular polymer chemistry – scope and perspectives. *Polym. Int.*, **2002**, *51*, 825-839.
53. Nusz, G. J.; Marinakos, S. M.; Curry, A. C.; Dahlin, A.; Höök, F.; Wax, A.; Chilkoti, A. Label-free plasmonic detection of biomolecular binding by a single gold nanorod. *Anal. Chem.*, **2008**, *80*, 984–989.
54. Pareek, V.; Bhargava, A.; Gupta, R.; Jain, N.; Panwar, J. Synthesis and applications of noble metal nanoparticles: a review. *Adv. Sci. Eng. Med.*, **2017**, *9*, 527-544.
55. Li, J.; Day, D.; Gu, M. Ultra-low energy threshold for cancer photothermal therapy using transferrin-conjugated gold nanorods *Adv. Mater.*, **2008**, *20*, 3866–3871.
56. Kinkhabwala, A.; Yu, Z. F.; Fan, S. H.; Avlasevich, Y.; Mullen, K.; Moerner, W. E. Large single-molecule fluorescence enhancements produced by a bowtie nanoantenna. *Nature Photon.*, **2009**, *3*, 654–7.
57. Nan, X. L.; Sims, P. A.; Xie, X. S. Organelle tracking in a living cell with microsecond time resolution and nanometer spatial precision. Chem. Phys. Chem., **2008**, *9*, 707-712.
58. Zijlstra, P.; Orrit, M. Single metal nanoparticles: optical detection, spectroscopy and applications. *Rep. Prog. Phys.*, **2011**, *74*, 106401.
59. Bauch, M.; Toma, K.; Toma, M.; Zhang, Q.; Dostalek, J. Plasmon-enhanced fluorescence biosensors: a review. *Plasmonics*, **2014**, *9*, 781-799.
60. Yang, X.; Yang, M.; Pang, B.; Vara, M.; Xia, Y. Gold nanomaterials at work in biomedicine. *Chem. Rev.*, **2015**, *115*, 10410-10488.
61. Ament, I.; Prasad, J.; Henkel, A.; Schmachtel, S.; Sönnichsen, C.; Single unlabeled protein detection on inidvidual plasmonic nanoparticles. *Nano Lett.*, **2012**, *12*, 1092-1095.
62. Zijlstra, P., Paulo, P. M. P.; Orrit, M. Optical detection of single non-absorbing molecules using the surface plasmon resonance of a gold nanorod. *Nat. Nanotechnol.*, **2012**, *7*, 379-382.
63. Beuwer, M. A.; Prins, M. W. J.; Zijlstra, P.; Stochastic protein interactions monitored by hundreds of single-molecule plasmonic biosensors. *Nano Lett.*, **2015**, *15*, 3507-3511.
64. Jain, P. K.; El-Sayed, M. A. Plasmonic coupling in noble metal nanostructures. *Chem. Phys. Lett.*, **2010**, *487*, 153-164.
65. Fong, K. E.; Yung, L-Y. L. Localized surface plasmon resonance: a unique property of plasmonic nanoparticles for nucleic acid detection. *Nanoscale*, **2013**, *5*, 12043-12071.
66. Puchkova, A.; Vietz, C.; Pibiri, E.; Wünch, B.; Sanz Paz, M.; Acuna, G. P.; Tinnefeld, P. DNA origami nanoantennas with over 5000-fold fluorescence enhancement and single-molecule detection at 25 μm. *Nano Lett.*, **2015**, *15*, 8354-8359.
67. Aćimović, S. S.; Kreuzer, M. P.; González, M. U.; Quidant, R. Plasmon near-field coupling in metal dimers as a step toward single-molecule sensing. *ACS Nano*, **2009**, *3*, 1231-1237.

Chapter 2

Multimodal correlative microscopy

2.1 Introduction

In our correlative microscopy experiments we combine atomic force microscopy with different optical techniques. In this chapter we discuss the experimental setup, the methods used for optical imaging and spectroscopy, and the working principle and operating modes of AFM. We discuss the challenges of AFM on soft biological samples and how AFM and optical imaging techniques are correlated. With this correlated setup we are able to optically localize molecules and particles based on fluorescence or scattering signals. Alignment of the optical signal with the AFM cantilever allows us to acquire correlated images providing optical and topographical information. In the following chapters we will use such multimodal correlative microscopy to study supramolecular polymers (**Chapter 3**), and self-assemblies of nanoparticles (**Chapter 4** and **Chapter 5**).

2.2 Experimental setup

All experiments in this thesis are performed on an inverted microscope (Nikon Eclipse Ti) with an AFM stage (Bruker Bioscope Catalyst). All optical experiments are performed with a total internal reflection (TIR) setup, where the light source is focused in the back-focal plane of the objective lens by a lens with its center offset from the optical axis. This results in total internal reflection at the glass-water interface of the sample, thus exciting the sample with an evanescent field.

The setup can be configured to detect either fluorescence or (elastic) scattering signals. In **Figure 2.1a** and **b** a total internal reflection fluorescence (TIRF) and scattering setup are shown, respectively. For fluorescence measurements a laser is used as the excitation source, where the beam is directed toward the objective with a dichroic mirror. The reflected excitation beam is then blocked, while the Stokes shifted emission passes through the dichroic and is collected by an electron multiplying charged coupled device (EMCCD; Andor iXon ultra 888, Andor Technology Ltd). For the TIR scattering setup the dichroic mirror is replaced with a beam splitter since the emission

wavelength and excitation wavelength are equal. Here, the reflected light from the excitation source is blocked by a crescent-shaped beam block underneath the objective. An LED light source is used, because of its lower coherence compared to lasers, decreasing interference artefacts originating from the many parallel interfaces in the beampath. In all experiments a 1.49 NA oil-immersion objective is used with a magnification of 100x.

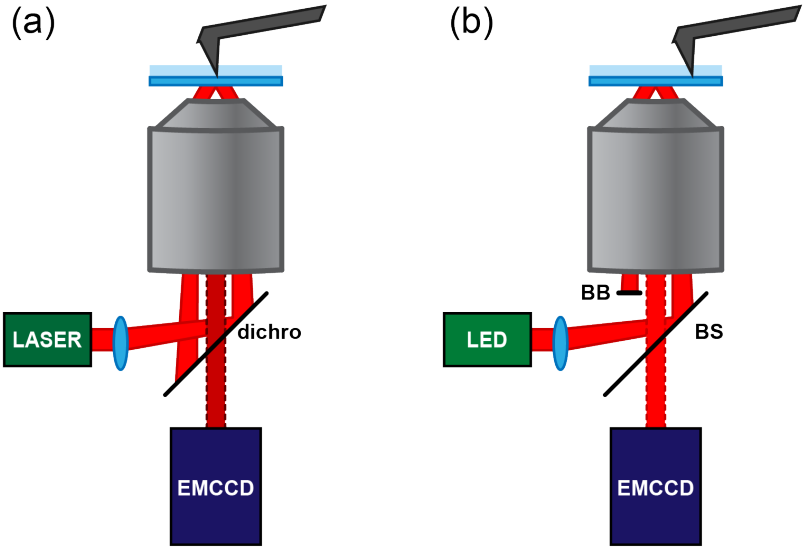

Figure 2.1 Correlative optical and atomic force microscopy setup. Samples can be imaged optically with wide-field detection in **(a)** a total internal reflection fluorescence microscopy setup or **(b)** a total internal reflection scattering microscopy setup. For fluorescence microscopy measurements a dichroic mirror is used to filter out the excitation light, for scattering microscopy the excitation and emission wavelength are the same and a beam block filters out the excitation beam. Here, a beam-splitter (BS) is used.

2.2.1 Correlated optical and atomic force microscope

To correlate AFM and optical images on one-and-the-same setup it is of utmost importance that the AFM tip is accurately aligned with the optical axis of the microscope. We typically align the EMCCD field-of-view with the AFM tip using the sample as a fiducial marker. The sample can be scattering, e.g. gold nanoparticles, or fluorescently labeled, e.g. biological or synthetic molecules.

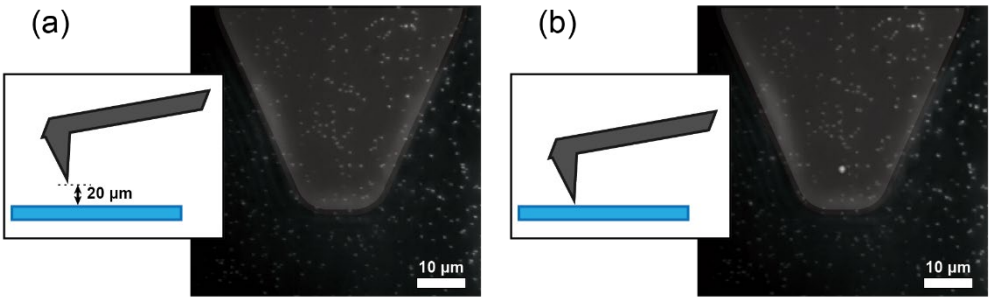

Figure 2.2 Alignment of the tip with respect to the sample. (a) Fiducial markers on a glass slide with an AFM tip 20 µm from the surface shows the shadow from the cantilever. The sample can be moved to select the area of interest. **(b)** The same sample with the tip lowered onto the surface. The AFM tip scatters the light from the evanescent field resulting in a bright spot at the exact location of the tip.

First the AFM head is placed on top of the stage and the cantilever is imaged on the camera in transmission, allowing for crude placement in the field-of-view (**Figure 2.2a**). After the crude alignment, the tip is engaged, i.e. lowered until the tip is in proximity to the surface. The tip scatters the evanescent field that excites the sample, which shows the tip position with respect to the sample, allowing to perform an AFM measurement on the desired location of the sample (**Figure 2.2b**). When the exact position of the AFM tip in the field of view is known, the tip can be retracted to select the required area of interest, and subsequently engaged to image this region.

2.3 Atomic force microscopy

Atomic force microscopy (AFM) is a scanning probe technique that employs a sharp tip that is scanned across the sample to map the sample topography. In **Figure 1.3** the basic layout of an AFM is sketched. The tip, with a nanometer-scale diameter, is connected to a flexible cantilever. Forces between the tip and the sample cause deflection of the cantilever. This deflection is measured by a laser reflected off the back of the cantilever onto a quadrant photodetector. To create a topographical image the sample is raster-scanned across areas up to 50 µm x 50 µm. The combination of nanoscale tip dimensions and the sensitive laser-based detection method allows for nanometer-scale resolution topographic measurements.

Although the vertical resolution in AFM is high,[1,2,3,4,5] the lateral resolution is not only determined by the tip diameter but more so by the convolution of the tip and the sample. The combination of the shape of the tip, usually conical or pyramidal, and the surface geometry leads to interactions between the tip and the surface resulting in decreased lateral resolution. Usage of high-aspect ratio tips such as such as carbon

nanotubes[6] have been used to circumvent this issue and obtain more accurate reconstruction of the surface topography.[7]

The AFM can be operated in different modes, each one with its own characteristics. The most commonly used modes (**Figure 2.3**) are contact mode (CM), non-contact mode (NCM), tapping mode (TP) and the one used in this thesis, peak force tapping mode (PFTM). Here, all modes and their respective characteristics, advantages and disadvantages are discussed briefly. In all modes a feedback mechanism is employed to obtain sample topography. Usually changes in cantilever deflection, oscillation amplitude, phase or frequency are used to create an image of sample topography.

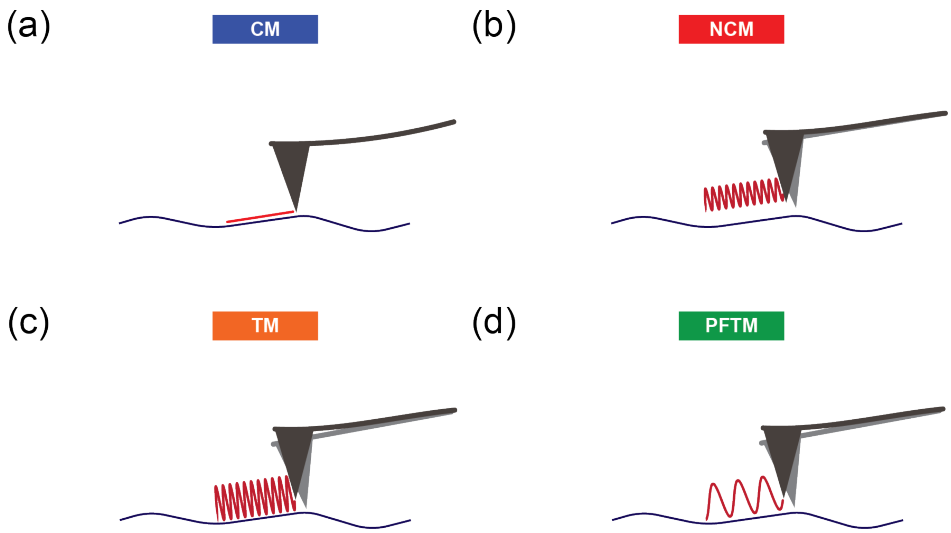

Figure 2.3 AFM modes. (a) In contact mode (CM) the tip moves laterally over the surface. Force or height is used as a feedback mechanism. **(b-c)** In non-contact (NCM) and tapping mode (TM) the cantilever is oscillated near the resonance frequency. For tapping mode the tip is closer to the surface than for non-contact mode. Cantilever amplitude or cantilever frequency is used as a feedback mechanism. **(d)** In peak force tapping mode (PFTM) the cantilever is oscillated at a much lower frequency than its resonance frequency. Maximum force is used as a feedback mechanism.

The AFM tip experiences forces depending mainly on the tip-sample distance and the cantilever stiffness. The spring constant k of the cantilever determines the sensitivity of the measurement. Low spring constants result in a higher resolution since small forces will produce a large cantilever deflection. However, simultaneously a high cantilever resonant frequency $f_0 = \frac{1}{2\pi}\sqrt{k/m_0}$, where m_0 is the effective mass loading the spring, is required to minimize sensitivity to vibrational noise.[8] The optimal spring constant therefore depends on the sample, cantilever and AFM mode.

The forces experienced by the AFM tip are distance-dependent and are shown in **Figure 2.4**. At atomic distances (a few angstroms) from the surface repulsive forces dominate due to the Pauli exclusion principle. Here, electron orbitals overlap resulting in repulsion between the atoms in the AFM tip and on the sample surface. Farther from the surface attractive van der Waals forces dominate. These forces can be described using the Lennard-Jones potential given by $U_{LJ} = \frac{B}{r^{12}} - \frac{C}{r^6}$, where B and C are constants and r is the distance from the surface.[9] The first term describes the repulsive component of the potential, whereas the second term represents the attractive van der Waals forces. The force exerted on the tip is given by the derivative of the potential (i.e. $F = -\nabla U$), which is plotted in **Figure 2.4**. The AFM modes differ mainly in their feedback system and as a consequence operate in different force regimes as indicated in **Figure 2.4**. Below we describe the working principle of the most commonly used AFM modes.

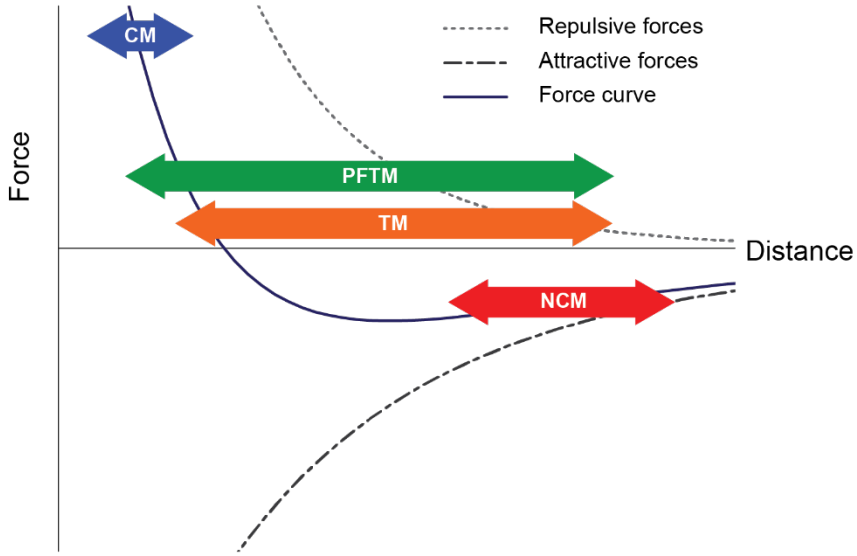

Figure 2.4 Force regimes for AFM scanning (forces are shown for the tip approaching the sample, dissipative forces due to adhesion not shown). Repulsive forces dominate close to the surface and are caused by overlapping electron orbitals, whereas attractive van der Waals forces become dominant as the distance increases. At very large distance the force is negligible. The force regime in which each of the four modes operates is indicated by the arrows.

2.3.1 Contact mode

In contact mode (**Figure 2.3a**) the tip is laterally "dragged" over the surface. Changes in the sample topography result in a change in the cantilever deflection due to repulsive tip-sample forces. This mode is operated in the repulsive force regime (**Figure 2.4**, blue arrow) and thus requires high forces to keep the tip close to the

surface. This makes it possible to image with atomic resolution, however due to high lateral forces this mode is only suited for mechanically rigid samples.

2.3.2 Non-contact mode

For softer samples contact mode results in sample damage due to the high shear forces. In non-contact (**Figure 2.3b**) mode the tip remains in the attractive regime (Figure **2.4**, red arrow), where it is mechanically excited near or on its resonance frequency. This is necessary because the attractive forces are smaller than the repulsive forces close to the surface and cannot be measured from cantilever deflection without a driven oscillation that allows for lock-in detection. For an oscillating cantilever, a change in tip-sample distance results in changes in the frequency[10] and/or amplitude of oscillation,[8,11] which is used as a feedback mechanism to map the sample topography. This results in lower forces on the sample compared to contact mode, since the cantilever is operated in the attractive regime only, preventing lateral tip-sample interactions and lowering vertical tip-sample maximum force. This does however require tight control to keep the tip in the right force regime. Stiffer cantilevers are used in non-contact mode (20-40 N/m) compared to contact mode (~0.2 N/m), as well as large oscillation amplitudes (>10 nm), to prevent the tip from snapping into the sample.[9] Furthermore, the van der Waals force gradient required for atomic resolution extends only about a nanometer from the sample surface. The present fluid layer, i.e. for measurements in air, is usually thicker than this distance complicating high-resolution measurements in air.

2.3.3 Tapping mode

Tapping mode (**Figure 2.3c**) employs the same feedback mechanism as non-contact mode, but the amplitude is increased to about 100-200 nm and it is operated at the boundary of the attractive and repulsive force regimes (**Figure 2.4**, orange arrow). It was introduced by Zhong *et al.*[12], who deliberately let the AFM 'tap' the surface intermittently. This results in higher resolution images and vastly reduced lateral forces compared to contact mode. Impact force is higher than for non-contact mode, but since the tip only touches the sample intermittently sample damage is reduced compared to contact mode. Frequencies for tapping mode range from 50 kHz to 0.5 MHz, depending on the type of cantilever.

In tapping mode, the phase difference between cantilever oscillation and driver oscillation can be measured. This allows for phase measurements providing additional material-dependent information (e.g. variations in composition and viscoelasticity) in addition to the topography image measured using cantilever amplitude as a feedback mechanism.[13] Amplitude decreases upon decreased tip-sample distance, i.e. a

protrusion or bump in the sample surface, and vice versa for increased tip-sample distance. Tip-sample separation is then adjusted to maintain constant amplitude of oscillation.

The main advantage of tapping mode over both contact and non-contact mode is the high oscillation frequency and amplitude which reduces adhesion forces and prevents the tip from sticking to the surface. In air the surface containing a thin viscoelastic fluid layer appears stiff due to the high oscillation frequency, and the large amplitude is able to overcome the adhesion forces when pulling the tip away from the surface. In fluid, the oscillation amplitude is decreased compared to air, but the mode is operated similarly with the exception of lower spring constants (typically ~0.1 N/m) than in air (1-100 N/m). In tapping mode multiple periods are required to generate a feedback sample, that means that when the sample height changes there is a delay in the feedback. This may result in a large peak force applied on the sample, and sample deformation or damage as a result, especially for soft samples.

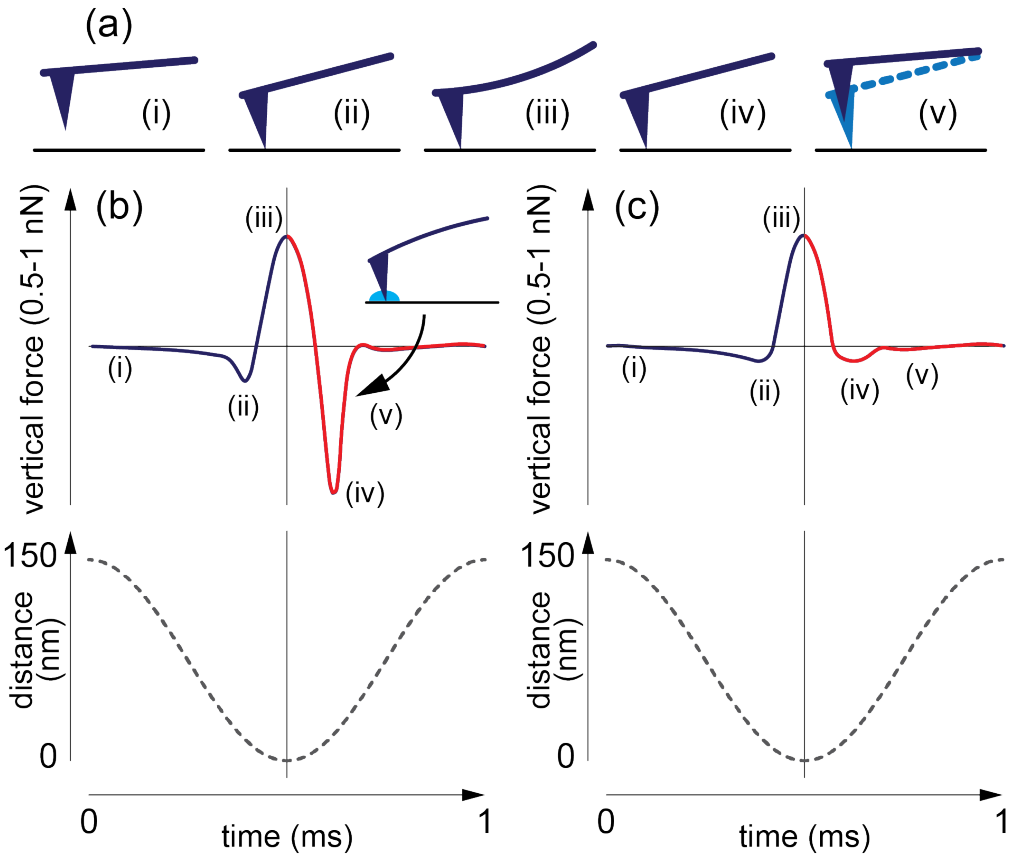

Figure 2.5 Force and tip-surface distance as a function of time in peak force tapping mode. (a) Different stages in the approach and withdrawal of the AFM tip. **(b)** Vertical force as a function of time in air and the

corresponding tip-sample distance. Adhesion forces due to small quantities of liquid on the surface require force to withdraw the tip (inset). **(c)** Vertical force as a function of time in liquid and the corresponding tip-sample distance.

2.3.4 Peak force tapping mode

Peak force tapping mode (**Figure 2.3d**) can be described as a combination of contact mode and tapping mode, where it combines advantages of both techniques. Peak force tapping mode is operated in the same force regime as tapping mode, but in contrast to tapping mode, the cantilever is actuated at a frequency much lower than its resonance frequency (~1 kHz). The actuation is sufficiently slow that the maximum force (i.e. cantilever deflection) can be used directly as a feedback mechanism, similarly to contact mode. This direct force control makes this mode ideal for very soft samples including biomolecules, since the set force is not exceeded, in contrast to tapping mode, where the delay in feedback can result in high forces that may deform or damage the sample.

In this thesis peak force tapping mode was used in all AFM measurements. In **Figure 2.5a** the approach and retraction of the cantilever is shown together with the force and tip-sample distance as a function of time in air (**Figure 2.5b**) and liquid (**Figure 2.5c**). In each cycle the tip is lowered towards the sample surface, where the cantilever deflection is zero (i). At close proximity the tip experiences attractive van der Waals forces and thus a negative force (ii), as the tip comes closer the repulsive forces start to dominate and the tip is deflected as the force increases up to the force set-point (iii). The vertical cantilever position at this moment is used to construct the topography of the sample. The tip is then retracted decreasing cantilever deflection (iv). Due to adhesion forces the tip is deflected resulting in a negative force, which is large in air due to the liquid layer on the sample. In water the dip in the force curve is due to attractive forces only (v). Tapping mode allows for sub-nN forces with a tapping amplitude of ~150 nm. Peak force tapping mode has been applied to biological samples such as amyloid polymers[14] and membrane proteins.[15,16] Furthermore, due to its low actuation frequency (~1 kHz) compared to tapping mode a force curve can be measured for each cycle[17,18] and thus at each pixel.

2.4 Characterization of AFM on soft samples

The intermittent contact the tip makes with the sample in both tapping mode and peak force tapping mode vastly decreases deformation and damage compared to contact mode, because of the decreased normal force and absence of lateral forces. Nevertheless, the lack of direct force control in tapping mode can still result in sample damage or sample deformation of soft samples when the tip comes into contact with

the surface. In peak force tapping mode the maximum force is controlled, eliminating the possible force peaks due to the slight delay in feedback for tapping mode.

However, we note that for imaging with low forces low spring constant cantilevers are required. These are difficult to operate, because the required cantilever deflection at the surface is often already met due to interaction with the fluid layer on the sample surface. This makes imaging with forces below 500 pN challenging.

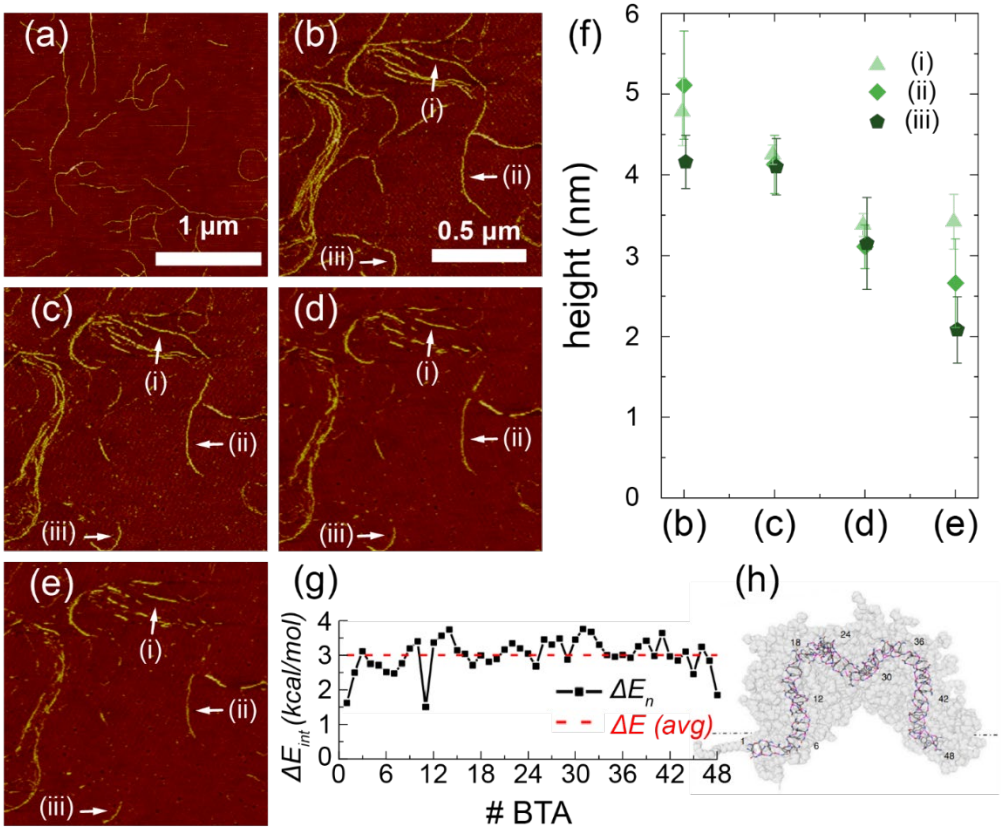

Figure 2.6 Peak force tapping mode measurements on soft supramolecular polymers. (a) AFM image of CBT derivatives. **(b)** AFM image of BTA polymers. The same field of view after two **(c)**, three **(d)** and four **(e)** scans. **(f)** Height of BTA polymers as a function of number of scans. The height is reduced in all three regions. In (a-d) sample damage is visible, as parts of polymer are swept away after each scan. The peak force used for all scans was 500 pN. **(g)** Self-assembly interaction energy of individual BTA molecules. The corresponding molecular dynamics simulation snapshot is shown in **(h)**. (g) and (h) are adapted from [21].

AFM was performed on two different supramolecular polymers. These self-assemble through non-covalent interactions and can therefore be categorized as soft materials. We image carbonyl-bridged triarylamine (CBT) 2,6,10-trisamides, where the CBT core consists of three arylamide groups, bridged by three carbonyl groups from which three side-chains extend,[19] and 1,3,5-benzene-tricarboxamide (BTA) motifs,

consisting of a benzene ring with three side-chains originating from three carboxamide groups.[20] Both monomers possess three hydrogen bonding amide groups, to which a benzene ring with three aliphatic groups is bound for the CBT derivatives,[19] and an aliphatic side chain with four hydrophilic polyethylene glycol groups for the BTA monomers.[20]

BTA monomers self-assemble through hydrogen bonding and hydrophobic interactions, while CBT monomers self-assemble through pi-pi stacking, hydrogen bonding and hydrophobic interactions. The larger core and the pi-pi stacking results in a stronger interaction energy of -29 kJ/mol at room temperature for CBT derivates[19] compared to -12.5 kJ/mol for BTA.[21] The CBT polymers have a diameter of 3.9 nm,[19] whereas BTA polymers are 6.2 nm in diameter.[21] However, compared to DNA, with an interaction energy of 58 - 78 kJ/mol for the stacking interaction and 135 – 288 kJ/mol for the interbase hydrogen bonding depending on the base pairs,[22] and a diameter of 2 nm, both can be considered extremely soft. Also, molecular dynamics simulations of the BTA polymers show local defects where the interaction energy is up to a factor of 3 lower (**Figure 2.6g** and **h**).

These defects weaken the structural integrity of the polymer and increase the probability of sample damage in AFM. Adsorption of BTA to a glass surface also proved challenging. Hydrophobic coatings, i.e. silanes with alkyl chains, result in disassembly of the BTA polymers, while charged coatings, i.e. (3-aminopropyl)triethoxysilane (APTES) result in BTA polymer aggregation. BTA was eventually found to reliably adsorb to piranha-treated glass coverslips, which creates a hydroxylated surface. This adsorption is relatively weak as evidenced by occasional desorption of BTA polymers, making AFM imaging more challenging. This trade-off between adsorption strength and BTA polymer integrity makes peak-force tapping mode essential for imaging, even though the weak adsorption, its dynamic character and defects may result in sample damage during AFM measurements. Nevertheless, we are able to image BTA polymer using the direct force control of peak force tapping mode.

In **Figure 2.6a** and **b** we show AFM data of both polymers using peak force tapping mode measured with a force setpoint of 500 pN. In **Figure 2.6b-e** we quantify sample stability in peak force tapping mode by repeatedly measuring the diameter of several polymers that are adsorbed on a piranha-treated glass coverslip. At locations (i), (ii) and (iii), depicted in **Figure 2.6b-e**, a reduction in height was observed and monitored after each scan. In **Figure 2.6f** the height for the three locations is shown after each scan b-e, where for all locations a slight reduction in polymer height is observed which was accompanied by a slightly increased width (not shown). Besides sample deformation, some sections are swept away. This is likely caused by the weak polymer-substrate

interaction that was required to prevent disintegration of the polymer upon immobilization. Although imaging in contact mode and tapping mode was not possible without drastic alteration of the polymer geometry, even these fragile supramolecular polymers can be imaged in peak force tapping mode. In **Chapter 3** we will discuss peak-force tapping AFM of these BTA supramolecular polymers in more detail.

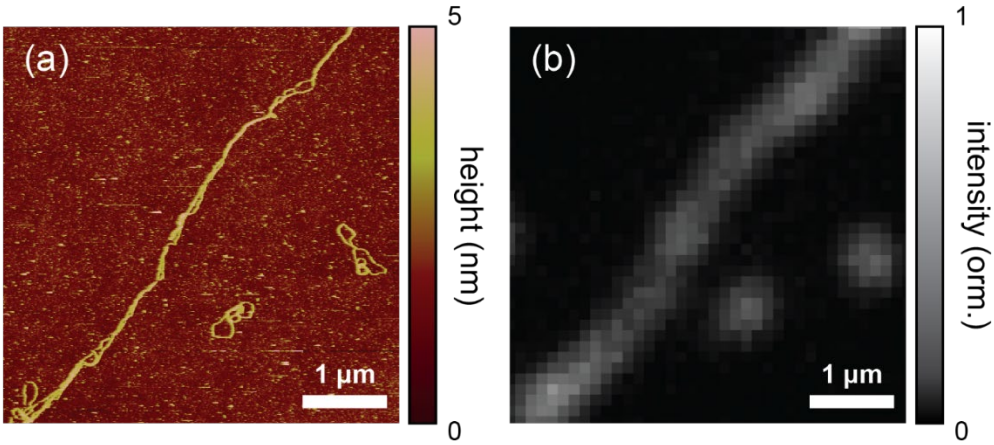

Figure 2.7 Correlated microscopy images of supramolecular polymers. (a) Peak force tapping mode AFM image of a supramolecular polymer. **(b)** TIRF image of the same polymer.

In **Figure 2.7** an example of a correlated AFM and TIRF measurement is shown. The AFM image, obtained with peak force tapping mode, of a Cy5-labeled supramolecular polymer (**Figure 2.7a**) shows a long clustered and entangled polymer and two curled-up polymers. The same curling is also present at the end of the entangled polymer in the left lower corner of the image. In the next chapter this will be discussed as well as why the correlated imaging is of added value for these polymers. The correlated fluorescent image (**Figure 2.7b**) shows the same polymers at diffraction-limited resolution. Here, the intensity is related to the local fluorophore density, which will also be discussed further in the next chapter.

2.5 High-throughput optical spectroscopy

In the majority of correlated microscopy setups two imaging modalities (e.g. optical and atomic force microscopy, or optical and electron microscopy) are combined. In this thesis we add another modality, namely optical spectroscopy. In spectroscopy the

interaction with matter and electromagnetic radiation is investigated by measuring the wavelength- or energy dependent radiation emitting from or interacting with a sample.[23] To measure spectra of samples in a microscopy setup different methods can be used. Here, we discuss commonly used techniques such as measurements with a spectrometer, with a grating (diffraction) or prism (refraction) in front of the camera, Fourier transform spectroscopy, hyperspectral cameras and hyperspectral microscopy.

A spectrometer is a device in which a light beam passes through a slit after which a grating diffracts the beam into its wavelength components to produce a spectrum (**Figure 2.8a**). This is a broadly applicable approach wherein the light emitted from a region of interest (with e.g. a single emitter) is directed into the spectrometer. Spectroscopy of single metal nanoparticles can for example be used to study the relation between the spectral linewidth and particle geometry[24] or the spectra of exotic shapes, such as star-shaped nanoparticles.[25] However, when using a spectrometer for single molecule or particle measurements a disadvantage is the low throughput, because only a single (or at most a few) particle's or molecule's spectrum can be measured at one time. Also, to ensure that only the emission from a single particle enters the spectrometer, a low density sample is required, making the gathering of statistics time consuming.

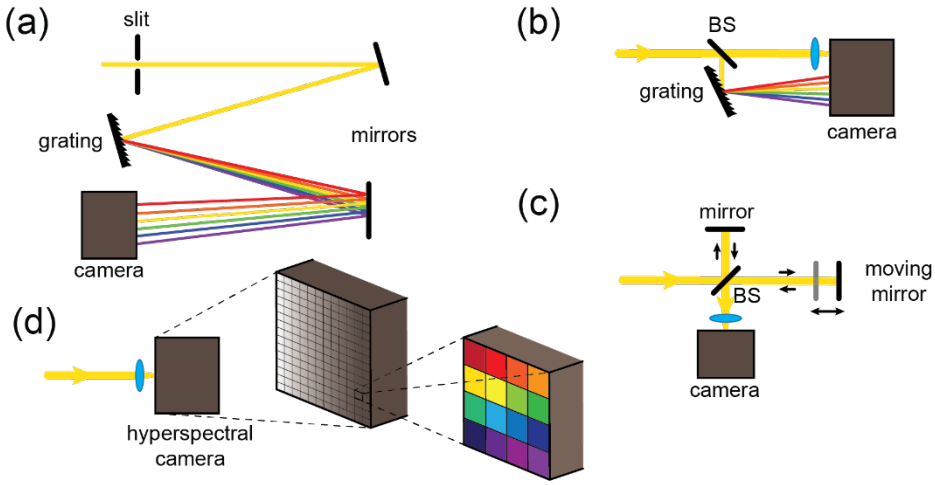

Figure 2.8 Schematic working principles for different spectroscopy techniques. (a) Spectrometer. The emission passes through a slit where it is directed onto a grating and the spectra are recorded by an array detector. **(b)** Combined spectral and wide-field imaging. The emission beam is split by a beam splitter (BS), where one beam is collected by the camera and the other beam is split into its wavelength components by the grating and projected onto the other half of the detector area. **(c)** Fourier transform spectroscopy. The beam is split in two by a beam splitter (BS), one beam is reflected by a stationary mirror, the other by a moving mirror. The mirror is moved and the arm length dependent interference intensity is collected by a camera. **(d)** Hyperspectral camera. The beam is focused onto the detector, where each pixel has a narrow

bandwidth wavelength filter. This effectively reduces the resolution and intensity, but provides high temporal resolution wide-field spectral images.

Alternatively, spectra and wide-field imaging can be combined in a dual image (**Figure 2.8b**). This allows for simultaneous wide-field imaging of a fluorescently-labeled sample or scattering sample and its spectra. The emitted light can e.g. be split using a beam splitter, where one beam path is directly projected onto a camera and the other passes through a grating or prism before being projected onto the other half of the camera's field of view. Such implementations have been used for spectrally-resolved point accumulation for imaging in nanoscale topography (srPAINT), where a fluorescent ligand binds and unbinds from the sample. Here, the additional spectral dimension provides environmental information when using solvatochromic dyes, in addition to their location (**Figure 2.8b**),[26] and can e.g. be used to map plasma-membrane organization.[27] Similar methods have been employed to image mitochondria and microtubules in cells by simultaneously recording the spectra of two different dyes in one frame. This yields a 3D spatial image of differently labeled structures in one measurement.[28,29] Instead of a grating the use of a prism achieves the same purpose,[30] which has been used for example to map point defects in boron nitride.[31] Though grating- or prism-based approaches deliver a wealth of information in a single measurement with a higher throughput compared to spectrometer measurements, low density samples are still required to prevent spatial overlap between the spectra of nearby emitters on the camera. Also, the field of view is split between the spectral and spatial data, reducing the field-of-view.

A third method to acquire spectra is Fourier transform spectroscopy. Here, the emitted light is split, where one beam path includes a movable mirror to introduce a path-length difference (**Figure 2.8c**). By modulating the path-length difference and letting the signal- and reference-beam interfere the detected intensity is also modulated. For a monochromatic beam the signal is a sine, where the period of the sine is the wavelength. For a multicomponent spectrum the signal will be a superposition of sines and using a Fourier transform the spectral information can be obtained.[32] Fourier transform spectroscopy has for example been applied to gold nanorods to measure their spectra,[33] but can also be used as a tool to identify biological tissues.[34] However, compared to grating measurements, Fourier interferometry is time consuming, because it requires the arm length to be varied with a fine stepsize.

A more straightforward method of obtaining spectra are hyperspectral methods. Here, filters are used to measure intensity at different wavelength bands, from which the spectrum is reconstructed by plotting the intensity as function of the center wavelength of the bandpass filter. Hyperspectral cameras are available, where a filter is placed in front of each camera pixel, as well as hyperspectral microscopy, where different filters filter the emitted light before it reaches the camera. Also methods have

been developed where the signal from each point on the image passes through a prism and is captured by a large EMCCD camera to find the spectrum for each point.[35]

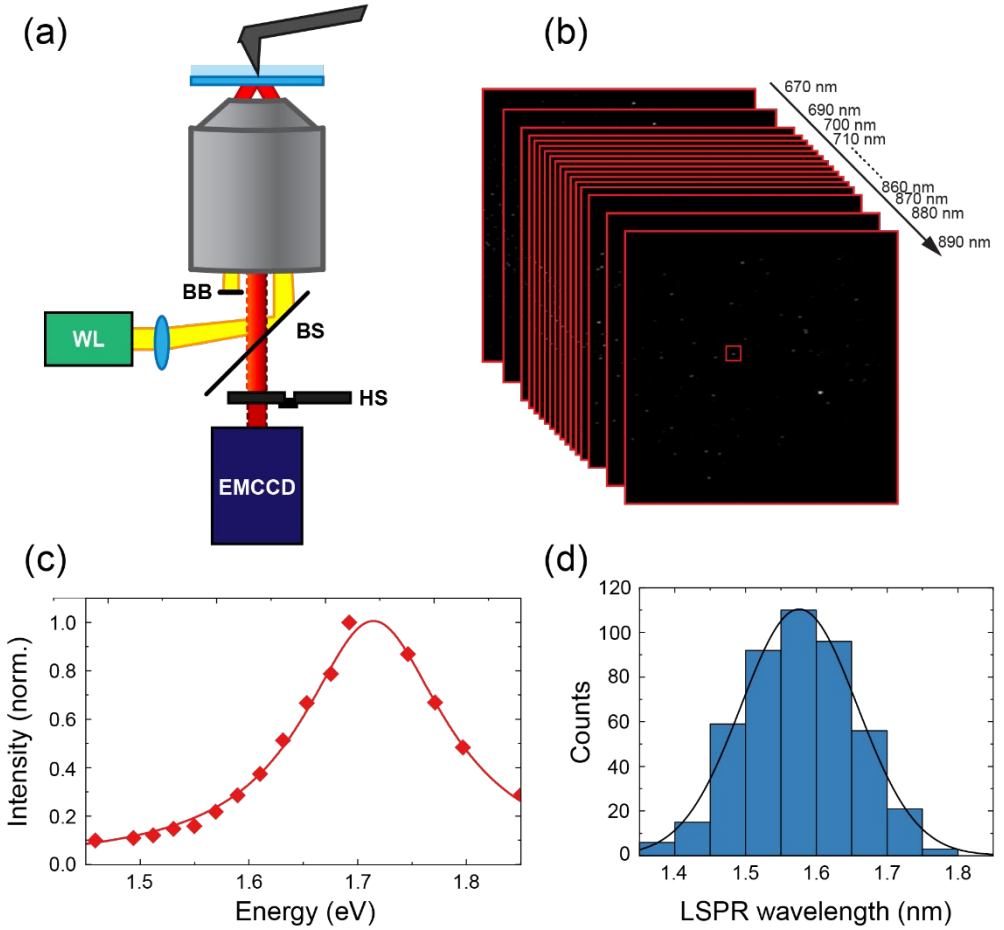

Figure 2.9 (a) Hyperspectral microscopy setup. A white light source excites the sample via a beam-splitter. The emitted light is filtered using a hyperspectral wheel with narrow bandwidth filters. **(b-c)** Principle of hyperspectral microscopy. Wide-field images of gold nanoparticles were taken while changing the 10 nm-bandwidth filter in front of the detector. The signal for each filter wavelength is determined to obtain single-particle spectra. Each spectrum **(c)** is fitted with a Lorentzian function to determine the center wavelength and linewidth of each particle in the field of view. **(d)** Histogram of nanorod LSPR wavelength obtained from Lorentzian fitting with a Gaussian fit yields a LSPR wavelength of 714 ± 26 nm.

For hyperspectral cameras the main downside is the decreased spatial resolution when the number of color channels increases. Twenty different color channels will result in a 20-fold reduction in resolution because each pixel is associated with only one color channel. This also results in a reduction of the signal-to-noise ratio because only a fraction of the total emission at a certain wavelength passes through the matching color pixel.

An alternative approach, the one employed in this thesis, is not to integrate the filters on the camera chip but rather to use bandpass filters in the detection path. This method is dubbed hyperspectral microscopy, and requires the bandpass filter in the detection path to be changed to reconstruct a full spectrum. This enables us to use the full camera resolution for imaging, and is still a very fast method compared to spectrometers or FTIR because a filter change can be using for example an acousto-optic tunable filter if needed.[36] The only requirement for hyperspectral microscopy is that single particles or molecules are further apart than the diffraction limit to be spatially resolved on the camera.

In this thesis we use such hyperspectral microscopy to record spectra of plasmonic assemblies. Here, an incoherent white-light source excites the sample through total internal reflection and the scattered light passes through a hyperspectral wheel (**Figure 2.9a**) that contains multiple narrow-bandwidth filters. By mapping the intensity of the sample in a wide-field image as a function of filter wavelength (**Figure 2.9b**) the spectra (**Figure 2.9c**) of many particles are measured simultaneously.

The main advantages of hyperspectral imaging are its ease of use and high throughput, since only dielectric interference filters are required. Also, the amount of data that is gathered from a single measurement allows for robust statistical analysis. For example, the spectra obtained from the filtered intensity of the particles (red diamonds, **Figure 2.9c**) in **Figure 2.9b** were fitted with a Lorentzian function (solid red line, **Figure 2.9c**) to yield the center wavelength and the full width at half maximum, or linewidth. In **Figure 2.9d** the resulting histogram shows the distribution yielding an average center wavelength of 714 ± 26 from a Gaussian fit to the data. In the next paragraph other spectroscopy methods are discussed and compared to hyperspectral microscopy to show their advantages and disadvantages with respect to this technique.

References

1. Giessibl, F. J.; Hembacher, S.; Bielefeldt, H.; Mannhart, J. Subatomic features on the silicon (111)-(7x7) surface observed by atomic force microscopy. *Science*, **2000**, *289*, 422-425.
2. Giessibl, F. J.; Bielefeldt, H.; Hembacher, S.; Mannhart, J. Imaging of atomic orbitals with the atomic force microscope – experiments and simulations. *Ann. Phys.*, **2001**, *10*, 887-910.
3. Hembacher, S.; Giessibl, F. J.; Mannhart, J. Force microscopy with light-atom probes. *Science*, **2004**, 305, 380-383.
4. Gross, L.; Mohn, F.; Moll, N.; Liljeroth, P.; Meyer, G. The chemical structure of a molecule resolved by atomic force microscopy. *Science*, **2009**, *325*, 1110-1114.
5. Welker, J.; Giessibl, F. J. Revealing the angular symmetry of chemical bonds by atomic force microscopy. *Science*, **2012**, *336*, 444-449.
6. Hafner, J. H.; Cheung, C-L.; Woolley, A. T.; Lieber, C. M. Structural and functional imaging with carbon nanotube AFM probers. *Prog. Biophys. Mol. Biol.*, **2001**, *77*, 73-110.
7. Canet-Ferrer, J.; Coronado, E.; Forment-Aliaga, A.; Pinilla-Cienfuegos, E. Correction of the tip convolution effects in the imaging of nanostructures studied through scanning force microscopy. *Nanotechnology*, **2014**, *25*, 395703.
8. Binnig, G.; Quate, C. F.; Gerber, Ch. Atomic force microscope. *Phys. Rev. Lett.*, **1986**, *56*, 930-934.
9. Giessibl, F. J. Forces and frequency shifts in atomic-resultion dynamic force microscopy. *Phys. Rev. B*, **1997**, *56*, 16010-16015.
10. Albrecht, T. R.; Grütter, P.; Horne, D.; Rugar, D. Frequency modulation detection using high-Q cantilevers for enhanced force microscope sensitivity. *J. Appl. Phys.*, **1991**, *69*, 668-673.
11. Martin, Y.; Williams, C. C.; Wickramasinghe, H. K. Atomic force microscope-force mapping and profiling on a sub 100-Å scale. *J. Appl. Phys.*, **1987**, *61*, 4723-4729.
12. Zhong, Q.; Inniss, K.; Elings, V. B. Fractured polymer/silica polymer surface studied by tapping mode atomic force microscopy. *Surf. Sci. Lett.*, **1993**, *290*, L688-L692.
13. Schmitz, I.; Schreiner, M.; Friedbacher, G.; Grasserbauer, M. Phase imaging as an extension to tapping mode AFM for the identification of material properties on humidity-sensitive surfaces. *Appl. Surf. Sci.*, **1997**, *115*, 190-198.
14. Adamcik, J.; Berquand, A.; Mezzenga, R. Single-step direct measurement of amyloid fibrils stiffness by peak force quantitative nanomechanical atomic force microscopy. *Appl. Phys. Lett.*, **2011**, *98*, 193701.
15. Rico, F.; Su, C.; Scheuring, S. Mechanical mapping of single membrane proteins at submolecular resolution. *Nano Lett.*, **2011**, *11*, 3983-3986.
16. Medalsy, I.; Hensen, U.; Muller, D. J. Imaging and quantifying chemical and physical properties of native proteins at molecular resolution by force-volume AFM. *Angew. Chem. Int. Ed.*, **2011**, *50*, 12103.
17. Sweers, K.; Van der Werf, K.; Bennink, M.; Subramaniam, V. Nanomechanical properties of α-synuclein amyloid fibrils: a comparative study by nanoindentation, harmonic force microscopy and Peakforce QNM. *Nanoscale Res. Lett.*, **2011**, *6*, 270.
18. Dokukin, M. E.; Sokolov, I. Quantitative mapping of the elastic modulus of soft material with HarmoniX and PeakForce QNM AFM modes. *Langmuir*, **2012**, *28*, 16060-16071.
19. Haedler, A. T.; Meskers, S. C. J.; Zha, R. H.; Kivala, M.; Schmidt, H-W.; Meijer, E. W. Pathway complexity in the enantioselective self-assembly of functional carbonyl-bridged triarylamamine trisamides. *J. Am. Chem. Soc.*, **2016**, *138*, 10539-10545.
20. Albertazzi, L.; Van der Zwaag, D.; Leenders, C. M. A.; Fitzner, R.; Van der Hofstad, R. W.; Meijer, E W. Probing exchange pathways in one-dimensional aggregates with super-resolution microscopy. *Science*, **2014**, *344*, 491-495.
21. Baker, M. B.; Albertazzi, L.; Voets, I. K.; Leenders, C. M. A.; Palmans, A. R. A.; Pavan, G. M.; Meijer, E. W. Consequences of chirality on the dynamics of a water-soluble supramolecular polymer. *Nat. Commun.*, **2015**, *6*, 6234.
22. Fukuzawa, K.; Watanabe, C.; Kurisaki, I.; Taguchi, N.; Mochizuki, Y.; Nakano, T.; Tanaka, S.; Komeiji, Y. Accuracy of the fragment molecular orbital (FMO) calculations for DNA: total energy, molecular orbital, and inter-fragment interaction energy. *Computational and theoretical chemistry*, **2014**, *1034*, 7-16.

23. Herrmann, R.; Onkelinx, C. Quantities and units in clinical chemistry: nebulizer and flame properties in flame emission and absorption spectrometry. *Pure Appl. Chem.*, **1986**, *58*, 1737-1743.
24. Hu, M.; Novo, C.; Funston, A.; Wang, H.; Staleva, H.; Zou, S.; Mulvaney, P.; Xia, Y.; Hartland, G. V. Dark-field microscopy studies of single metal nanoparticles: understanding the factors that influence the linewidth of the localized surface plasmon resonance. *J. Mater. Chem.*, **2008**, *18*, 1949-1960.
25. Nehl, C. L.; Liao, H.; Hafner, J. H. Optical properties of star-shaped gold nanoparticles. *Nano Lett.*, **2006**, *6*, 683-688.
26. Bongiovanni, M. N.; Godet, J.; Horrocks, M. H.; Tosatto, L.; Carr, A. R.; Wirthensohn, D. C.; Ranasinghe, R. T.; Lee, J-E.; Ponjavic, A.; Fritz, J. V.; Dobson, C. M.; Klenerman, D.; Lee, S. F. Multi-dimensional super-resolution imaging enables surface hydrophobicity mapping. *Nat. Commun.*, **2016**, *7*, 13544.
27. Danylchuk, D. I.; Moon, S.; Xu, K.; Klymchenko, A. S. Switchable solvatochromic probes for live-cell super-resolution imaging of plasma membrane organization. *Angew.Chem. Int. Ed.*, **2019**, *58*, 1-6.
28. Song, K-H.; Zhang, Y.; Wang, G.; Sun, C.; Zhang, H. F. Three-dimensional biplane spectroscopic single-molecule localization microscopy. *Optica*, **2019**, *6*, 709-714.
29. Zhang, Y.; Song, K-H.; Dong, B.; Davis, J. L.; Shao, G.; Sun, C.; Zhang, H. F. Multicolor super-resolution imaging using spectroscopic single-molecule localization microscopy with optimal spectral dispersion. *Appl. Opt.*, **2019**, 58, 2248-2255.
30. Huang, T.; Phelps, C.; Wang, J.; Lin, L-J.; Bittel, A.; Scott, Z.; Jacques, S.; Gibbs, S. L.; Gray, J. W.; Nan, X. Simultaneous multicolor single-molecule tracking with single-laser excitation via spectral imaging. *Biophys. J.*, **2017**, *114*, 301-310.
31. Comtet, J.; Glushkov, E.; Navikas, V.; Feng, J.; Babenko, V.; Hofmann, S.; Watanabe, K.; Taniguchi, T.; Radenovic, A. Wide-field spectral super—resolution mapping of active defects in hexagonal boron nitride. *Nano Lett.*, **2019**, *19*, 2516-2523.
32. Horlick, G. Introduction to Fourier transform spectroscopy. *Appl. Spectrosc.*, **1968**, *22*, 617-626.
33. Kollmann, H.; Esmann, M.; Wtt, J.; Markovic, A.; Smirnov, V.; Wittstock, G.; Sillies, M.; Lienau, C. Fourier-transform spatial modulation spectroscopy of single gold nanorods. *Nanophotonics*, **2018**, *7(4)*, 715-726.
34. Movasaghi, Z.; Rehman, S.; Rehman, I. U. Fourier Transform Infrared (FTIR) spectroscopy of biological tissues. *Appl. Spectros. Rev.*, **2008**, *43*, 134–179.
35. Gao, L.; Kester, R. T.; Hagen, N.; Tkaczyk, T. S. Snapshot image mapping spectrometer (IMS) with high sampling density for hyperspectral microscopy. *Optics Express*, **2010**, *18*, 14330-14344.
36. Fairbairn, N.; Christofidou, A; Kanaras, A. G.; Newman, T. A.; Muskens, O. L. Hyperspectral darkfield microscopy of single hollow nanoparticles for biomedical applications. *Phys. Chem. Chem. Phys.*, **2013**, *15*, 4163-4168.

Chapter 3

Mechanical properties of single supramolecular polymers from correlative AFM and fluorescence microscopy

We characterize the structure and mechanical properties of 1,3,5-benzenetricarboxamide (BTA) supramolecular polymers using correlative AFM and fluorescence imaging. AFM allows for nanoscale structural investigation but we found that statistical analysis is difficult because these structures are easily disrupted by the AFM tip. We therefore correlate AFM and fluorescence microscopy to couple nanoscale morphological information to far-field optical images. A fraction of the immobilized polymers are in a clustered or entangled state, which we identify based on diffraction limited fluorescence images. We find that clustered and entangled polymers exhibit a significantly longer persistence length that is broader distributed than single unentangled polymers. By comparison with numerical simulations we find significant heterogeneity in the persistence length of single unentangled polymers, which we attribute to polymer–substrate interactions and the presence of structural diversity within the polymer.

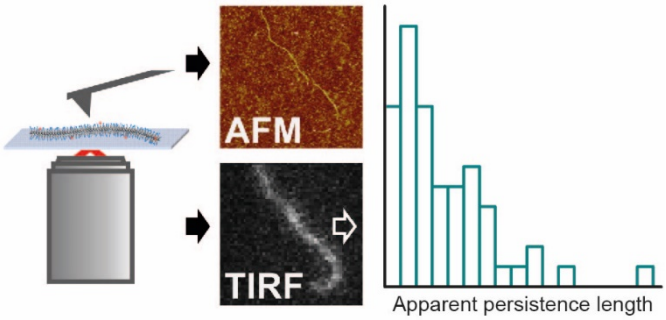

This chapter has been published as: Beuwer, M. A.; Knopper, M. F.; Albertazzi, L.; Van der Zwaag, D.; Ellenbroek, W. G.; Meijer, E. W.; Prins, M. W. J.; Zijlstra, P. Mechanical properties of single supramolecular polymers from correlative AFM and fluorescence microscopy. *Polym. Chem.*, **2016**, *7*, 7260-7268.

3.1 Introduction

Here we apply the correlative approaches from the first two chapters to study the mechanical properties of single supramolecular polymers. The fluorescent labelling here provides chemically specific information on micrometer length scales, while the AFM imaging provides structural information on nanometer length scales.

Most polymers are one-dimensional (1D) chains of many units that are connected by covalent bonds. In supramolecular polymers on the other hand the units are connected by non-covalent interactions, e.g. π-π stacking, hydrogen bonds, electrostatic and hydrophobic interactions.[1] Biological supramolecular polymers, such as actin filaments and microtubules, are of major importance to cell structure, migration and differentiation.[2] The unique properties of these biological polymers have sparked interest into bio-inspired supramolecular materials. These synthetic materials have been applied as biocompatible agents for drug delivery and scaffolds for tissue engineering,[1,3,4,5,6,7,8,9] as self-healing additives that prevent misting and reduce drag in engines,[10] and as semiconducting nanotubes in molecular electronics.[1] These applications rely on the polymer's dynamic and responsive behaviour that arises due to the non-covalent nature of the monomer interactions.

In the past few decades the assembly of 1,3,5-benzenetricarboxamide (BTA) polymers has been studied in great detail.[11,12,13] BTA polymers are an example of synthetic supramolecular polymers and can be engineered to different applications by modifying the monomer structure. In **Figure 3.1a** the BTA monomer is shown with its different regions. A benzene ring with three carboxamide groups forms the core of the monomer (orange region), allowing for stacking by the formation of triple hydrogen bonds between adjacent monomers. In water, polymerization is driven by the aggregation of hydrophobic chains (yellow region) between nearby monomers. The hydrophilic terminal groups, composed of four polyethylene glycol groups, ensure the polymer's solubility in water. A cartoon representation of a BTA polymer is shown in **Figure 3.1b**. Self-assembly and solubility in aqueous solutions makes BTA polymers compatible with biological environments. BTA polymers have been applied as drug delivery agents,[14] MRI contrast reagents,[15] in organogels[16] and hydrogels[17] and as self-healing materials.[18] The difficulty in predicting polymer properties based on the monomer structure has sparked efforts to characterize the physical properties of supramolecular polymers. Ensemble-averaged techniques such as UV-VIS spectroscopy,[11,19] circular dichroism,[11,19,20,21,22.23] and fluorescence emission[24] as well as small-angle X-ray scattering (SAXS)[25] have been applied.

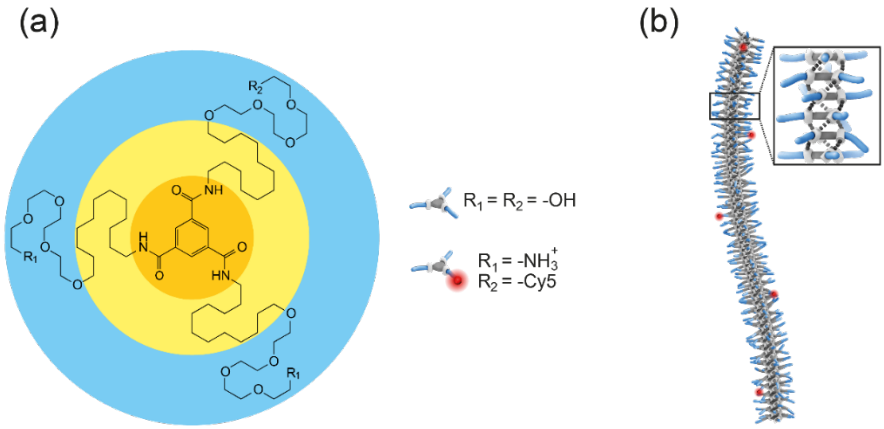

Figure 3.1 Structure of water-soluble 1,3,5-benzene-tricarboxamide (BTA). (a) Chemical structure of BTA monomer. In a stack, the BTA core (orange) forms triple hydrogen bonds with neighboring monomers. Three side-chains with alkane groups (yellow) give rise to hydrophobic interactions and polyethylene glycol (PEG) groups (blue) provide water-solubility. A fraction of the monomers (2%) are labelled with a fluorescent dye (Cy5). **(b)** Cartoon representation of a BTA polymer with Cy5-labeled monomers. Hydrogen bonds are illustrated by dashed lines in the inset.

Although these techniques give a wealth of information, single-polymer methods are able to discern rare states and reveal distributions of molecular properties instead of averages. Single immobilized BTA polymers have been studied mostly by optical techniques.[26] Recently, super-resolution optical microscopy has shown that dynamic monomer exchange occurs homogeneously along the polymer backbone,[24,26] instead of solely at the polymer ends or by fragmentation–recombination. However, it remains difficult if not impossible to predict the mechanical properties of a supramolecular polymer based on its monomer structure.

Here we study the mechanical properties of single BTA supramolecular polymers using correlated AFM and fluorescence microscopy. Such correlated imaging benefits from the spatial resolution of AFM, and the chemical specificity and throughput of fluorescence microscopy. Although these fragile structures are easily disrupted by mechanical interactions with the AFM tip, we show that correlation of AFM and fluorescence microscopy allows for the reliable identification of nanoscale features such as clustering and entanglement of polymers based purely on diffraction limited fluorescence images. We apply this correlative approach to study the persistence length of individual polymers and compare our results to numerical simulations based on the worm-like chain model. We analyze the distribution of single-

polymer persistence lengths and discuss the underlying factors that induce inhomogeneous broadening.

3.2 Experimental and theoretical methods

3.2.1 Synthesis and preparation of BTA polymers

We studied water-soluble 1,3,5-benzentricarboxamide (BTA) motifs with amphiphilic side-chains that were synthesized and assembled as reported before.[11] In short, BTA monomers[11] (**Figure 3.1a**, R_1 = R_2 = -OH) and Cy5-labeled BTA monomers[26] (**Figure 3.1a**, R_1 = $-NH_3^+$, R_2 = -Cy5) were dissolved in methanol at a concentration of 10 mM and 1 mM, respectively. These solutions were subsequently mixed to obtain a ratio of Cy5-BTA to BTA of 0.02. The resulting solution in methanol was diluted in Milli-Q water to a final concentration of 25 µM. Dilution in Milli-Q water induces the self-assembly process through a combination of hydrophobic interactions and hydrogen bonds[11,19] The diameter of these BTA polymers in solution was reported to be 6.2 nm using SAXS.[27]

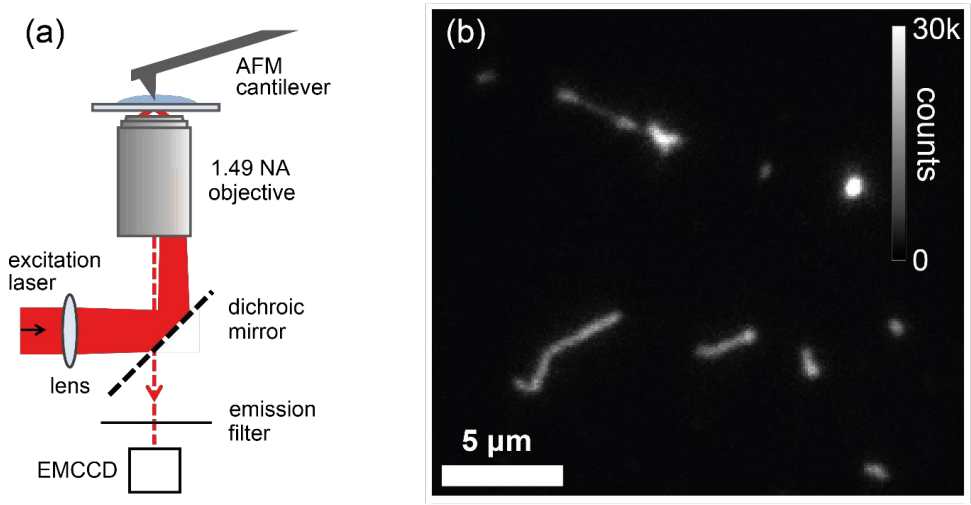

Figure 3.2 **(a)** Schematic of the combined total internal reflection fluorescence and AFM setup. **(b)** Fluorescence image of immobilized BTA polymers. Bright spots correspond either to polymers that are smaller than the diffraction limit or to clusters of entangled polymers.

3.2.2 Sample preparation

In our measurements BTA polymers were immobilized on glass substrates by physisorption. The coverslips (Menzel-Gläser) were first sonicated in acetone,

isopropanol and Milli-Q water for 5 minutes each, before incubating for 15 minutes in freshly prepared piranha etch (3:1 v/v H_2SO_4:H_2O_2 (30%)). Afterwards, the coverslips were sonicated in Milli-Q and acetone for 5 minutes each and dried under N_2-flow.

The solution of Cy5-BTA was further diluted to a monomer concentration of 5 μM using Milli-Q water. A droplet of diluted Cy5-BTA was dropcast on the piranha-etched coverslip and after 1 minute of incubation, unbound Cy5-BTA in solution was washed away with Milli-Q water. This resulted in several supramolecular polymers per field of view (100x100 μm^2), see **Figure 3.2b**.

All experiments were performed with a combined total internal reflection fluorescence (TIRF) and atomic force microscopy (AFM) setup (**Figure 3.2a**) as described in Chapter 2. The Cy5 was excited with a HeNe laser (632.8 nm, Thorlabs, Inc., New Jersey, USA) and both fluorescence microscopy and AFM measurements were performed in milliQ water.

3.2.3 Persistence length analysis

The persistence length defines the flexibility of a polymer and is the characteristic distance over which the tangent angles are correlated. For distances much smaller than the persistence length the correlation approaches unity, whereas for distances larger than the persistence length the angles randomize and the correlation is lost. Inextensible polymers that exhibit a resistance to bending are usually described with the worm-like chain model.[28] The key parameter of this model is the bending stiffness κ. Describing the position along the polymer chain (length L) with a coordinate $s \in (0, L)$, measured along the polymer backbone, $\vec{r}(s)$ is the position of a chain segment and $\hat{t}(s) = d\vec{r}/ds$ is a unit tangent vector denoting the local orientation.

The key physics of the bending resistance is captured in the model by introducing an energy penalty on gradients of $\hat{t}(s)$, given by

$$E_{\text{bend}} = \frac{\kappa}{2} \int ds \left| \frac{d\hat{t}}{ds} \right|^2, \tag{3.1}$$

so that higher bending moduli lead to straighter chains. The combined effect of thermal fluctuations and bending stiffness then leads to a typical length (measured along the backbone) over which the chain orientation decorrelates, the persistence length $L_p = \kappa/(k_B T)$. This length can be extracted from any form of data that describes the local orientation of the polymer chain as a function of contour length s, by fitting the tangent vector autocorrelation to its theoretical prediction:[29]

$$C(s) = \langle \hat{t}(s) \cdot \hat{t}(0) \rangle = \exp\left[-\frac{s}{2L_p}\right]. \tag{3.2}$$

Here the average is taken over an ensemble of similar chains. The factor 2 in this equation is only present for chains adsorbed onto a flat surface, i.e. 2D chains, as we study here. In adsorbed chains, the tangent vector can be represented with a single angle $\theta(s)$ indicating the angle between $\hat{t}(s)$ and a chosen reference axis in the plane of the surface, and the average can be rewritten as $C(s) = \langle \cos[\theta(s) - \theta(0)] \rangle$. We therefore refer to $C(s)$ as the *cosine correlation function*, given by:[29,30,31]

$$C(s) = \langle \cos[\theta(s_0 + s) - \theta(s_0)] \rangle_{s_0} = e^{-s/(2L_p)}, \tag{3.3}$$

where $\theta(s_0 + s)$ is the tangent angle at coordinate $(s_0 + s)$, $\theta(s_0)$ is the reference tangent angle and the average is taken over all reference points along the polymer.

To extract the persistence length from fluorescence images we used an approach based on the cosine correlation function, where the apparent persistence length was extracted from skeletonized polymers.[30] The backbone of each polymer was obtained by pre-processing the raw image of the polymers (**Figure 3.3a**) using the free image-processing software *ImageJ* based on a similar approach as Graham *et al.*[30] We use thresholding and skeletonization (**Figure 3.3d**), i.e. creating a one-pixel-wide backbone by eliminating the outer pixels of the polymer. However, due to pixilation of the camera-images the polymer backbone does not always follow the polymer, because the pixel size is large compared to the width of the polymer. This created curvature in the backbone that is not present in the polymer, therefore prior to thresholding images were interpolated with a factor 9, i.e. each pixel is divided into nine subpixels, where each subpixel is given a weighted intensity of its nearest neighbors (**Figure 3.3b**). To further improve localization of the polymer backbone the polymer was deconvolved with a 2D Gaussian with the FWHM of the experimental point spread function (**Figure 3.3c**). Before thresholding and skeletonization, the image was Gaussian-smoothed to improve thresholding. The Gaussian smoothing was necessary to smooth inhomogeneities in the intensity caused by deconvolution of a noisy image, the Gaussian kernel used was however much smaller than the 2D Gaussian used for deconvolution.

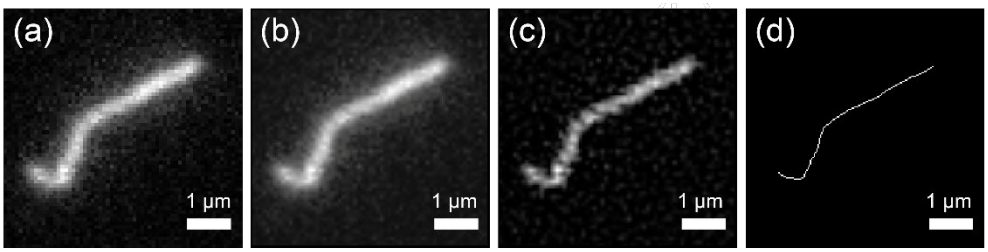

Figure 3.3 Pre-processing of the raw image to extract the polymer backbone. The raw image of a polymer **(a)** is pre-processed by enhancing contrast and interpolation **(b)** to improve the shape of the final one-pixel-wide backbone. The backbone is deconvolved with a 2D Gaussian to decrease its width **(c)** and is finally thresholded and skeletonized, resulting in a one-pixel-wide polymer backbone **(d)**.

The coordinates along the polymer were determined from the skeletonized backbone which was first smoothed using a third-order Beziér spline fit. From this fit the tangent angles at each coordinate along the polymer were calculated, a fit with Eq. (3.3) then yields the persistence length. When applied to a single immobilized polymer an apparent persistence length is obtained, as the polymer is in one of infinite configurations. Only when performing cosine correlation on many configurations of one polymer or many different molecules an accurate estimate of the persistence length is obtained. To prevent artefacts due to low sampling at large s we only fitted the cosine correlation function for s ranging from 0 to 1 µm.

To assess the necessity of this pre-processing procedure and the accuracy of the cosine correlation analysis we have performed simulations. Polymers with a persistence length of 1.5 µm (close to the measured value) were simulated using the worm-like chain model. We represented numerical worm-like chains as discrete jointed chains with straight segments of length Δs and angles between consecutive segments drawn from a normal distribution with variance $\Delta s/L_p$. The apparent persistence length for each polymer can then be calculated directly from the tangent angle at each coordinate along the polymer.

We analyzed 100 simulated polymers by fitting the cosine correlation function directly to the computer-generated tangent angles. For these polymers generated with a 1.5 µm persistence length we find a distribution of persistence lengths with a median ± MAD of 1.50 ± 0.31 µm (see **Figure 3.4a**). This implies that we find a significant spread even for simulated polymers with a predefined persistence length. This spread arises due to the finite length of each individual chain which introduces uncertainty in determining the persistence length. In order to compare simulations to experiments, polymers with the same pixelation and diffraction-limited resolution were generated by convolving the simulated polymers with a 2D Gaussian with a FWHM equal to the experimental point spread function yielding images with comparable signal-to-noise

(~10) and signal-to-background (~2.5) ratios to our experimental images. Persistence length analysis of convolved and pixelated polymers yielded the distribution of apparent persistence lengths shown in **Figure 3.4b**. The resulting persistence length is 1.64 ± 0.36 µm, showing an increase in persistence length and slight broadening of the distribution. This shift and broadening both increase when shot noise is added to the images to accurately mimic the experimental images (see **Figure 3.4c**). The distribution of apparent persistence lengths yields a persistence length of 1.80 ± 0.44 µm, which means convolution and pixelation with added shot noise results in a 0.3 µm increase in persistence length compared to the persistence length of the simulated polymers, where both the convolution and pixelation and the added noise contribute equally to the increase.

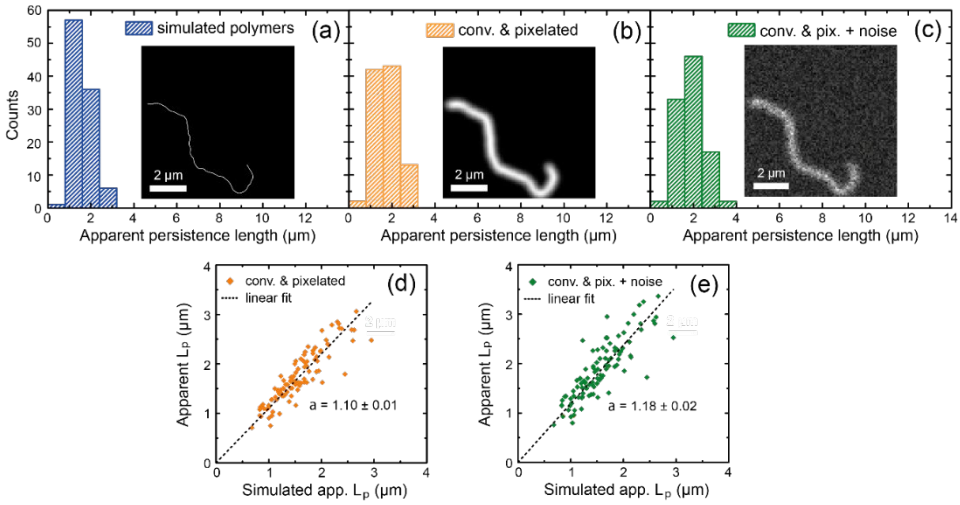

Figure 3.4 Apparent persistence lengths for simulated polymers. (a) Distribution of apparent persistence lengths of simulated polymers. The apparent persistence length is directly calculated from the generated angles at the coordinate along the polymer, yielding a persistence length of 1.50 ± 0.31 µm. Inset: simulated polymer with a contour length of 10 µm and a 1.5 µm persistence length. **(b)** Distribution of apparent persistence lengths of pixelated simulated polymers convolved with a 2D Gaussian yields a persistence length of 1.64 ± 0.36 µm. Inset: convolved and pixelated polymer. **(c)** Distribution of apparent persistence lengths of convolved and pixelated polymer with added shot noise yields a persistence length of 1.80 ± 0.44 µm. Inset: convolved and pixelated polymer with added shot noise. **(d)** Correlation of apparent persistence lengths of 100 simulated polymers with the convolved and pixelated version of the same polymer. A linear fit yields a slope a of 1.10 ± 0.01. **(e)** Correlation of apparent persistence lengths of 100 simulated polymers with the convolved and pixelated version with added shot noise of the same polymer. A linear fit yields a slope a of 1.18 ± 0.02.

In **Figure 3.4d** and **e** we show the correlation between the persistence length obtained directly from the tangent angles, and the persistence length of the convolved and pixelated polymers (**Figure 3.4d**) and the same polymers with shot noise (**Figure**

3.4e). Both show excellent correlation and linear fits with a slope of 1.10 ± 0.01 (**Figure 3.4d**) and 1.18 ± 0.02 (**Figure 3.4e**) again reveal the increase in apparent persistence length. In **Figure 3.4e** we observe a strong correlation ($R^2 = 0.97$), with a slope of 1.18 ± 0.02, and a random deviation from the expected persistence length due to the shot noise. From these results it can be concluded that pixelation, convolution and noise increase the median persistence length and slightly broaden the MAD of the distribution by ~40%. However, the spread observed in **Figure 3.4e** is largely due to the finite length of the chains as explained above.

3.3 Correlative imaging of supramolecular polymers

The fragile nature of the BTA polymers did not allow us to collect large numbers of AFM images that are needed for the statistical analysis of the persistence length. Interactions between the AFM tip and the polymer frequently led to damage and rupture of the polymer, even at the lowest forces that were accessible. For the majority of the AFM data, analysis of mechanical properties was therefore not possible. With our correlative approach, we establish an objective criterion to identify single and unentangled polymers directly from fluorescence images. We then used this criterion to determine the persistence length by collecting fluorescence images of many single polymers.

In **Figure 3.2b** we show a typical fluorescence image of a sample showing several isolated supramolecular polymers. Of these polymer-like structures, a subpopulation (~30 %) exhibits large variations in fluorescence intensity along the backbone. Such intensity variations were observed to occur in extended regions along the polymer backbone, but were also sometimes localized to an area smaller than the diffraction limit. To trace the origin of the variations in intensity along the backbone, we correlated TIRF measurements with atomic force microscopy (AFM) in liquid to resolve the underlying topography.

In **Figure 3.5** we show several examples of correlated AFM and fluorescence images of individual polymers. From a collection of AFM images we find that polymers exhibit heights ranging from 1.3 to 4.5 nm, whereas the width ranged from 11 to 27 nm. In **Figure 3.6a-c** AFM images of three BTA polymers are shown together with histograms of the height (**Figure 3.6d**, **f** and **h**) and width (**Figure 3.6e**, **g** and **i**) along the polymer obtained from the AFM images. The difference between height and width is caused by the dimensions of the tip. The height can be accurately determined from the z-position of tip, whereas the width is a convolution of the diameter of the tip and the width of the polymers. This results in larger values. The height determined from the AFM images is lower than the diameter of 6.2 nm obtained from SAXS measurements,[27] and

is most probably due to the compression of the side-chains by the force applied by the AFM probe or due to surface interactions that cause local differences in non-specific binding of the polymer to the glass surface. We find an average contour length of 7 ± 3 μm (n=83), in good agreement with previous studies.[11,24]

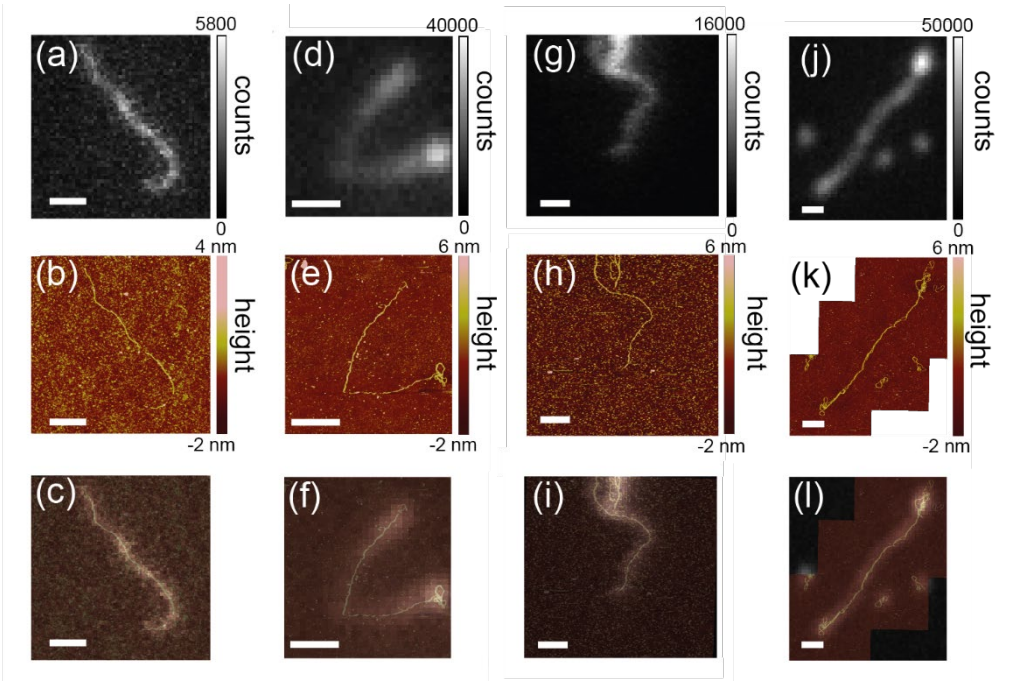

Figure 3.5 Correlated AFM and TIRF images of BTA polymers. TIRF **(a,d,g,j)**, AFM topography **(b,e,h,k)** and merged **(c,f,j,l)** images of four BTA polymers are shown. A homogenous intensity **(a)** corresponds to a single BTA polymer **(b,c)**, whereas intensity variations **(d,g,j)** correspond to entanglement or clustering **(e,h,k)**. All scale bars are 1 μm.

In **Figure 3.5a-c** we show a polymer that exhibits a uniform fluorescence intensity along its backbone. The AFM image reveals that this fluorescence signature corresponds to an individual and unentangled polymer. Approximately 60 % of the total analyzed polymers fall in this category. In **Figure 3.5d-f**, a brighter emission at the end of the polymer corresponds to an entangled chain, which were observed on ~30 % of analyzed polymers. We also observe other nonuniform fluorescence intensities, ~5 % of cases correspond to multiple polymers that are spaced by less than the diffraction limit, see **Figure 3.5g-i**, and intertwined polymers were observed in ~5 % of cases, see **Figure 3.5j-l**. Interestingly, in **Figure 3.5j** we find several diffraction limited spots that correspond to one or more short polymers that are strongly entangled, see **Figure 3.5k**. Because the resolution of both the AFM and fluorescence microscope are insufficient for a detailed analysis of such entangled polymers we focus in this study on the mechanical properties of single unentangled polymers.

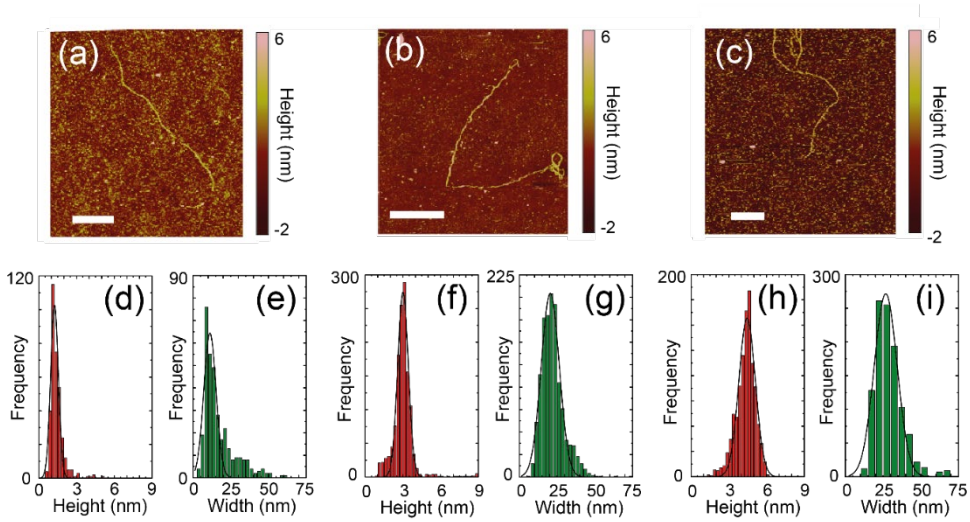

Figure 3.6 Height and width analysis from AFM images. Height (red) and width (green) distributions are shown for three polymers **(a-c)** and were determined from Gaussian fits to cross sections along the polymer length. This yields heights of 1.3 ± 0.3 nm (a), 3.0 ± 0.4 nm **(b)** and 4.5 ± 0.7 nm **(c)** and widths of 11 ± 4 nm **(a)**, 20 ± 6 nm **(b)** and 27 ± 8 nm **(c)**. Scale bars in **(a-c)** are 1 μm, error bars in **(d-e)** are standard deviations.

It is yet unclear what causes these water-soluble BTA polymers to cluster or entangle, specifically at the polymer ends. It is likely that hydrophobic interactions play a role, either between side-chains or between the exposed core and side-chains. A mechanistic understanding of the origin of the entanglement could be obtained by e.g. studying polymers with hydrophobic chains with different lengths. Also, molecular dynamics simulations may provide direct molecular insight into the underlying causes of the observed morphology.

To obtain an objective criterion that allows for the identification of single and unentangled polymers from fluorescence images, we analyzed the emission intensity along the backbone of 84 supramolecular polymers, three examples are shown in **Figure 3.7a-c**. The top row shows the intensity profile along the BTA polymer shown in **Figure 3.5a-c**, which is uniformly distributed as expected for an unentangled single polymer without interchain interactions that is homogeneously labelled. In **Figure 3.7e** and **f** the intensity profile is shown for BTA polymers that exhibit regions with elevated emission intensity (**Figure 3.7b**,**c**), giving rise to multimodal intensity distributions (**Figure 3.7h**,**i**). Typically the peaks in the multimodal distributions are separated by an integer times the mean of the lowest-intensity part (x3 for **Figure 3.7h**, x2 for **Figure 3.7i**), thus suggesting the presence of an integer number of chains within the diffraction limited focal spot. Although a polymer that is intertwined along its whole length (**Figure 3.5j-l**) cannot be identified by a nonuniform fluorescence intensity, we did not

find any cases in which entangled ends were also not observed. This suggests that identifying an intertwined polymer as a single unentangled polymer is unlikely.

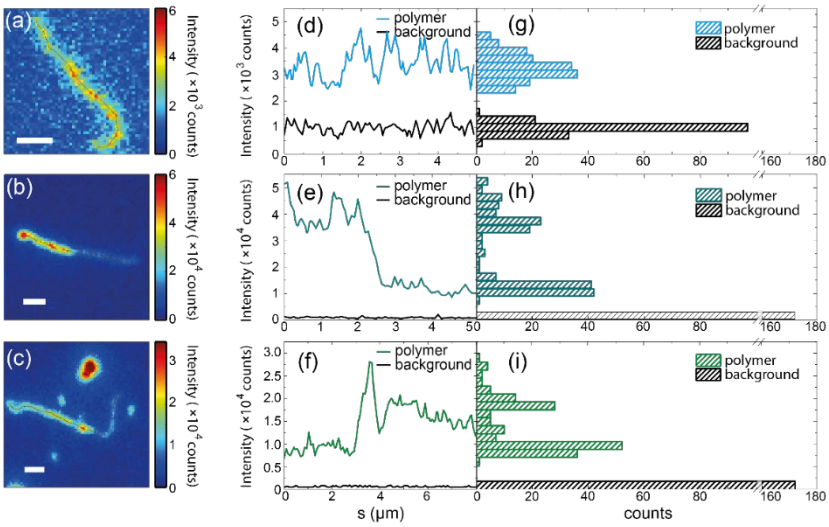

Figure 3.7 Intensity distribution along the polymer backbone. The black lines in **(a-c)** represent the trajectory along which the intensity is plotted in **(d-f)**. Scale bars are 1 μm. **(d-f)** Emission intensity along the backbone (blue, dark cyan and green lines) and background intensity (black lines). The background intensity was obtained by shifting the trajectory to a position next to the polymer. **(g-i)** Distributions of the polymer and background intensities. The difference in average intensity and background level arises due to differences in exposure time and gain of the EMCCD camera.

To quantify the uniformity of the fluorescence intensity we use the ratio of the background-corrected standard deviation of the intensity to its mean, i.e. the coefficient of variation (CV). In **Figure 3.8** we show the distribution of this ratio for 84 polymers in a bee swarm plot and a histogram. We observe a broad range of CVs, with a concentration of data points around CV = 0.25 corresponding to single unentangled polymers. For the persistence length analysis we therefore exclude polymers with a CV > 0.4, corresponding to the sum of the mean and 2σ of the Gaussian fit in Fig 8. For comparison, the polymers shown in **Figure 3.5** exhibit a CV of 0.27 (**Figure 3.5a**) and 0.54, 0.47 and 0.58 (**Figure 3.5d**, **g** and **j**, respectively). Verification of a subset of 10 polymers using AFM imaging resulted in 100% correct assignment using the above criterion. The uniformity of the fluorescence intensity along the backbone of the polymer therefore provides a reliable criterion to identify single unentangled polymers, which we will use hereafter to study the polymer's mechanical properties.

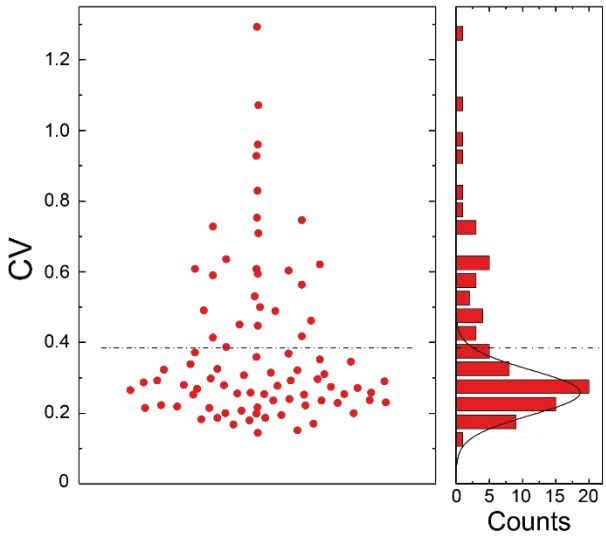

Figure 3.8 Distribution of coefficient of variation (CV) of the intensity along all polymer backbones. For a CV above the threshold (the mean plus 2σ of the plotted Gaussian fit), polymers are entangled or clustered and are excluded from persistence length analysis.

3.4 Persistence length analysis

For a polymer that obeys worm-like-chain dynamics the persistence length is the length over which angular correlations decrease to $1/\sqrt{e}$ (for a polymer constrained in two dimensions). In literature, the persistence length has been determined using the end-to-end distance,[32,33] cosine correlation analysis[31,34] or bending mode analysis.[31] The latter determines the angular bending modes of a polymer through Fourier analysis. End-to-end analysis extracts the persistence length by fitting the relation between a polymer's end-to-end distance and its contour length. However, kinks along the polymer may influence the end-to-end distance and can cause bias in the persistence length, especially for our polymers with lengths of only a few times the persistence length.

In contrast, cosine correlation analysis uses the sum of *local* values (the bend angles) because it employs the angle between segments that are significantly shorter than the contour length. This yields significant statistics even for a single polymer and greatly reduces the bias caused by kinks. To extract the apparent persistence length from the cosine correlation function, an exponential decay (**Equation 3.3**) was fitted to the correlation data. Note that in literature the bend angles for a certain segment length are often averaged over many polymers, followed by a fit with the cosine correlation

function. It is then implicitly assumed that each polymer has the same persistence length, allowing for averaging of the bend angles before fitting. It is known that supramolecular polymers contain structural diversity[27] which might cause polymer-to-polymer variations in their persistence length. We therefore refrain from this pre-averaging and instead analyze the single-polymer data directly. This gives a value for the apparent persistence length for each separate polymer, of which we then study the distribution.

In **Figure 3.9a** an example of the cosine correlation fit for one of the polymers (inset) is shown, yielding an apparent persistence length of 1.39 ± 0.01 μm. In **Figure 3.9b** we plot the distribution of persistence lengths, in which we observe a positively skewed distribution for single unentangled polymers (light blue bars) and a broader distribution for the entangled or clustered polymers (dark blue bars). We find a median persistence length of 2.2 ± 1.4 μm (median ± median absolute deviation, MAD) for single unentangled polymers, and a significantly larger value of 5.7 ± 3.5 μm for clusters. We speculate that clustering and entanglement may stiffen the polymer depending on the exact inter- and intramolecular interactions.[35] Selecting only single unentangled polymers thus greatly reduces the width of the distribution by removing sample heterogeneity caused by clustering and entanglement.

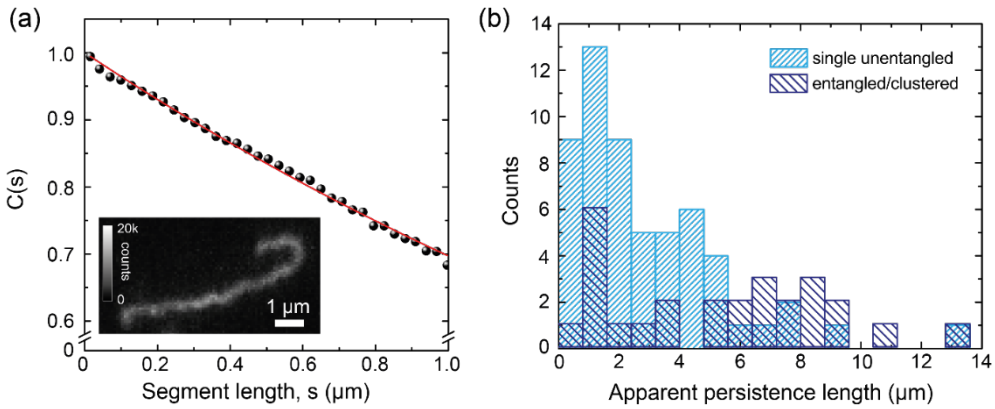

Figure 3.9 Distribution of the apparent persistence lengths. (a) For each polymer the apparent persistence length is determined using cosine correlation analysis, where the cosine correlation is fitted with an exponential decay according to **Equation 3.3.** The apparent persistence length of the polymer shown in the inset is 1.39 ± 0.01 μm. **(b)** Distribution of apparent persistence lengths of single unentangled (light blue) and entangled/clustered (dark blue) BTA polymers immobilized on glass.

Even after removal of the population of clustered and entangled polymers we still observe a relatively broad distribution of persistence lengths. As shown in section 3.2.3 the median persistence length found from our calculations is 1.80 ± 0.44 μm. Thus, the width of our measured distribution is a factor of ~3 broader than expected from our

simulations and exhibits a long tail toward longer persistence lengths. Below we discuss the possible origins of the broadening and tailing of the distribution.

First, polymer-to-polymer variations of the persistence length may inhomogeneously broaden the distribution. Recently, experiment[15] and theory[27] have hinted at the presence of structural diversity due to imperfect stacking of monomers. This structural diversity includes local bends and disorder in the structure of the polymer, which might result in stochastic variations of polymer diameter along the backbone. Starting from the definition of the persistence length $L_p = \kappa/k_BT$, where the bending stiffness κ is the product of the shape independent material stiffness E and the second moment of area I,[29,40] we find the relation between persistence length and polymer radius. For a cylinder with radius r the second moment of area is equal to $\frac{1}{4}\pi r^4$, which means $L_p \sim r^4$. Small changes in the radius would thus result in large changes in the persistence length.

Secondly, our analysis assumes that the polymers absorb onto the sample surface in a random conformation that is not influenced by the immobilization procedure and underlying sample topography. Although this has been shown to be true for specific samples,[36,37] we cannot exclude that local flow and inhomogeneities of the underlying substrate (e.g. local differences in charge density after piranha etching) affect the conformation of the absorbed polymer. To minimize these effects we excluded areas on the sample where neighboring polymers were clearly aligned. It is however possible that a fraction of polymers were less visibly affected by for example flow, resulting in a tail towards longer persistence lengths. Future studies on polymers that are not immobilized but freely diffuse in solution between two tightly spaced substrates might be used to quantify these effects.

3.5 Conclusions

In conclusion, we have shown the application of correlative microscopy to study the mechanical properties of supramolecular polymers. Atomic force microscopy revealed that a fraction of polymers were in a clustered or entangled state. The fragility of the supramolecular polymers did not allow us to reliably measure their persistence length using AFM. However, correlation with fluorescence microscopy allowed us to identify single and unentangled polymers purely based on the emission intensity along the backbone. Thus, this correlative technique facilitates the analysis of statistical properties of fragile supramolecular polymers.

For these single and unentangled polymers we found a persistence length of 2.2 ± 1.4 μm by cosine correlation analysis. Few fully atomistic calculations on

supramolecular polymers in water have been performed, except for peptide amphiphiles. Molecular dynamics simulations on cyclic peptide nanotubes[38] and β-sheet filaments[39] yielded persistence lengths of 0.46 μm and 1.2 – 4.8 μm, respectively, comparable to our measured value for BTA. The measured persistence length is comparable to that of cofilin-bound actin filaments[40] and to amyloid-like fibrils[41] and in between the persistence lengths of well-known biopolymers such as ssDNA (2 nm)[42] and dsDNA (50 nm)[43], and actin (10 μm)[40] and microtubules (5.2 mm).[31]

The distribution of apparent persistence length was narrowed drastically when entangled and clustered polymers, as identified from the correlated fluorescence images, were excluded. However, comparison of the distribution of apparent persistence lengths with simulations revealed that the measured distribution was still significantly broader than expected. We suggest that this broadening might be caused by a distribution of intrinsic persistence lengths, or by the immobilization of the polymers where local flow or surface inhomogeneities might play a role. Our analysis shows the advantages of studying single-polymer (apparent) persistence lengths, which not only allows for the comparison of the average values to simulations but also provides information on the shape and width of the distribution.

Here, the correlated measurements were applied to single polymers, showing the advantage of the ability to study single molecules rather than ensemble measurements. Applying this to different systems is advantageous when there are any inhomogeneous distributions of specific properties, multiple populations or other characteristics that remain hidden in ensemble measurements. Performing these single-molecule measurements with correlated microscopy techniques has the added advantage that when combining nanoscale structural information and optical localization or spectroscopy both optical properties and molecular or particle structure can be measured. This allows for correlation between the structure or conformation and the resulting optical properties. Here, we studied assemblies of organic molecules, but correlative microscopy also enables in-depth studies of assemblies of solid-state materials like nanoparticles, which is the topic of the next chapter.

References

1. Aida, T.; Meijer, E. W.; Stupp, S. I. Functional supramolecular polymers. *Science*, **2012**, *335*, 813–817.
2. Fletcher, D. A.; Mullings, R. D. Cell mechanics and the cytoskeleton. *Nature*, **2010**, *463*, 485-492.
3. Dong, R.; Zhou, Y.; Huang, X.; Zhu, X.; Lu, Y.; Shen, J. Functional supramolecular polymers for biomedical applications. *Adv. Mater.*, **2015**, *27*, 498-526.
4. Boekhoven, J.; Stupp, S. I. 25th anniversary article: supramolecular materials for regenerative medicine. *Adv. Mater.*, **2014**, *26*, 1642-1659.
5. Busserson, E.; Ruff, Y.; Moulin, E.; Guiseppone, N. Supramolecular self-assemblies as functional nanomaterials. *Nanoscale*, **2013**, *5*, 7098-7140.
6. Bakker, M. H.; Lee, C. C.; Meijer, E. W.; Dankers, P. Y. W.; Albertazzi, L. Multicomponent polymers as a modular platform for intracellular delivery. *ACS Nano*, **2016**, *10*, 1845-1852.
7. Dankers, P. Y. M.; Hermans, T. M. Baughman, T. W.; Kamikawa, Y. Kieltyka, R. E.; Bastings, M. M. C.; Janssen, H. M; Sommerdijk, N. A. J. M.; Larsen, A.; Van Luyn, M. J. A.; Bosman, A. W.; Popa, E. R.; Fytas, g.; Meijer, E. W.; Hierarchical formation of supramolecular transient networks in water: a modular injectable delivery system, *Adv. Mater.*, **2012**, *24*, 2703–2709.
8. Saunders, L.; Ma, P. X. Self-healing supramolecular hydrogels for tissue engineering applications. *Macromol. Biosci.*, **2019**, *19*, 1800313.
9. Yu, G.; Zhao, X.; Zhou, J.; Mao, Z.; Huang, X.; Wang, Z.; Hua, B.; Liu, Y.; Zhang, F.; He, Z.; Jacobson, O.; Gao, C.; Wang, W.; Yu, C.; Zhu, X.; Huang, F.; Chen, X. Supramolecular polymer-based nanomedicine: high therapeutic performance and negligible long-term immunotoxicity. *J. Am. Chem. Soc.*, **2018**, *140*, 8005-8019.
10. Wei, M-H.; B. Li, B.; Ameri David, R. L.; Jones, S. C.;Sarohia, V.; Schmitigal, J. A. and Kornfield, J. A. Megasupramolecules for safer, cleaner fuel by end association of long telechelic polymers. *Science*, **2015**, *350*, 72-75.
11. Leenders, C. M. A.; Albertazzi, L.; Mes, T.; Koenigs, M. M. E.; Palmans, A. R. A.; Meijer, E. W. Supramolecular polymerization in water harnessing both hydrophobic effects and hydrogen bond formation. *Chem. Commun.*, **2013**, *49*, 1963–1965.
12. Cantekin, S.; De Greef, T. F. A.; Palmans, A. R. A. Benzene-1,3,5-tricarboxamide: a versatile ordering moiety for supramolecular chemistry. *Chem. Soc. Rev.*, **2012**, *41*, 6125–6137.
13. Varela-Aramburu, S.; Morgese, G.; Su, L.; Schoenmakers, S. M. C.; Perrone, M.; Leanza, L.; Perego, C.; Pavan, G. M.; Palmans, A. R. A.; Meijer, E. W. Exploring the potential of benzene-1,3,5-tricarboxamide supramolecular polymers as biomaterials. *Biomacromolecules*, **2020**, *21*, 4105-4115.
14. Broaders, K. E.; Pastine, S. J.; Grandhe, S.; Fréchet, J. M. J. Acid-degradable solid-walled microcapsules for pH-responsive burst-release drug delivery, Chem. Commun., **2011**, *47*, 665–667.
15. Besenius, P.; Heynens, J. L. M.; Straathof, R.; Nieuwenhuizen, M. M. L.; Bomans, P. H. H.; Terreno, E.; Aime, S.; Strijkers, G. I.; Nikolay, K.; Meijer, E. W. Paramagnetic self-assembled nanoparticles as supramolecular MRI contrast agents, *Contrast Media Mol. Imaging*, **2012**, *7*, 356–361.
16. Shikata, T.; Ogata, D.; Hanabusa, K. Viscoelastic behaviour of supramolecular polymeric systems consisting of N,N′,N″-tris(3,7-dimethyloctyl)benzene-1,3,5-tricarboxamide and n-alkanes, J. Phys. Chem. B, **2004**, *108*, 508–514.
17. Bernet, A.; Alburquerque, R. Q.; Behr, M.; Hoffmann, S. T.; Schmidt, H-W.; Formation of a supramolecular chromophore: a spectroscopic and theoretical study, Soft Matter, 2012, 8, 66–69, *Chem. Commun.*, **2011**, *47*, 665–667.
18. Li, C.; Tan, J.; Guan, Z.; Zhang, Q. A three-armed polymer with tunable self-assembly and self-healing properties based on benzene-1,3,5-tricarboxamide and metal-ligid interactions. *Macromol. Rapid Commun.*, **2019**, *40*, 1800909.
19. Leenders, C. M. A.; Baker, M. B.; Pijpers, I. A. B.; Lafleur, R. P. M.; Albertazzi, L.; Palmans, A. R. A.; Meijer, E. W. Supramolecular polymerisation in water; elucidating the role of hydrophobic and hydrogen-bond interactions. *Soft Matter*, **2016**, *12*, 2887-2893.
20. Schenning, A. P. H. J.; Jonkheijm, P.; Peeters, E.; Meijer, E. W. Hierarchical order in supramolecular assemblies of hydrogen-bonded oligo(p-phenylene vinylene)s. *J. Am. Chem. Soc.*, **2001**, *123*, 409-416.
21. Palmans, A.R.A.; Meijer, E. W.; Amplification of chirality in dynamic supramolecular aggregates. *Angew. Chem. Int. Ed.*, **2007**, *46*, 9849-8969.

22. Korevaar, P. A.; George, S. J.; Markvoort, A. J.; Smulders, M. M. J.; Hilbers, P. A. J.; Schenning, A. P. H. J.; De Greef, T. F. A.; Meijer, E. W. Pathway complexity in supramolecular polymerization. *Nature*, **2012**, *481*, 492-497.
23. Li, Y.; Hammoud, A.; Bouteiller, L.; Raynal, M. Emergence of homochiral benzene-1,3,5-tricarboxamide helical assemblies and catalysts upon addition of an achiral monomer. *J. Am. Chem. Soc.*, **2020**, *142*, 5676-5688.
24. Albertazzi, L.; Martinez-Veracoechea, F. J.; Leenders, C. M. A.; Voets, I. K.; Frenkel, D.; Meijer, E. W. Spatiotemporal control and superselectivity in supramolecular polymers using multivalency. *Proc. Natl. Acad. Sci. USA*, **2013**, *110*, 12203-12208.
25. Besenius, P.; Portale, G.; Bomans, P. H. H.; Janssen, H. M.; Palmans, A.R.A.; Meijer, E. W. Controlling the growth and shape of chiral supramolecular polymers in water. *Proc. Natl. Acad. Sci. USA*, **2010**, *107*, 17888-17893.
26. Albertazzi, L.; van der Zwaag, D.; Leenders, C. M. A.; Fitzner, R.; Van der Hofstad, R. W.; Meijer, E. W. Probing exchange pathways in one-dimensional aggregates with super-resolution microscopy. *Science*, **2014**, *344*, 491-495.
27. Baker, M. B.; Albertazzi, L.; Voets, I. K.; Leenders, C. M. A.; Polmans, A. R. A.; Pavan, G. M.; Meijer, E. W. Consequences of chirality on the dynamics of a water-soluble supramolecular polymer. *Nat. Commun.*, **2015**, *6*, 6234.
28. Kratny, O.; Porod, G. Röntgenuntersuchung gelöster Fadenmoleküle. *Rec. Trav. Chim. Pays-Bas.*, **1949**, *68*, 1106-1123.
29. Broedersz, C. P.; MacKintosh, F. C. Modeling semiflexible polymer networks. *Rev. Mod. Phys.*, 2**014**, *86*, 995-1036.
30. Graham, J. S.; McCullough, B. R.; Kang, H.; Elam, W. A.; Cao, W.; De La Cruz, E. M. Multi-platform compatible software for analysis of polymer bending mechanics. *PLoS One*, **2013**, *9(4)*, e94766.
31. Gittes, F.; Mickey, B.; Nettleton, J.; Howard, J. Flexural rigidity of microtubules and actin filaments measured from thermal fluctuations in shape. *J. Cell Biol.*, **1993**, *120*, 923-934.
32. Howard, J. *Mechanics of motor proteins and the cytoskeleton.* Sunderland, MA, Sinauer Associates, Inc., 2001.
33. Landau, L. D.; Lifshitz, E. M. *Statistical physics 3rd edition, Part 1*, Butterworth-Heinemann, 1980
34. Isambert, H.; Venier, P.; Maggs, A. C.; Fattoum, A.; Kassab, R.; Pantaloni, D.; Carlier, M. F. Flexibility of actin filaments derived from thermal fluctuations. Effect of bound nucleotide, phalloidin and muscle regulatory proteins. *J. Biol. Chem.*, **1995**, *270*, 11437-11444.
35. Kouwer, P. H. J.; Koepf, M.; Le Sage, V. A. A.; Jaspers, M.; Van Buul, A. M.; Eksteen-Akeroyd, Z. A.; Woltinge, T.; Schwartz, E.; Kitto, H. J.; Hoogenboom, R.; Picken, S. J.; Nolte, R. J. M.; Mendes, E.; Rowan, A. E. Responsive biomimetic networks from polyisocyanopeptide hydrogels. *Nature*, **2013**, *493*, 651-655.
36. Abels, J. A.; Moreno-Herrero, F.; Van der Heijden, T.; Dekker, C.; Dekker, N. H. Single-molecule measurements of the persistence length of double-stranded RNA. *Biophys. J.*, **2005**, *88*, 2737-2744.
37. Rivetti, C.; Guthold, M.; Bustamante, C. Scanning force microscopy of DNA deposited onto mica: equilibrium versus kinetic trapping studied by statistical polymer chain analysis. *J. Mol. Biol.*, **1996**, *264*, 919-932.
38. Ruiz, L.; Von Achen, P.; Lazzara, T. D.; Xu, T.; Keten, S. Persistence length and stochastic fragmentation of supramolecular nanotubes under mechanical force. *Nanotechnology*, **2013**, *24*, 195103.
39. Park, J.; Kahng, B.; Kamm, R. D.; Hwang, W. Atomistic simulation approach to a continuum description of self-assembled β-sheet filaments. *Biophys. J.*, **2006**, *90*, 1510-2524.
40. McCullough, B. R.; Blanchoin, L.; Mariel, J-L.; De La Cruz, E. M. Cofilin increases the bending flexibility of actin filaments: implications for severing and cell mechanics. *J. Mol. Biol.*, **2008**, *381*, 550-558.
41. Bortolini, C.; Jones, N. C.; Hoffman, S. V.; Wang, C.; Besenbacher, F.; Dong, M. Mechanical properties of amyloid-like fibrils defined by secondary structures. *Nanoscale*, **2015**, *7*, 7745-7752.
42. Murphy, M. C.; Rasnik, I.; Cheng, W.; Lohman, T. M.; Ha, T. J. Probing single-stranded DNA conformational flexibility using fluorescence spectroscopy. *Biophys. J.*, **2004**, *86*, 2530-2537.
43. Hagerman, P. J. Flexibility of DNA. *Ann. Rev. Biophys. Biophys. Chem.*, **1988**, *17*, 265-86.

Chapter 4

Spatially resolved sensitivity of single-particle plasmon sensors

The high sensitivity of localized surface plasmon resonance sensors to the local refractive index allows for the detection of single-molecule binding events. Though binding events of single objects can be detected by their induced plasmon shift, the broad distribution of observed shifts remains poorly understood. Here, we perform a single-particle study wherein single nanospheres bind to a gold nanorod, and relate the observed plasmon shift to the binding location using correlative microscopy. To achieve this we combine atomic force microscopy to determine the binding location, and single-particle spectroscopy to determine the corresponding plasmon shift. As expected, we find a larger plasmon shift for nanospheres binding at the tip of a rod compared to its sides, in good agreement with numerical calculations. However, we also find a broad distribution of shifts even for spheres that were bound at a similar location to the nanorod. Our correlative approach allows us to disentangle effects of nanoparticle dimensions and binding location, and by comparison to numerical calculations we find that the biggest contributor to this observed spread is the dispersion in nanosphere diameter. These experiments provide insight into the spatial sensitivity and signal-heterogeneity of single-particle plasmon sensors and provides a framework for signal interpretation in sensing applications.

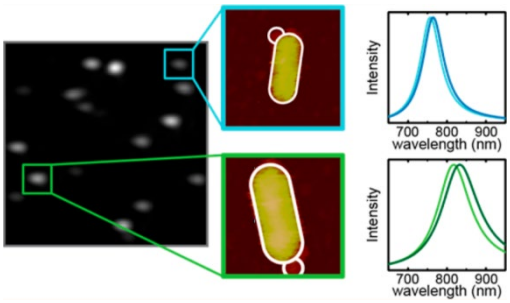

This chapter has been published as: Beuwer, M. A.; Van Hoof, B.; Zijlstra, P. Spatially resolved sensitivity of single-particle plasmon sensors. *J. Phys. Chem. C,* **2018**, *122*, 4615-4621.

In this chapter we study the spatially resolved sensitivity of self-assembled gold nanoparticle heterodimers towards local refractive index changes. To achieve this we employ correlative microscopy, where in comparison to previous chapters we have added the capability to perform spectroscopy on individual assemblies on an integrated device. We use this approach to perform a single-particle study wherein single nanospheres bind to a gold nanorod and relate the observed plasmon shift to the binding location using correlative microscopy. This correlative approach allows us to disentangle effects of nanoparticle dimensions and binding location, and by comparison to numerical calculations we find that the biggest contributor to this observed spread is the dispersion in nanosphere diameter. These experiments provide insight into the spatial sensitivity and signal-heterogeneity of single-particle plasmon sensors and provides a framework for signal interpretation in sensing applications.

4.1 Introduction

Gold nanoparticles are ideal tools for label-free sensing[1] as the frequency of their localized surface plasmon resonance depends on the material, shape, size, and the refractive index of the environment of the particle.[2,3] Label-free detection of molecular interaction kinetics has been successfully demonstrated using plasmonic nanoparticles,[4,5,6,7,8,9,10,11] but the magnitude of the plasmon shift is not easily translated to the number of analytes bound because the shift of the plasmon resonance depends on the location at which the analyte binds.[12,13] This resonance shift scales with the overlap integral between the analyte and the locally enhanced field, so the inhomogeneity in the locally enhanced field causes a distribution of plasmon shifts depending on the binding location. Moreover, the probability of analyte binding depends on particle geometry and is typically higher at protrusions due to better fluid accessibility, where the local field enhancement is also maximized.[13] It is therefore important to understand the dependence of the plasmon shift on binding location to correctly interpret sensor response and convert the signal to an analyte concentration.[12,13]

To measure both binding location and plasmon shift a correlative approach has been adopted in literature, where the plasmon shift is correlated to atomic force microscopy (AFM) or scanning electron images (SEM) of metallic nanoparticles. The plasmon response of gold colloids binding to a gold crescent-shaped nanoparticle was mapped by positioning the gold colloid near the nanocrescent tip, showing large shifts correspond to high local near-fields.[16] For triangular gold nanoplates it was shown that for anti-IgG the plasmon shift was more than twice as high when binding to the nanoplate edges compared to the flat terrace.[17] Correlated SEM and optical measurements on gold spheres bound to gold nanoplates were also combined with

numerical calculations to show how heterogeneity in the constructs influences the spectral response and revealed nanoparticle size to be the dominant variable.[18] Sannomiya *et al.* demonstrated excellent agreement between experiment and theory for single 20 nm DNA-labeled gold nanospheres binding to 100 nm spheres.[19] Finally, Garai *et al.* studied the polarization dependence of the two-photon photoluminescence to distinguish between gold nanospheres bound to the side and the tip of a nanorod,[20] whereas Szekrényes *et al.* were able to discern side-bound and top-bound nanospheres using polarization-resolved spectral measurements.[21]

Beyond nanoplates and nanospheres, gold nanorods have emerged as a promising geometry for plasmon sensing due to their high sensitivity to local refractive index[22] and reproducible bulk synthesis.[23] Particularly colloidal gold nanorods are attractive because their single-crystalline structure[23,24] minimizes plasmon dephasing by electron scattering, resulting in a narrow and bright longitudinal plasmon resonance.[25] Gold nanorods have been employed for detection of streptavidin[5,6,26], antibodies[7,8,27,28], fibronectin[9,26] and thrombin[26], where both ensemble-averaged[5,6,26,27,28] and single-molecule detection[7,9,8] have been demonstrated. For gold nanorods the location-dependent plasmon shift has been mapped on ensembles of polycrystalline particles using polymer masks covering either the particle's tip or center region[29] and for 20 nm SiO_2 dots embedded in a polymer film.[30] The highest plasmon shift was found for structures fabricated at the nanorod tip, in agreement with numerical calculations.[30] However, these were ensemble studies requiring averaging over hundreds of particles to mitigate variations due to differences in particle geometry.[29,30] Such ensemble-averaging masks particle-to-particle variations and heterogeneity, which are important contributors to the expected spread in plasmon shift.[31]

Here, we perform a single-particle study in which we elucidate the spatial sensitivity of single-crystal gold nanorods to the binding of a model analyte (small gold spheres). We use a correlative approach combining optical and atomic force microscopy and optical spectroscopy on an integrated device. Using this approach, we map the position-dependent plasmon shift of single gold nanorods in response to binding of small gold nanospheres. We find that the shift of the longitudinal surface plasmon increases when the gold nanosphere binds closer to the tip of the gold nanoparticle, in quantitative agreement with the numerical calculations. Because we probe single particles instead of ensembles we gain direct access to heterogeneity in the magnitude of the plasmon shift. We find that the spread in plasmon shift is not dominated by the volume or aspect ratio of the nanorods, but rather by the size dispersion of the gold spheres. These results imply that this correlated technique is well suited to study location-dependent sensor response to e.g. optimize site-specific functionalization protocols[14] and study location-dependent kinetics.[13]

4.2 Experimental and theoretical methods

4.2.1 Experimental setup

We used a combined AFM and total internal reflection scattering microscopy setup (**Figure 2.1b**). Single-particle spectroscopy measurements were performed on the same setup with the addition of a hyperspectral wheel (**Figure 2.9a**). To achieve this the excitation beam was focused on the periphery of the back-focal plane and was totally internally reflected at the glass-water interface. The scattered and reflected signals were collected by the 100x 1.49 NA oil immersion objective and imaged on an electron multiplying charged coupled (EMCCD) device (Andor iXon Ultra, Andor Technology Ltd, Northern Ireland). The directly reflected excitation beam was blocked in the detection path by a half-moon shaped beamblock, allowing only the photons scattered by the particles to reach the detector. Onto the Nikon Eclipse Ti microscope an AFM stage (Bruker Bioscope Catalyst in peak-force tapping mode) was mounted to enable topographic imaging. ScanAsyst-Air cantilevers were used with a stiffness k of 0.7 N/m and a force of 2 nN was applied. AFM imaging was performed in air after rinsing and drying the sample to reveal the binding location of the gold nanosphere. In **Figure 4.1a** a typical scattering image of immobilized gold nanorods is shown with the corresponding AFM image of the indicated 5 x 5 μm² area shown in **Figure 4.1c**. The insets show zooms of the particles where we observe two individual nanorods and a nanorod dimer.

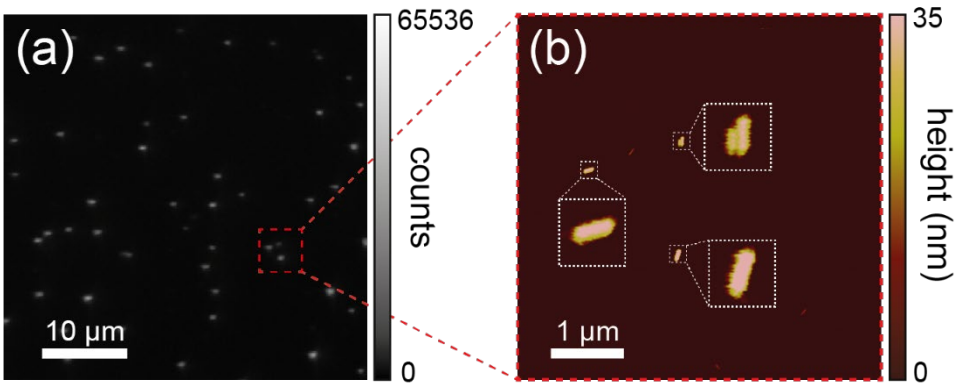

Figure 4.1 Correlated images. (a) Wide-field image of the scattered intensity of gold nanorods immobilized on the coverslip surface. **(b)** The indicated 5 × 5 μm² area in **(a)** was imaged with the AFM showing the diffraction-limited spots correspond to two single nanorods and a nanorod dimer.

Spectra of single gold nanorod assemblies were recorded with hyperspectral microscopy. Using white-light illumination with a broadband Tungsten-halogen light source (Thorlabs, New Jersey, USA). A series of bandpass filters (10 nm full width at half maximum and center wavelength ranging from 670 to 890 nm) was inserted into

the detection path and images were recorded with an EMCCD camera. For each wavelength channel the scattered intensity was determined by fitting the diffraction limited spots with a 2D Gaussian and correcting for the spectral profile of the light source. The plasmon resonance wavelength and linewidth were then determined by fitting a Lorentzian function to the scattering intensity as a function of photon energy for each nanoparticle.

Spectra were recorded for all particles, where particles with broad spectra, i.e. a linewidth deviating more than two standard deviations from the average, or with a non-Lorentzian-shape were discarded as clusters. The variation in scattering intensity we observe in the wide-field images is due to size dispersion[31] and particle orientation with respect to the partially polarized evanescent field. Gaussian fits to the distributions of LSPR wavelength and linewidth for all particles in a typical field of view give an average LSPR wavelength of 793 ± 38 nm and a linewidth of 157 ± 20 meV, corresponding excellently to the numerically calculated values for a 120 nm by 40 nm gold nanorod in water on a glass surface.

Real-time measurements of single 20 nm gold nanospheres binding to the immobilized gold nanorods were performed by illuminating with a fiber-coupled light emitting diode (Thorlabs, New Jersey, USA) with a center wavelength of 780 nm and a linewidth of 29 nm. A shift in the nanorod spectra due to a nanosphere binding event causes an intensity change, where each step in the signal corresponds to a single binding event. The step is positive or negative depending on the LSPR wavelength of the nanorod with respect to the probe excitation spectrum. These time-traces were used to identify particles that exhibited one or more binding events, while the magnitude of the plasmon shift was extracted from the scattering spectra before and after binding.

4.2.2 Sample preparation

Samples were prepared by spin coating 40x120 nm^2 gold nanorods (Nanoseedz, Hong Kong) at 2000 RPM for 2 minutes onto glass coverslips. Before spincoating the glass coverslips were sonicated in methanol and UV/ozone-cleaned for 90 min. After spin coating the samples were rinsed with methanol, PBS and water and blown dry under N_2-flow.

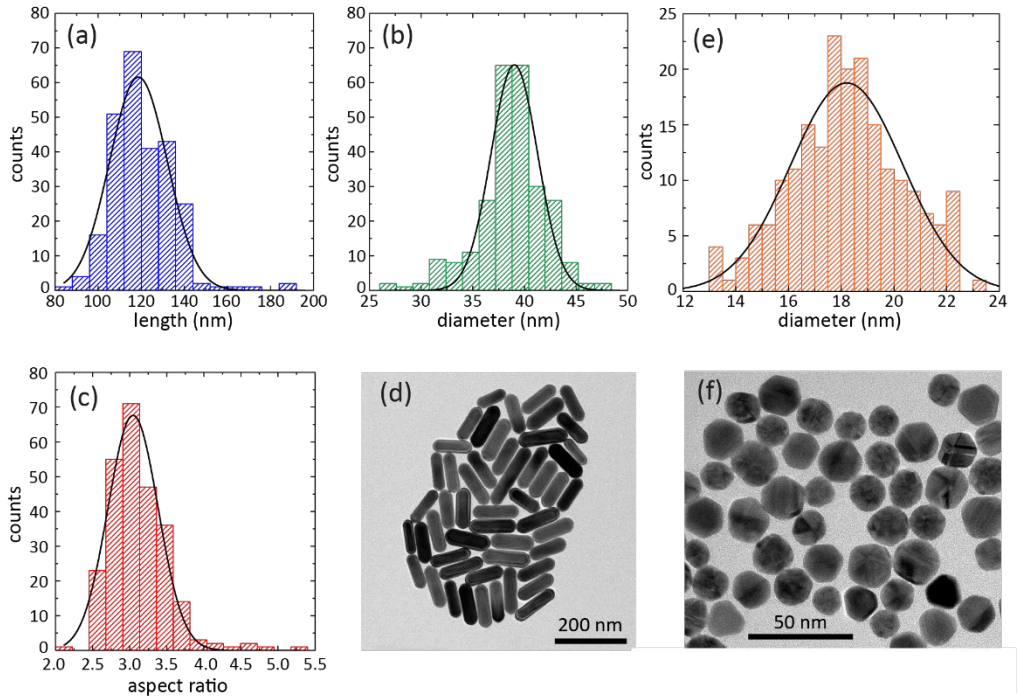

Figure 4.2 Size dispersion of nanorods and nanospheres. Distribution of **(a)** length, **(b)** diameter, and **(c)** aspect ratio from TEM images of gold nanorods **(d)**. A Gaussian fit to the distribution yields a length of 119 ± 13 nm, a diameter of 39 ± 2 nm and an aspect ratio of 3.0 ± 0.3. A Gaussian fit to the distribution of **(e)** diameter from TEM images of gold nanospheres **(f)** yields a diameter of 18.2 ± 2.1 nm.

We couple gold nanospheres to gold nanorods, of which the dimensions were measured using transmission electron microscopy (TEM). The distributions of gold nanorod length, diameter and aspect ratio, as well as the distribution of gold nanosphere diameter are shown in **Figure 4.2**. From Gaussian fits to the distributions we find a length of 119 ± 13 nm, a diameter of 39 ± 2 nm and an aspect ratio of 3.0 ± 0.3 for the gold nanorods and a diameter of 18.2 ± 2.1 nm for the gold nanospheres. To induce gold nanospheres binding to the gold nanorods we used cysteine-cysteine coupling.[20] Cysteine binds covalently to the particles via a gold-thiol interaction. Coupling of spheres to rods was achieved at a pH of 2.3 at which cysteine is zwitterionic and allows for nanosphere-nanorod coupling by electrostatic interactions.[20] The immobilized gold nanorods were first incubated in 100 μM L-cysteine (Sigma-Aldrich) in pH 2.3 MilliQ water. A solution containing 1.2 nM of 20 nm gold nanospheres (Sigma-Aldrich) was then flown in and incubated for 30 min while a time-trace was recorded. Afterwards the sample was flushed with MQ water adjusted to pH 2.3 to wash away unbound gold nanospheres and cysteine. Based on the dimensions of two bound cysteine molecules an interparticle spacing of ~1 nm is assumed.[20]

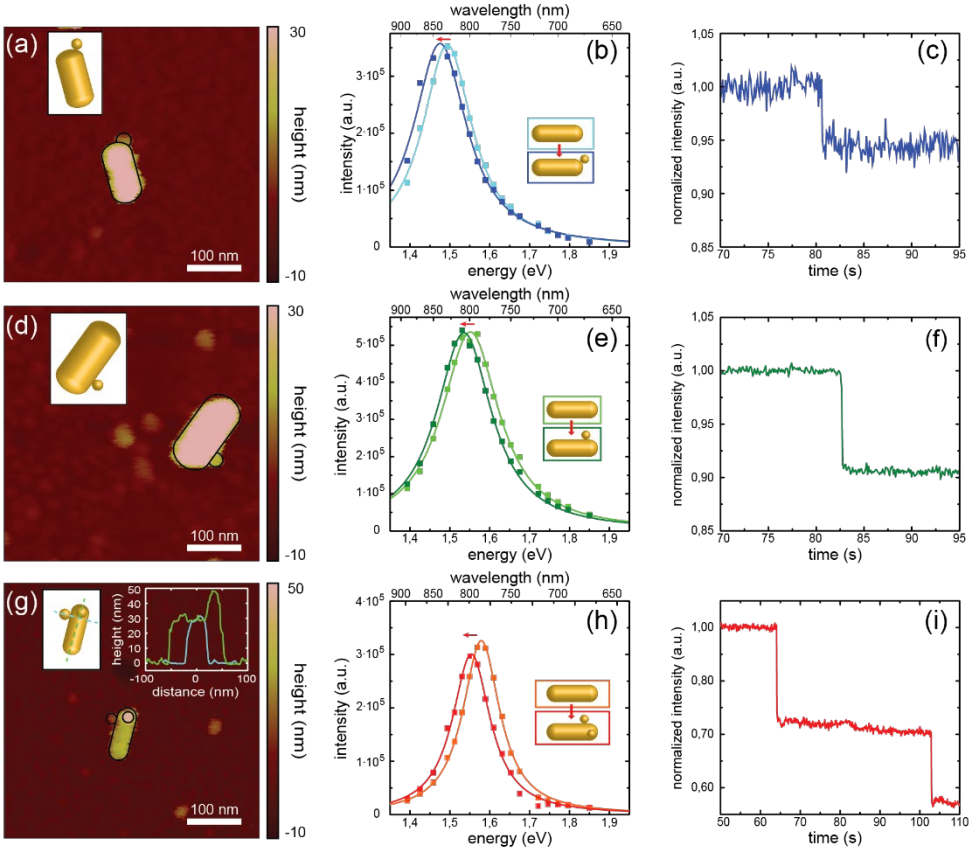

Figure 4.3 Correlated atomic force microscopy, spectroscopy and optical microscopy of gold nanoparticles binding to individual gold nanorods. From AFM images **(a, d, g)** the binding position is determined. Insets show the binding position of the nanospheres to the gold nanorods. In the inset in **(g)** cross sections along the longitudinal and transversal axis of the nanorod show the dimensions of the gold nanoparticles. The total plasmon shift is extracted from the scattering spectra before and after incubation in gold nanospheres **(b, e, h)**. Monitoring the scattering intensity in time at a single excitation wavelength results in stepwise changes in scattered intensity due to nanosphere binding **(c, f, i)**. For some particles we observe multiple binding events evidenced by multiple stepwise intensity changes **(i)**.

4.3 Correlative AFM and fluorescence imaging of supramolecular polymers

The results for three typical nanoparticles are shown in **Figure 4.3**. The AFM scans show different heterodimer configurations where the nanorods in **Figure 4.3a** and **d** have bound a single gold nanosphere, whereas in **Figure 4.3g** we observe two bound nanospheres. The corresponding plasmon shifts, as measured from the Lorentzian fit to the spectra, are 10.3 ± 0.5 nm (**Figure 4.3b**), 8.3 nm ± 0.3 nm (**Figure 4.3e**) and 12.7 ± 0.5 nm (**Figure 4.3h**). The time-traces recorded on the same particles confirm this

behavior as the number of observed step-wise changes in intensity matches the number of bound spheres. For approximately 15% of the particles stepwise changes were observed in the scattering intensity time-traces, indicating one or more gold nanosphere binding events.

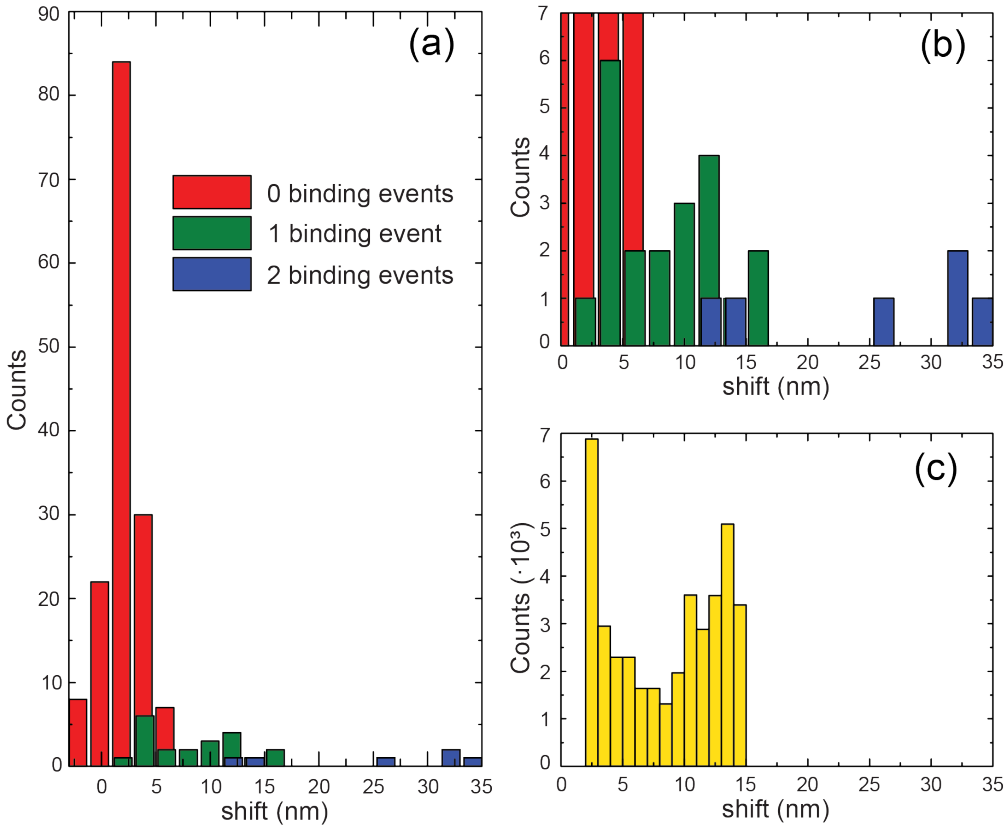

Figure 4.4 Measured and calculated distributions of plasmon shifts due to nanosphere binding. (a) distribution of plasmon shifts. The total number of binding events for each particle was determined by counting stepwise intensity changes in the time traces. A Gaussian fit to the distribution of plasmon shifts for zero binding events yields a shift of 2.1 ± 1.2 nm, caused cysteine molecules binding during incubation. **(b)** Zoomed-in plot of **(a)** highlighting the distributions for particles that exhibited one and two binding events. **(c)** Calculated distribution of plasmon shifts for 20 nm gold nanospheres binding to a 40x120 nm^2 gold nanorod with isotropic binding probability. Plotted on the same scale as the measured shifts in **(b)** for comparison.

In **Figure 4.4a** the distribution of measured plasmon shifts is shown for nanorods with zero, one and two nanoparticles bound. In **Figure 4.4b** the same plot is rescaled to show the distributions for one and two binding events per particle more clearly. For particles that show no binding events we find an average plasmon shift of 2.1 ± 1.3 nm, which we attribute to additional cysteine binding to the gold nanorods in the time that passes between the acquisition of both scattering spectra.

To gain more insight in the distribution of shifts we performed boundary element method (BEM) calculations.[33,34] The gold nanorod is modelled as a 120 nm long and 40 nm wide spherically capped cylinder, the dimensions as determined from TEM. The modelled nanosphere has a diameter of 20 nm and was placed at a distance of 1 nm from the gold nanorod corresponding to the length of a cysteine dimer.[20] Binding locations were spaced approximately 1 nm apart and the calculations were performed in water. We simulated the expected distribution of plasmon shifts by assuming an isotropic binding probability, i.e. the chance that a gold nanosphere binds at different random positions onto the nanorod is location-independent. We observe higher probability for shifts around 2 nm and larger than 10 nm. The peak at lower shifts is caused by nanospheres binding to the side of the nanorod which has a large available surface area, while nanospheres binding near the tip will result in a large plasmon shift causing the second peak. The shifts in between these lowest and highest values are due to nanospheres binding on the sides near the tip, which is only a small part of the total surface area explaining the lower amount of counts. Note that these calculations were performed without a glass surface, which may affect the distribution because it shields part of the surface area of the rod.

The measured distribution shown in **Figure 4.4b** is in good agreement with the results from BEM simulations shown in **Figure 4.4c**, where we also observe a broad range of shifts up to 15 nm. Both the measured and calculated distribution of shifts show a broad spread, in the next discussion we investigate the origin of this spread. In **Figure 4.5a** and **b** the electric field amplitude normalized to the incoming field is shown for two heterodimer configurations. The excitation of the longitudinal plasmon in combination with the lightning rod effect results in strong local fields at the nanorod tip compared to the nanorod side. The plasmon frequency shift $\Delta\omega$ depends on the overlap integral of the local field and the spherical particle given by[35]

$$\Delta\omega = -\omega \iiint_{V_P} \Delta\varepsilon\,(\boldsymbol{r},\omega)\boldsymbol{E}_{\mathrm{app}}(\boldsymbol{r}) \cdot \boldsymbol{E}(\boldsymbol{r}) d^3\boldsymbol{r}. \tag{4.1}$$

Here, the nanosphere, which has a volume V_p, perturbs the quasi-normal mode $\boldsymbol{E}(\boldsymbol{r})$ due to the change in local permittivity $\Delta\varepsilon(\boldsymbol{r},\omega)$. $\boldsymbol{E}_{\mathrm{app}}(\boldsymbol{r})$ is the modified quasi-normal mode taking into account the local field and is given by $\alpha\varepsilon_m\boldsymbol{E}(\boldsymbol{r})/[V_P\Delta\varepsilon(\boldsymbol{r},\omega)]$, with α the polarizability and ε_m the permittivity of the medium.[35] This results in a larger plasmon shift when a particle is positioned near the tip because of the high field-enhancement there. The electric field strength in the gap of the coupled nanosphere and nanorod is also increased at the tip (~270x enhancement) compared to the side (~30x enhancement). In **Figure 4.5c** the calculated plasmon shift is shown for 11 different binding locations at interparticle distances varying from 1 – 10 nm. Due to the rapidly decaying enhanced field the plasmon shift decreases strongly with distance.

This illustrates the importance of thin coatings and small capture molecules on nanoparticle sensors to optimize the shift induced by molecular binding.[36] The plasmon shift strongly decreases as the nanosphere is moved from the tip to the side of the nanorod because of the decreasing near-field intensity. Interesting to note is the influence of the presence of the substrate on the position-dependent plasmon shift. Position '9' and '11' are identical in the absence of the substrate due to rotational symmetry, but in the presence of the substrate we find a ~10% larger plasmon shift at position '11' due to the slightly enhanced field in the gap region between the tip of the particle and the glass substrate.

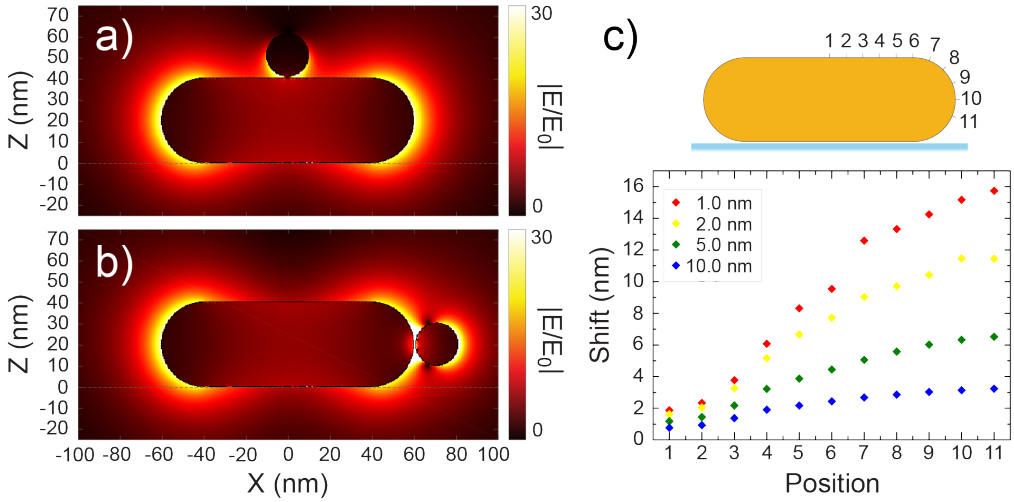

Figure 4.5 BEM simulations of local electric field enhancement and plasmon shift. Calculated normalized electric field |E/E0| around a gold heterodimer with a gold nanosphere at the side **(a)** and at the tip **(b)**. Fields are calculated for a polarization along the long axes and a wavelength resonant with the longitudinal plasmon resonance wavelength of the dimer. **(c)** Plasmon shift as a function of binding position for a 20 nm sphere near a 40 × 120 nm^2 gold nanorod on a glass substrate for interparticle distances from 1–10 nm

From the correlated microscopy shown in **Figure 4.3** we extract the binding location and plasmon shift, these are shown in **Figure 4.6b** (blue circles). The binding location *s* is represented as the coordinate along the gold nanorod surface, starting from the center of the side-facet as in **Figure 4.5**. When nanospheres are bound outside the XZ-plane the 3D-position was projected onto the XZ-plane. This is possible because of the radial symmetry of the nanorod if we neglect the presence of the substrate. In doing so we introduce an estimated uncertainty of ~10% in the expected plasmon shift (see **Figure 4.5c**). To aggregate and compare binding positions for particles with slightly different dimensions we rescale *s* to a 120 nm x 40 nm gold nanorod. This will introduce a small uncertainty in the position-determination, which we estimate to be less than 2 nm based on BEM simulations with different nanorod volume and aspect ratio, again much smaller than the observed heterogeneity. For side-bound nanospheres the error in shift is even less than 0.5 nm. From **Figure 4.5c** we expect that tip-bound

nanospheres result in plasmon shifts approximately 8x larger than side-bound nanospheres. In **Figure 4.6b** and **c** we see the same trend, where the plasmon shift increases for gold nanospheres binding closer to the nanorod tip as expected from the numerical simulations. Side-bound spheres induce a small but nonzero shift that is caused by the residual field-enhancement present at the side-facets of the rod, see **Figure 4.5c**. We notably observe a large spread in the measured plasmon shifts with variations of nearly a factor two even for spheres bound at a similar location on the nanorod, e.g. for particles bound around s = 40 nm.

We estimated the expected range of plasmon shifts due to dispersion in nanorod aspect ratio and volume, and in nanosphere diameter. This was done by calculating the plasmon resonances using the boundary element method (BEM), and varying the nanoparticle dimensions based on the observed distributions in the TEM images.

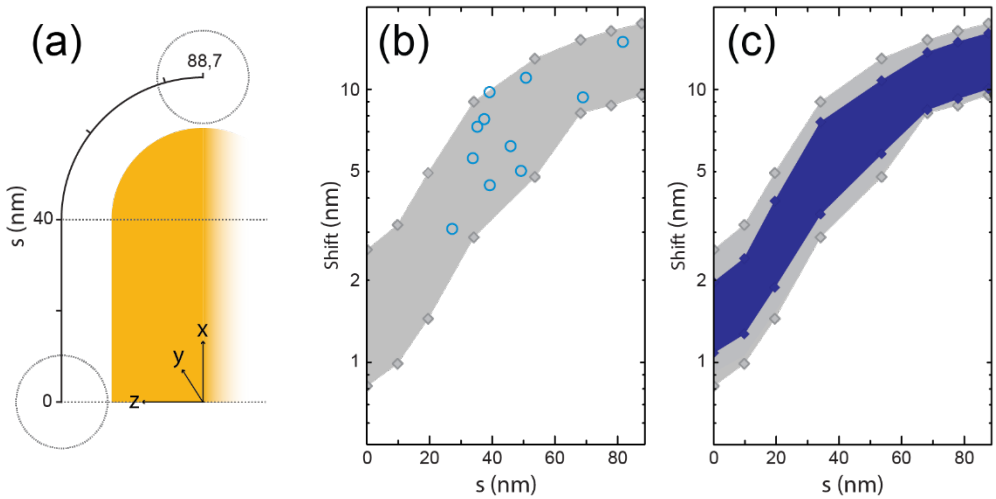

Figure 4.6 (a) Binding position along the nanorod s for a 40 nm wide and 120 nm long nanorod. The gray dashed circles in the cartoon show the binding position of the gold nanospheres at the side (s = 0 nm) and tip (s = 88.7 nm). **(b)** Measured plasmon shifts of single nanosphere binding events as a function of the coordinate s as measured by AFM (blue open circles). The light gray area indicates the range of shifts (standard deviation) based on the distribution of nanorod and nanosphere dimensions present in the samples, where the gray diamonds are the calculated values for different binding positions along the nanorod**. (c)** Calculated distribution of plasmon shift due to dispersion of nanosphere diameter (blue shaded area and blue diamonds) and the total distribution of shift due to the distribution of both nanorod and nanosphere dimensions. Deviations from a smooth curve are due to the finite mesh size used in the numerical calculations.

To estimate the expected spread in plasmon shifts, we calculate the plasmon shift for nanospheres at 10 positions along the gold nanorod by combining the smallest observed aspect ratio (2.7) and volume of the rod (V = 1.1 $\cdot 10^5$ nm^3) with the largest nanoparticle diameter (20 nm) resulting in the largest shifts. The lower boundary of plasmon shifts was established by combining the largest aspect ratio (3.4) and volume

(V = 1.5 $\cdot 10^5$ nm^3) of the rod with the smallest nanoparticle diameter (16 nm) resulting in the lower limit of the plasmon shifts. The resulting expected range in plasmon shifts is shown as the grey shaded region in **Figure 4.6b**.

We find that nearly all measurements fall within the calculated range of plasmon shifts. In **Figure 4.6c** we plot the contribution in the spread of plasmon shifts caused by only the dispersion in nanosphere diameter as the blue shaded area. These simulations reveal that the 10% size-dispersion in nanosphere diameter (18 ± 2 nm) dominates the observed spread in plasmon shift, whereas the distribution of nanorod volume and aspect ratio contribute significantly less to the distribution of shifts. Interestingly, the distribution of shifts for tip-bound spheres is nearly entirely determined by the distribution of sphere diameters, whereas for side-bound spheres the contribution of nanorod volume is increased. We attribute this effect to the volume-dependence of the near-field intensity around the rod.

In recent single-molecule plasmon sensing studies, we[8] and others[9] reported plasmon shifts induced by single proteins to vary widely from binding event to binding event. The origin of the observed spread in molecular sensing experiments remains poorly understood but is critical for the correct interpretation of sensor response. A correlated approach such as the one presented here may be used to directly image the binding position of bound proteins to gain insight into the origins of the spread in plasmon shifts, and provide guidelines on how to minimize this heterogeneity. Although globular proteins show very little size dispersion compared to the nanospheres used here, many proteins (e.g. antibodies[8] and fibronection[9]) are not globular and thus the plasmon shift will also depend on their orientation with respect to the nanorod.

Not only the plasmon shift is spatially dependent, numerical calculations have recently shown that the binding rate is also spatially heterogeneous. The binding rate at protrusions and tips is higher than near the coverslip surface due to fluid accessibility, and this heterogeneity becomes more pronounced for sharper tips and higher aspect ratios.[13] For the nanorods used in our experiments, the binding probability is predicted to be ~25% higher at the nanorod tip compared to the side.[13] This means that knowledge of the binding location is not only required to interpret the amplitude of a sensor signal, but also to determine the kinetic constants of the biomolecular interaction.

In practical sensing implementations it is not feasible to measure the binding location of each detected protein. In contrast, site-specific functionalization protocols may be advantageous to functionalize specific regions on the particle where the sensitivity to binding is maximized.[14,15] Qualitative measurements of their efficacy have

been performed,[14] but the quantitative effect on the heterogeneity in signal amplitude and kinetics is unknown. A correlated approach such as the one presented here may shed light on the origins of observed heterogeneity to allow for the tailored design and optimization of single-molecule sensors.

4.4 Conclusions

We have employed correlative microscopy to correlate the plasmon shift to binding position and demonstrated this for the first time on single gold nanorods. We have shown that the measured plasmon shifts fall within the expected range calculated from BEM simulations. The dominant contributor to the spread in plasmon shifts is the dispersion in size of the gold nanospheres, in combination with smaller contributions of dispersion in nanorod volume and aspect ratio. In the future correlated microscopy can be applied to evaluate efficacy of site-specific functionalization protocols, which will contribute to the improvement of single-molecule sensors. Specifically, the possibility of correlated microscopy to image the exact size and shape of both the nanoparticle and the detected analyte, in combination with the spectral properties and plasmon shift allows for the improved understanding of sensor signals.

Nanoparticle self-assemblies such as the ones studied in this chapter provide exciting opportunities to tune plasmon resonances and associated near-field enhancements due to plasmon hybridization. Varying the shape and size of the nanoparticles, as well as their conformation and interparticle distance provides tunability that cannot be achieved with their individual building blocks. The effect of tuning these conformations and their application in plasmonic sensing is discussed in the following chapter for self-assemblies of gold nanorods.

References

1. Taylor, A. B.; Zijlstra, P. Single-molecule plasmon sensing: current status and future prospects. *ACS Sens.*, **2017**, *2*, 1103-1122.
2. Zijlstra, P.; Orrit, M. Single metal nanoparticles: optical detection, spectroscopy and applications. *Rep. Prog. Phys.*, **2011**, *74*, 106401.
3. Guo, Y.; Zhu, X.; Li, N.; Yang, J.; Yang, Z.; Wang, J.; Yang, B Molecular sensitivities of substrate-supported gold nanocrystals. *J. Phys. Chem. C*, **2019**, 123, 7336-7346.
4. McFarland, A. D.; van Duyne, R. P. Single silver nanoparticles a real-time optical sensors with zeptomole sensitivity. *Nano Lett.* **2003**, *3*, 1057-1062.
5. Raschke, G.; Kowarik, S.; Franzl, T.; Sönnichsen, C.; Klar, T. A.; Feldmann, J. Biomolecular recognition based on single gold nanoparticle light scattering. *Nano Lett.* **2003**, *3*, 935-938.
6. Nusz, G. J. ; Marinakos, S. M.; Curry, A. C.; Dahlin, A.; Höök, F.; Wax, A.; Chilkoti, A. Label-free plasmonic detection of biomolecular binding by a single gold nanorod. *Anal. Chem.* **2008**, *80*, 984-989.
7. Zijlstra, P.; Paulo, P. M. R.; Orrit, M. Optical detection of single non-absorbing molecules using the surface plasmon resonance of a gold nanorod. *Nat. Nanotechnol.*, **2012**, *7(6)*, 379-381.
8. Beuwer, M.A.; Prins, M. W. J.; Zijlstra, P. Stochastic protein interactions monitored by hundreds of single-molecule plasmonic biosensors. *Nano Lett.*, **2015**, *15*, 3507-3511.
9. Ament, I.; Prasad, J.; Henkel, A.; Schmachtel, S.; Sönnichsen, C. Single unlabeled protein detection on individual plasmonic nanoparticles. *Nano Lett.*, **2012**, *12*, 1092-1095.
10. Spitzberg, J. D.; Zrehen, A.; Van Kooten, X. F.; Meller, A. Plasmonic-nanopore biosensors for superior single-molecule detection. *Adv. Mater.*, **2019**, *31*, 1900422.
11. Gooding, J. J.; Gaus, K. Single-molecule sensors: challenges and opportunities for quantitative analysis. *Angew. Chem., Int. Ed.*, **2016**, *55*, 11354-11366.
12. Claudio, V.; Dahlin, A. B.; Antosiewicz, T. J. Single-particle plasmon sensing of discrete molecular events: binding position versus signal variations for different sensor geometries. *J. Phys. Chem. C*, **2014**, *118*, 6980-6988.
13. Antosiewicz, T. J.; Käll, M. A multiscale approach to modeling plasmonic nanorod biosensors. *J. Phys. Chem. C*, **2016**, *120*, 20692-20701.
14. Zijlstra, P.; Paulo, P. M. R.; Yu, K.; Xu, Q-H.; Orrit, M. Chemical interface damping in single gold nanorods and its near elimination by tip-specific functionalization. *Angew. Chem., Int. Ed.*, **2012**, *51*, 8352-8355.
15. Paulo, P. M. R.; Zijlstra, P.; Orrit, M.; Garcia-Fernandez, E.; Pace, T. C. S.; Viana, A.S.; Costa, S. M. B. Tip-specific functionalization of gold nanorods for plasmonic biosensing: effect of linker chain length. *Langmuir*, **2017**, *33*, 6503-6510.
16. Unger, A.; Rietzler, U.; Berger, R.; Kreiter, M. Sensitivity of crescent-shaped metal nanoparticles to attachment of dielectric colloids. *Nano Lett.*, **2009**, *9*, 2311-2315.
17. Beeram, S. R.; Zamborini, F. P. Effect of protein binding coverage, location, and distance on the localized surface plasmon resonance response of purified Au nanoplates grown directly on surfaces. *J. Phys. Chem. C*, **2012**, *115*, 7364-7371.
18. Fang, A.; White, S. L.; Masitas, R. A.; Zamborini, F. P.; Jain, P. K. One-to-one correlation between structure and optical response in a heterogeneous distribution of plasmonic constructs. *J. Phys. Chem. C*, **2015**, *119*, 24086-24094.
19. Sannomiya, T.; Hafner, C.; Voros, J. In situ sensing of single binding events by localized surface plasmon resonance, *Nano Lett.*, **2008**, *8(10)*, 3450-3455.
20. Garai, M.; Zhang, T.; Gao, N.; Xu, Q-H. Single-particle studies on two-photon photoluminescence of gold nanorod-nanosphere heterodimers. *J. Phys. Chem. C*, **2016**, *120*, 11621-11630.
21. Szekrényes, D. P.; Pothorszky, S.; Zámbó, D.; Deák, A. Detecting spatial rearrangement of individual gold nanoparticle heterodimers. *Phys. Chem. Chem. Phys.*, **2019**, *21*, 10146.
22. Becker, J.; Trügler, A.; Jakab, A.; Hohenester, U.; Sönnichsen, C. The optimal aspect ratio of gold nanorods for plasmonic bio-sensing. *Plasmonics*, **2012**, *5*, 161-167.
23. Nikoobakht, B.; El-Sayed, M. A. Preparation and growth mechanism of gold nanorods (NRs) using seed-mediated growth method. *Chem. Mater.*, **2002**, *15*, 1957-1962.
24. Katz-Boon, H.; Rossouw, C. J.; Weyland, M.; Funston, A. M.; Mulvaney, P.; Etheridge, J. Three-dimensional morphology and crystallography of golf nanorods. *Nano Lett.* **2011**, *11*, 273-278.

25. Luis, M.; Guyot-Sionnest, P.; Lee, T-W.; Gray, S. K. Optical properties of rodlike and bipyramidal gold nanoparticles from three-dimensional computations. *Phys. Rev. B: Condens. Matter Mater. Phys.*, **2007**, *76(23)*, 235428.
26. Rosman, C.; Prasad, J.; Neiser, A.; Henkel, A.; Edgar, J.; Sönnichsen, C. Multiplexed plasmon sensor for rapid label-free analyte detection. *Nano Lett.* **2013**, *13*, 3243-3247.
27. Mayer, K. M. ; Lee, S.; Liao, H.; Rostro, B. C.; Fuentes, A.; Scully, P. T.; Nehl, C. L.; Hafner, J. H. A label-free immunoassay based upon localized surface plasmon resonance of gold nanorods. *ACS Nano*, **2008**, *2*, 687-692.
28. Lee, S.; Mayer, K. M.; Hafner, J. H. Improved localized surface plasmon resonance immunoassay with gold bipyramid substrates. *Anal. Chem.* **2009**, *81*, 4450-4455.
29. Piliarik, M.; Kvasnička, P.; Galler, N.; Krenn, J. R.; Homola, J. Local refractive index sensitivity of plasmonic nanoparticles. *Opt. Express*, **2011**, *19*, 9213-9220.
30. Leitgeb, V.; Trügler, A.; Köstler, S.; Krug, M. H.; Hohenester, U.; Hohenau, A.; Leitner, A; Krenn, J. R. Three dimensional sensitivity characterization of plasmonic nanorods for refractometric biosensors. *Nanoscale*, **2016**, *8*, 2974-2981.
31. Henkel, A.; Ye, W.; Khalavka, Y.; Neiser, A.; Lambertz, C.; Schmachtel, S.; Ahijado-Guzmán, R.; Sönnichsen, C. Narrowing the plasmonic sensitivity distribution by considering the individual size of gold nanorods. *J. Phys. Chem. C*, **2018**, *122*, 10133-10137.
32. Krug, M. K.; Schaffernak, G.; Belitsch, M.; Gašparić, M.; Leitgeb, V.; Trügler, A.; Hohenester, U.; Krenn, J.R.; Hohenau, A. Mapping the local particle plasmon sensitivity with a scanning probe. *Nanoscale*, **2016**, 8**,** 16449-16454.
33. Hohenester, U.; Trügler, A. MNPBEM – a Matlab toolbox for the simulation of plasmonic nanoparticles. *Comp. Phys. Commun.*, **2012**, *183*, 370-381.
34. Waxenegger, J.; Trügler, A.; Hohenester, U. Plasmonic simulations with the MNPBEM toolbox: consideration of substrates and layer structures. *Comp. Phys. Commun.*, **2015**, *193*, 138-150.
35. Yang, J.; Giessen, H.; Lalanne, P. Simple analytical expression for the peak-frequency shifts of plasmonic resonances for sensing. *Nano Lett.* **2015**, *15*, 3439-344.
36. Wang, Y.; Li, X.; Su, Z.; Wang, H.; Xia, H.; Chen, H.; Zhou, J. Single plasmonic particle with exposed sensing hot spot for exploring gas molecule adsorption in nanolocalized space. *Anal. Chem.*, **2019**, *91*, 4063-4069.
37. Sönnichsen, C.; Franzl, T.; Wilk, T.; von Plessen, G.; Feldmann. J Drastic reduction of plasmon damping in gold nanorods. *Phys. Rev. Lett.* **2002**, *88*, 077402.

Chapter 5

Self-assembled nanorod dimers for refractometric sensing

A publication based on this chapter is in preparation: Beuwer, M. A.; Van Hoof, B.; Zijlstra, P. Self-assembled nanorod dimers for refractometric sensing.

5.1 Introduction

The gold nanorod geometry has been proposed as an excellent single-particle sensor due to its high-yield synthesis combined with a narrow plasmon resonance that occurs away from the interband transitions of gold.[1,2] Single-nanorod plasmonic sensing has recently even reached single-molecule sensitivity.[3,4,5] The spatial dependence of the sensing response is crucial as explained in the **Chapter 4**, where we used correlative microscopy to show that the plasmon shift is maximized for analyte binding near the tip, where the enhanced near-field is maximal.[6,7] The plasmon shift induced by molecular binding depends on the overlap integral between the local electric field and the analyte molecule, providing design rules to improve sensitivity by e.g. incorporating protrusions or sharp corners to enhance the local field further.[8] The elongated shape of a nanorod will therefore result in stronger near-field than for nanospheres, whereas the sharp tip of bipyramids will results in even stronger field-enhancement.[9] However, the small tip radius of bipyramids (typically a few nanometers) makes them photothermally less stable due to the low coordination number of atoms near the sharp tips.[10]

This indicates the requirement to find alternative routes to achieve even stronger near-fields. An attractive alternative is to utilize plasmon hybridization, where plasmon modes of neighboring particles hybridize similarly to molecular orbitals.[11,12,13] Here, coupled plasmonic particles produce strongly enhanced near-fields in the gap region between particles.

The simplest geometry in which such hybridization has been studied is a nanosphere homodimer, for which the dipolar modes hybridize to form four plasmon orbitals (see **Figure 1.8c**). Two of the plasmon orbitals have dipole moments oriented parallel to the dimer long axis. Among them, the symmetric bonding mode has the lowest resonance frequency/energy owing to the weakened dipole in each particle, [14] which gives a net dipole moment and couples best to the external light, whereas the dipoles of the asymmetric antibonding mode cancel out yielding a dark plasmon. The other two plasmon orbitals have dipoles oriented perpendicular to the dimer's long axis with the symmetric antibonding mode and the asymmetric bonding mode having non-zero and zero dipole moments, respectively.[15] Only the modes with a net dipole moment interact with the incident light, the asymmetric modes are so-called dark plasmon modes.[16]

The field-enhancement in the gap between the particles is highest for opposing positive and negative charges in the gap region, i.e. for the symmetric bonding mode. The wavelength at which this mode occurs depends on particle size and gap spacing, but is typically found between 600 nm – 750 nm.[17,18,19,20] Associated field enhancements

are typically between 10 and 50,[21,22] approximately 2 to 10-fold higher[23] than for an isolated gold sphere. These strong field enhancements in the gap have sparked investigations into the use of sphere-dimers for refractive index sensing,[24] fluorescence enhancement,[20,25] and surface-enhanced Raman scattering.[26,27] Even higher enhancements are expected for nanorod dimers due to their red-shifted longitudinal plasmon resonance that occurs even further away from the interband transitions of gold.

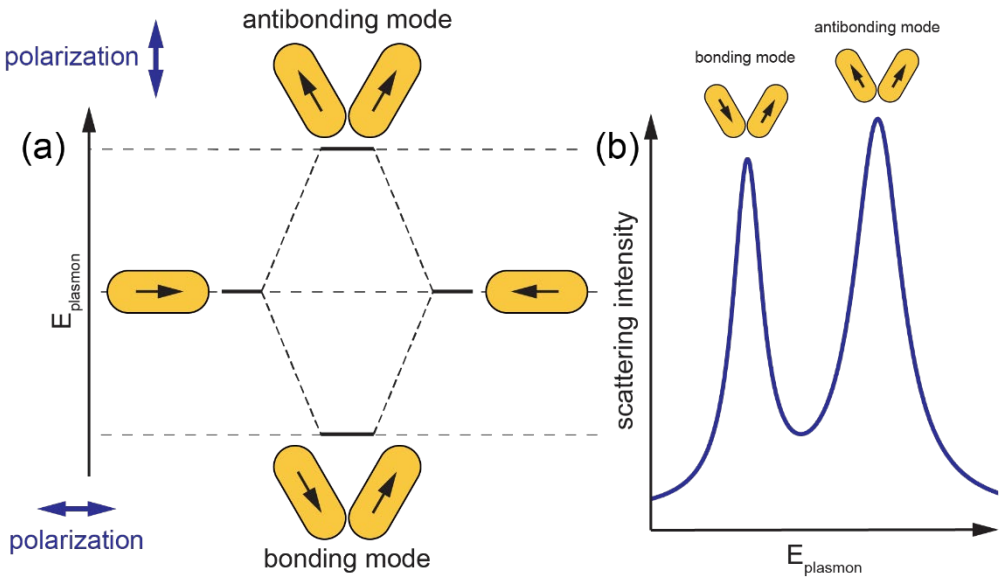

Figure 5.1 Hybridization of nanorod dimers. (a) Depending on the polarization of the excitation the nanorod dimer is in an antibonding or bonding mode. **(b)** The resulting scattering intensity due to the two different modes.

For nanorod dimers both the transverse and longitudinal modes couple to each-other, which can again be understood in the context of plasmon hybridization (**Figure 5.1a**). The far-field spectra are dominated by the hybridized longitudinal modes due to their stronger dipole-moment, so here we will focus only on those modes. The polarization averaged scattering spectrum (**Figure 5.1b**) exhibits two bright plasmon modes, a bonding mode at low energy and an antibonding mode at a higher energy.[28,29,30] The angle between the nanorods determines the relative intensity of the two peaks.[28,30,31] The dependence of the spectral response on interparticle spacing has also been well documented. Similarly to the redshift of the bonding mode in sphere dimers, the bonding mode of nanorod homodimers redshifts upon decreasing interparticle spacing.[28,35] Following this, nanoparticle dimers have been applied as plasmonic rulers[13,32,33] allowing for distance measurements ranging from 1-100 nm.[34]

In this chapter we employ correlative microscopy to investigate plasmon hybridization between the longitudinal plasmons of self-assembled nanorod dimers, and assess their performance as refractometric sensors. In agreement with numerical simulations we find that the observed scattering spectra exhibit a bonding and an antibonding mode, whose relative amplitude and wavelength depend on the size and relative angle of the two particles. We find that the refractive index sensitivity of the antibonding mode corresponds well with simulations, whereas the bonding mode systematically exhibits a lower than expected sensitivity. We interpret these results in the context of the overlap between the near-field of the mode and the medium, which is reduced for the bonding mode due to the presence of a thin 1 nm coating on the particles. These results have implications for the use of closely spaced plasmonic dimers in sensing assays and plasmon-enhanced emission, where the overlap between the near-field and the medium is crucial to obtain the signals predicted by simulations.

5.2 Methods

5.2.1 Experimental setup

Correlative measurements were performed using the setup as shown in in **Figure 2.9a**. Here, a white light source illuminated the sample via TIR illumination. The evanescent field excites the nanorod dimers on the glass surface, and the emission passes through the hyperspectral filters before being detected by the EMCCD. Using narrowband wavelength filters with different center wavelengths we obtain the scattering spectrum of individual dimers, which is fitted by a double Lorentzian function. The geometry of the same particles was obtained by subsequent atomic force microscopy (AFM) measurements, allowing us to directly correlate the measured optical response to the geometry of the same particle-dimer.

5.2.2 Sample preparation

Gold nanorod dimers were constructed using solution-phase self-assembly. To this end we employed cysteine coupling following a protocol based on the pH-dependent assembly and disassembly as reported by Sun *et al.*[36] A 0.1 nM suspension of 30x72 nm^2 nanorods (Nanopartz, Hong Kong; #A12-30-650) was concentrated 10 times by centrifugation. With a 10 mM CTAB solution in milliQ water, the CTAB concentration was adjusted to 7 mM. 10 μL of 10 mM cysteine solution in MilliQ water was added to 75 μL of the 1 nM nanorod suspension. With a 1M HCl solution and MilliQ water the volume was increased to 100 μL with a pH of 2 and a final 0.75 nM nanorod and 1 mM cysteine concentration.

The nanorod solution was incubated for 30 minutes at 45 degrees to allow for dimer formation. The cysteine binds covalently to the gold via its thiol, and for 1.96 < pH < 8.33 is in a zwitterionic state. This allows for electrostatic interactions between the positively charged NH_3^+ and the negatively charged O^- groups. This results in a stable dimer formation that can be reversed by increasing the pH to 11.3.[36]

Coverslips with dimensions of 21 x 26 mm^2 were cleaned by sonication in methanol for 20 minutes, and UV/ozone-cleaned for 90 minutes to form reactive hydroxyl groups on the surface. The surface is then silanized by incubation in 5% solution of (3-mercaptopropyl)trimethoxysilane (MPTMS) in ethanol for 5 min. A 15 µl drop of solution with nanorod dimers was then spincoated onto the MPTMS-coated coverslips.

Sensing experiments were performed in mixtures of water (n=1.33) and ethylene glycol (n=1.43) that enabled the tuning of medium refractive index by changing the mixing ratio. After each measurement the sample was flushed with MQ water and blow-dried under a N_2 flow before a different mixture was added. AFM measurements were performed in air using the peak-force tapping mode (**Chapter 2, section 2.3.3**).

5.2.3 Boundary element method calculations

We compared the measured optical response of individual dimers to numerical simulations using the boundary element method.[33,38] Here, two spherically capped cylinders were simulated with an angle *a* between their longitudinal axes. We estimate a 1.1 nm interparticle spacing, similar to the values reported before for this assembly method.[36] Care was taken that the meshing was fine enough to accurately simulate these small gap spacings. Calculations were performed without substrate with water as immersion medium using plane-wave excitation. The dimensions and relative orientation of the particles were extracted from the AFM images. Due to tip convolution the measured width and length of the particles are larger than the actual values. The difference between the more accurately measured height and the width of the rod was used to estimate the effect of tip-convolution and obtain the particle dimensions.

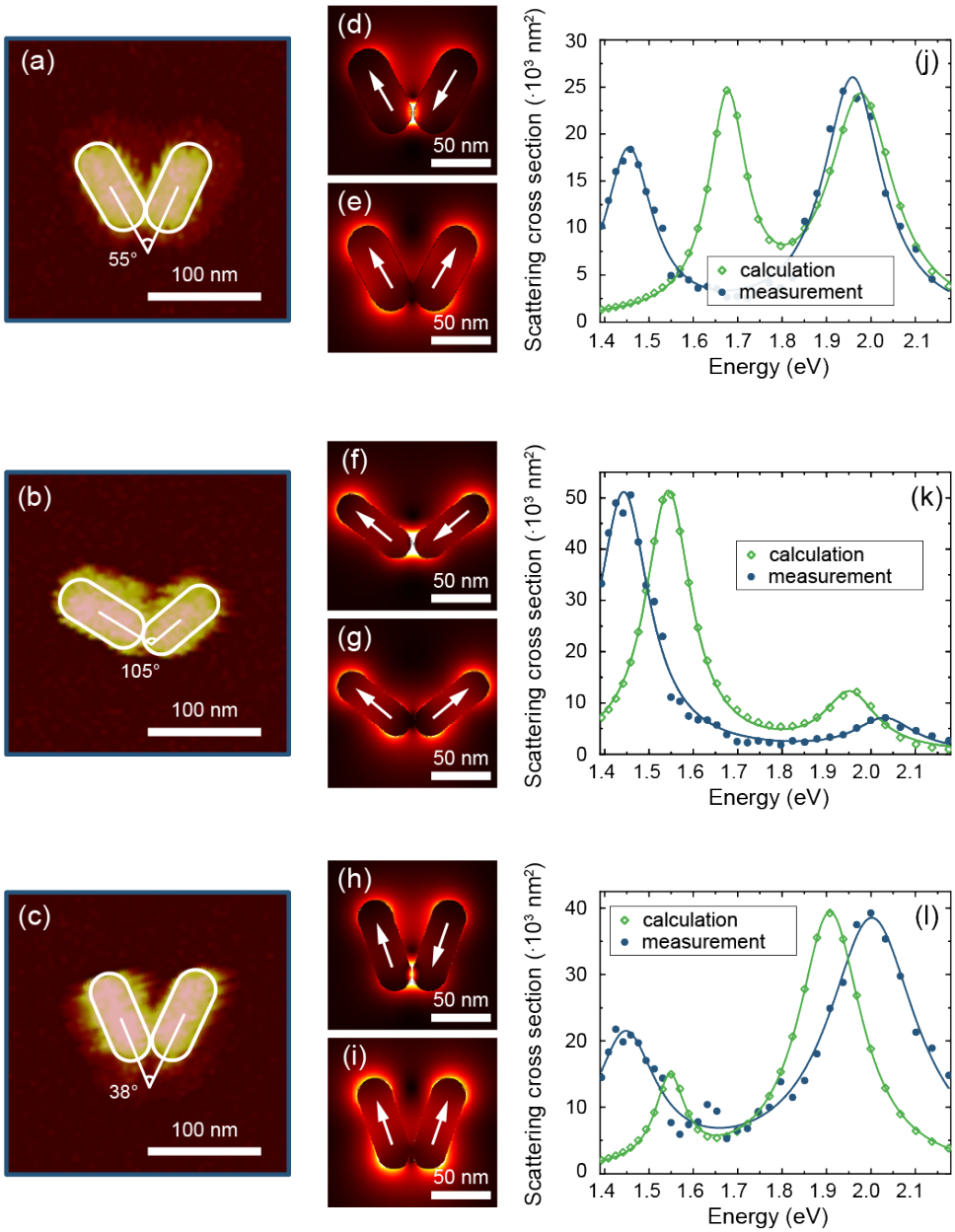

Figure 5.2 Correlated measurements of self-assembled gold nanorod dimers that are deposited on a glass substrate. Nanorod dimers were imaged with AFM **(a-c)** to determine their conformation and their corresponding spectra measured using confocal microscopy **(j-l**, blue circles**)**. Measured spectra were normalized to the peak value of the calculations. BEM calculations show the distribution of the near-field for x-polarized **(d,f,h)** and y-polarized **(e,g,i)** excitation on resonance with the bonding (top figures) and antibonding (bottom figures) modes. The corresponding spectra of each conformation were calculated for an uncoated dimer (open green diamonds) and fitted with a double Lorentzian function.

5.3 Correlated AFM and hyperspectral measurements of gold nanorod dimers

In **Figure 5.2a-c** the AFM images of three nanorod dimers are shown with their corresponding spectra in **Figure 5.2j-l** (blue circles). A double Lorentzian (solid blue line) was fitted through the hyperspectral data points. These spectra show the antibonding (higher energy) and bonding mode (lower energy) that arise due to hybridization of the longitudinal plasmons of the individual particles. The relative amplitude of these peaks and their energy depend on the nanorod conformation (nanorod angle, size, interparticle distance, medium and coating).

We also calculated the far-field scattering spectra for the geometry found in the AFM images, shown in **Figure 5.2j-l** next to the measured spectra. We find that the measured and calculated energy of the antibonding mode are in good agreement (**Figure 5.2j**) or that the measured spectra exhibit a slight blue-shift (**Figure 5.2k-l**), but that the measured bonding mode systematically exhibits a red-shifted resonance peak compared to calculations. We attribute the occasional discrepancy in the antibonding mode to the exact particle shape (e.g. tip-shape, which was assumed to be a half-sphere here but is known to vary from particle-to-particle) and their nanoscale positioning with respect to each other, particularly around the tip-region. Although finetuning of a combination of parameters (tip-curvature, gap spacing, particle dimensions) would likely retrieve the correct spectra, we refrained from this detailed optimization because the bonding mode is most interesting for refractometric sensing due to its suspected higher sensitivity.

To investigate the origin of the observed mismatch of the bonding mode energy we show in **Figure 5.2d-i** the near-field enhancement (E/E_0) for the bonding mode (**Figure 5.2d**,**f**,**h**) and antibonding mode (**Figure 5.2e**,**g**,**i**). The white arrows denote the orientation of the dipole moment in each nanorod. We find that for the bonding mode the field is greatly enhanced in the gap region, whereas for the antibonding mode the enhancement is highest at the nanorod tip region outside the gap. We therefore hypothesized that the discrepancy we find between the calculated and measured bonding mode energy may be partly due to the very thin cysteine coating that was used to induce oriented self-assembly. If this coating fills the gap between the particles this would particularly affect the bonding mode. Any remaining discrepancy between the measured and calculated bonding mode may then be explained again by differences in tip-curvature and exact particle positioning around the tip region.

The effect of a thin coating on the near-field enhancement and the scattering intensity are shown in **Figure 5.3**. For the uncoated dimer the field is shown to be maximal at the point where the two rods are closest. With the addition of the 0.5 nm

cysteine coating the field inside the coating is similarly distributed, but with a slightly lower amplitude than outside the coating. This is due to the higher refractive index of the coating (n = 1.47)[39] compared to the medium (n = 1.33).

This increased refractive index of the coating results in a redshift particularly for the bonding mode, as shown in **Figure 5.3** (dark green diamonds). We therefore attribute the red-shifted bonding mode we measured partly to the presence of the (very thin) cysteine coating on the particles. By iterative optimization we found that a combination of an 0.6 nm gap and 0.5 nm cysteine coating gives the best correspondence between measurements and simulations. These values are in good agreement with previous electron microscopy studies of gold nanorod dimers.[36] Correlative measurements across several nanorod dimers allows us to compare the plasmon wavelength of the bonding and antibonding mode to simulations. In the BEM calculations, the dimer angle of a cysteine-coated nanorod dimer (72 nm length, 30 nm diameter) was varied between 15 and 165 degrees. Subsequently, the bonding and antibonding plasmon wavelength and amplitude were extracted from a double Lorentzian fit to the calculated scattering intensity to find SPR wavelengths and peak ratios.

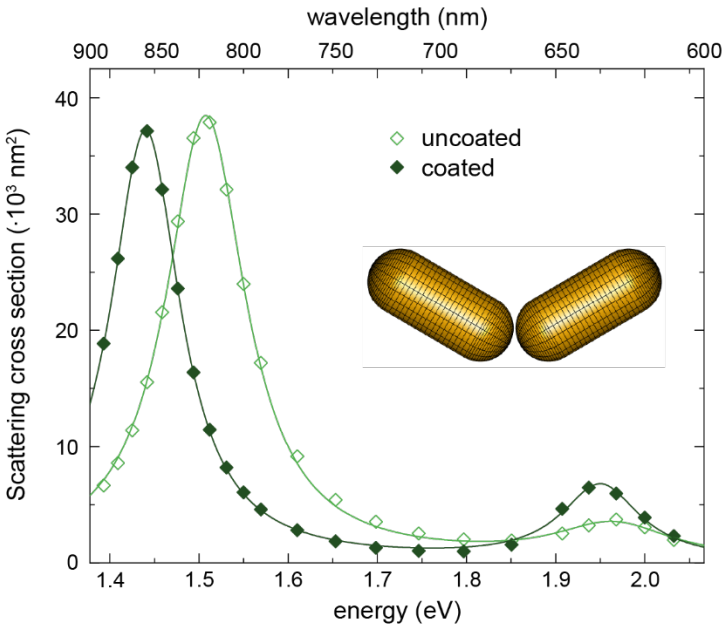

Figure 5.3 BEM calculations of gold nanorod dimer with and without a thin cysteine coating. A gold nanorod dimer with a 120 degree angle between the two particles was calculated using BEM. The spectra of the uncoated (light green, open diamonds) and coated (dark green, solid diamonds) dimer are shown for an interparticle distance 0.6 nm. In the inset the mesh used for the BEM calculations is depicted.

In **Figure 5.4a** the dependence of the plasmon wavelength on dimer angle is shown for the antibonding mode (green lines) and bonding mode (blue lines). Dashed lines represent a coated dimer, solid lines an uncoated dimer. The blue (bonding mode) and green (antibonding mode) data points show the experimentally determined plasmon wavelengths. Here, the error bars denote the fitting uncertainty. For the antibonding mode the measured resonance wavelengths match well with the calculated values. The calculations show that the antibonding mode plasmon wavelength is nearly insensitive to the dimer angle. Residual deviations in the measured resonance wavelength are due to variations in nanodimer geometry that cannot be prevented in the experiment, i.e. nanorod dimensions, interparticle distance and cysteine coating thickness.

For an interparticle distance of 0.6 nm with and without cysteine coating the calculated SPR wavelength corresponds well to the measured red-shift. A further decrease in interparticle distance would result in even better agreement, however overlap of 0.5 nm coating with the gold dimers in the calculations resulted in artefacts.

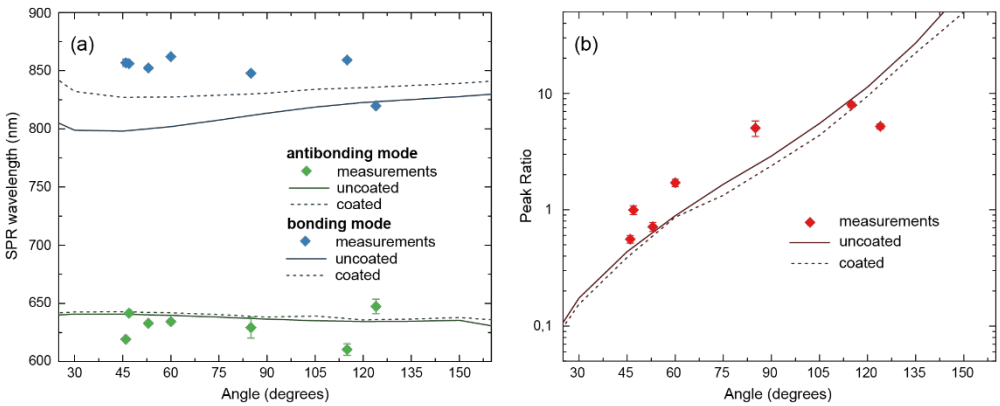

Figure 5.4 (a) Plasmon wavelength of the bonding and antibonding mode in water for nanorod dimers. The solid lines show the calculated peak wavelength of the bonding (blue) and antibonding (green) mode as a function of angle between the two uncoated nanorods in a dimer with a 0.6 nm interparticle distance. The solid lines represent uncoated dimers, dashed lines coated dimers. The diamonds represent measurements of the peak wavelength of the bonding (blue) and antibonding (green) mode. For the antibonding mode the SPR wavelength is more or less constant for all dimer angles, whereas it slightly increases for the bonding mode. **(b)** Peak ratio versus dimer angle in water from simulations for uncoated (solid line) and coated (dashed line) dimers and measurements (diamonds) in water. The peak ratio, the ratio of the area underneath bonding mode and the antibonding mode peak, increases for increasing dimer angle.

In **Figure 5.4b** the calculated peak ratio (red lines) and measured peak ratio (red diamonds) are shown. Peak ratio barely changes for coated dimers (red dashed line) or a decreased interparticle distance (not shown). Here, the peak ratio is defined as the ratio of the scattered intensities (area under the peak) of the bonding mode to the antibonding mode. From the calculations an increase in peak ratio is shown for increasing dimer angle. This increase is more than two orders of magnitude over the

range of angles, whereas the bonding mode plasmon wavelength only increases marginally over the same range. As reported before[31,40] this trend is well reproduced in the experimental data, the peak ratio increases for increasing angle. Deviations of the measured peak ratios from the theoretical value are likely caused by variations in dimer geometry.

5.4 Refractive index sensing

Dimers consisting of two spherical particles have been used for sensing, showing its promise by a strongly enhanced refractive index sensitivity compared to monomers.[41,42] Here, we focus on nanorod dimers due to their higher sensitivity compared to nanospheres and investigate their performance as ultrasensitive refractometric sensors. Potential scanning has recently been used to show that the enhanced near-field associated with the bonding mode has promise for refractometric sensing.[43] These experiments were however limited to dimers with an internal angle of 0 or 180 degrees, here we investigate end-linked dimers across all internal angles of orientation.

To assess the refractometric sensing performance of individual nanorod dimers we recorded spectra of dimers in three different media: water (n = 1.33), a 1:1 mixture of water and ethylene glycol (n = 1.38) and ethylene glycol (n = 1.43). The recorded spectra of three dimers (**Figure 5.5d-f**) are shown in **Figure 5.5a-c**. A double Lorentzian was fit through the hyperspectral microscopy data points.

For the first two dimers the dimer angle is smaller than 60 degrees (53 ± 2 and 47 ± 2 degrees, respectively) resulting in a lower intensity bonding mode compared to the antibonding mode in all three media. Furthermore, the relative scattered intensity of the bonding mode decreases for increasing refractive index. For the third dimer (**Figure 5.5f**) with a dimer angle of 124 ± 2 degrees, we observe the opposite in which the antibonding mode is weaker than the bonding mode, and increases in intensity with increasing refractive index. These features are all in good agreement with the numerical simulations.

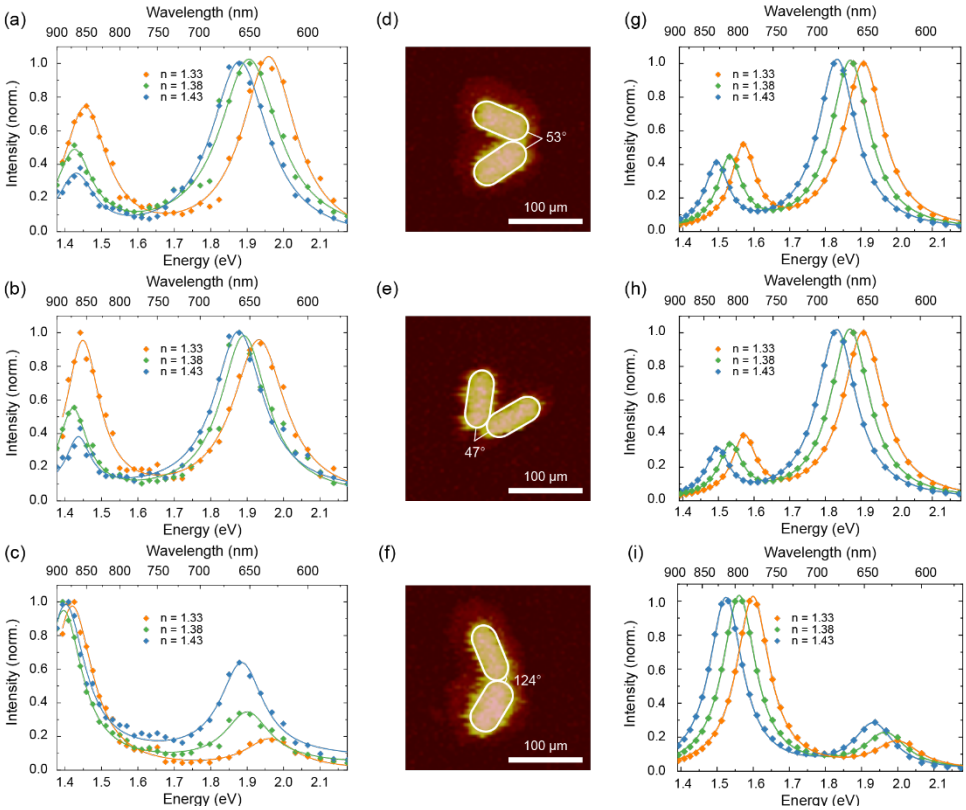

Figure 5.5 sensing with gold nanorod dimers. Left column: spectra of three gold nanorod dimers **(a-c)** measured in MQ water (orange), a 1:1 mixture of MQ water and ethylene glycol (green) and ethylene glycol (blue). Center column: corresponding AFM images of dimers **(d-f)**. Right column: BEM calculations of scattering spectra from nanorod dimers (length: 72 nm, diameter: 30 nm) **(g-i)** with an 0.5 nm cysteine coating and angle corresponding to the AFM images of the measured nanorod dimers.

To assess the sensing performance of these dimers we quantify their sensitivity, defined on an energy scale as $S_E = dE_{eV}/dn$, where dE_{eV} is the shift in plasmon energy upon a change in refractive index dn. To enable comparison between the different modes that occur at different energies we use the Figure of Merit (FoM) as a dimensionless measure for sensitivity. The FoM is generally defined as the ratio of the sensitivity S_E and the linewidth or full width at half maximum Γ, given by:[1]

$$\text{FoM} = \frac{S_E}{\Gamma} = \frac{1}{\Gamma}\frac{dE_{eV}}{dn}. \tag{5.1}$$

The measurements of nanorod dimer spectra in different media yield the FoM of the antibonding (green squares in **Figure 5.6**) and bonding (blue diamonds) mode by a linear fit of the correlation between refractive index and plasmon wavelength. The average antibonding mode FoM we find is 3.5 ± 0.7 RIU^{-1}, very comparable to the FoM

of single nanorods with the same plasmon wavelength, see **Figure 5.6**. Calculations of the FoM for a coated nanorod dimer provide similar results. For a coated dimer, numerical calculations indicate a FoM of 5.1 ± 0.4 RIU^{-1} for the antibonding mode. This is slightly higher than the measurements, which we attribute to the presence of the substrate that shields part of the sensing volume but is not included in the calculations.

In contrast, the average measured FoM for the bonding mode of 2.3 ± 0.7 is significantly lower than expected from calculations that indicate a FoM of 6.1 ± 0.7 RIU^{-1} for a coated dimer. This is significantly lower than a FoM of 8.1 ± 0.5 RIU^{-1} for an uncoated dimer, strongly suggesting that accessibility of the gap region plays a crucial role, since refractive-index sensitivity is dictated by the spatial overlap between the mode volume and medium. The substantially lower than expected FoM for the bonding mode indicates that the strongly enhanced and confined field in the gap region exhibits substantially lower accessibility than anticipated. For the antibonding mode, the enhanced field is mainly located near the nanorod tip regions away from the gap region (**Figure 5.2e**,**g**,**i**). Here, the 0.5 nm cysteine coating will lower the FoM compared to uncoated dimers, but still exhibits a strong response to refractive index close to the expected sensitivity from calculations. For the bonding mode the enhanced near-field is mostly concentrated in the gap region between the two nanorods (**Figure 5.2d**,**f**,**h**). We thus conclude that the cysteine coating nearly completely fills the gap region reducing the accessibility by the medium well below the expectation from simulations. Interestingly, we observe that the most red-shifted bonding modes exhibit the lowest FoM. This may indicate that for these dimers either the gap-spacing is smaller, or a larger fraction of the enhanced field in the gap region is occupied by cysteine. Both factors induce a red-shift of the bonding mode accompanied by a reduced refractive index sensitivity due to a reduced accessibility of the gap.

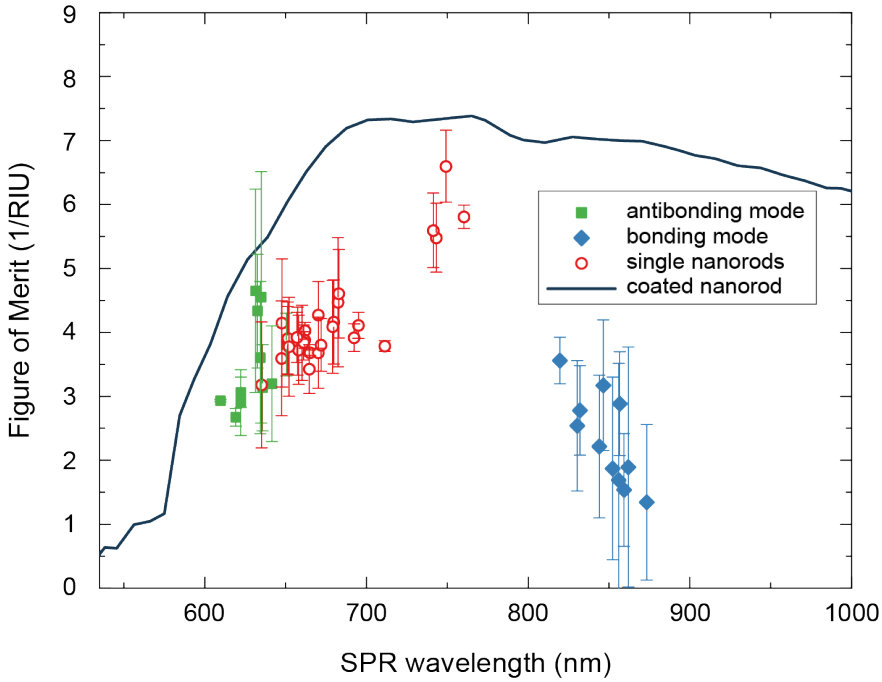

Figure 5.6 Figure of Merit (FoM) as a function of plasmon resonance wavelength for nanorod dimers (bonding mode, blue diamonds; antibonding mode, green diamonds) and single nanorods (open red circles). BEM calculations of the FoM of single nanorods were performed for increasing aspect ratio. The calculated FoM as a function of the LSPR wavelength is shown as a solid line for rods with a 0.5 nm cysteine coating (dark blue line). The measurements of the antibonding mode FoM and the single nanorod FoM are close to the calculated value, whereas the bonding mode FoM is lower.

5.5 Conclusions

These correlative experiments indicate that, despite the strongly confined electric field present in the gap of self-assembled dimers, the accessibility of the gap region is critical in their application. Often self-assembly is induced by molecular linkers like cysteine,[36] DNA,[17,44,45] thiol linkers,[46] or polyethylene glycol[47] that easily restrict access to the gap region. In the case of metallic nanorods as employed in this study the use of single particles provides even better sensitivities than the self-assembled dimers, despite the very thin coatings employed here. In particular, we find that individual gold nanorods with an optimized aspect ratio of 3-4 exhibit the highest figure-of-merit among the structures compared here due to a favorable compromise between accessibility of the plasmon's mode volume and sensitivity.

References

1. Becker, J.; Trügler, A.; Jakab, A.; Hohenester, U.; Sönnichsen, C. The optimal aspect ratio of gold nanorods for plasmonic bio-sensing. *Plasmonics*, **2010**, *5*, 161-167.
2. Nusz, G. J.; Curry, A. C.; Marinakos, S. M.; Wax, A.; Chilkoti, A. Rational selection of gold nanorod geometry for label-free plasmonic biosensors. *ACS Nano*, **2009**, *3*, 795-806.
3. Zijlstra, P.; Paulo, P. M. R.; Orrit, M. Optical detection of single non-absorbing molecules using the surface plasmon resonance of a gold nanorod. *Nat. Nanotechnol.*, **2012**, *7*, 379-382.
4. Ament, I.; Prasad, J.; Henkel, A.; Schmachtel, S.; Sönnichsen, C. Single unlabeled protein detection on individual plasmonic nanoparticles. *Nano Lett.*, **2012**, *12*, 1092-1095.
5. Beuwer, M. A.; Prins, M. W. J.; Zijlstra, P. Stochastic protein interaction monitored by hundreds of single-molecule plasmonic biosensors. *Nano Lett.*, **2015**, *15*, 3507-3511.
6. Taylor, A. B.; Zijlstra, P. Single-molecule plasmon sensing: current status and future prospects. *ACS Sens.*, **2017**, *2*, 1103-1122.
7. Zijlstra, P.; Orrit, M. Single metal nanoparticles: optical detection, spectroscopy and applications. *Rep. Prog. Phys.*, **2011**, *74*, 106401.
8. Kottmann, J. P.; Martin, O. J. F.; Smith, D. R.; Schultz, S. Non-regularly shaped plasmon resonant nanoparticle as localized light source for near-field microscopy. *Journal of Microscopy* **2001,** *202*, 60-65.
9. Chen, H.; Kou, X.; Yang, Z.; Ni, W.; Wang, J. Shape- and size-dependent refractive index sensitivity of gold nanoparticles. *Langmuir*, **2008**, *24*, 5233-5237.
10. Taylor, A. B.; Siddiquee, A. M.; Chon, J. W. M. Below melting point photothermal reshaping of single gold nanorods driven by surface diffusion. *Nanoscale*, **2004**, *8*, 12071-12079.
11. Prodan, E.; Radloff, C.; Halas, N. J.; Nordlander, P. A hybridization model for the plasmon response of complex nanostructures. *Science*, **2003**, *203*, 419-422.
12. Nordlander, P.; Oubre, C.; Prodan, E.; Li, K.; Stockman, M. I. Plasmon hybridization in nanoparticle dimers. *Nano Lett.*, **2004**, *4*, 899-903.
13. Jain, P. K.; El-Sayed, M. A. Universal scaling of plasmon coupling in metal nanostructures: Extension from particle pairs to nanoshells. *Nano Letters* **2007,** *7* (9), 2854-2858
14. Rechberger, W.; Hohenau, A.; Leitner, A.; Krenn, J. R.; Lamprecht, B.; Ausenegg, F. R. Optical properties of two interacting gold nanoparticles. *Opt. Commun.*, **2003**, *220*, 137-141.
15. Fong, K. E.; Yung, L-Y. L. Localized surface plasmon resonance: a unique property of plasmonic nanoparticles for nucleic acid detection. *Nanoscale*, **2013**, *5*, 12043-12071.
16. Myroshnychenko, V.; Rodríquez-Fernández, J.; Pastoriza-Santos, I.; Funston, A. M.; Novo, C.; Mulvaney, P.; Liz-Marzán, L. M.; García de Abajo, F. J. Modelling the optical response of gold nanoparticles. *Chem. Soc. Rev.*, **2008**, 37, 1792-1805.
17. Chen, J. I. L.; Chen, Y.; Ginger, D. S. Plasmonic nanoparticle dimers for optical sensing of DNA in complex media. *J. Am. Chem. Soc.*, **2010**, *132*, 9600-9601.
18. Yoon, J. H.; Selbach, F.; Schumacher, L.; Jose, J.; Schlücker, S. Surface plasmon coupling in dimers of gold nanoparticles: experiment and theory for ideal (spherical) and nonideal (faceted) building blocks. *ACS Photonics*, **2019**, *6*, 641-648.
19. Yim, T-J.; Wang, Y.; Zhang, X. Synthesis of a gold nanoparticle dimer plasmonic resonator through two-phase-mediated functionalization. *Nanotechnology*, **2008**, *19*, 435605.
20. Punj, D.; Regmi, R.; Devilez, A.; Plauchu, R.; Moparthi, S. B.; Stout, B.; Bonod, N.; Rigneault, H.; Wenger, J. Enhanced single-molecule fluorescence detection at micromolar concentrations. *ACS Photonics*, **2015**, *2*, 1099-1107.
21. Dhawan, A.; Norton, S. J.; Gerhold, M. D.; Vo-Dinh, T. Comparison of FDTD numerical computations and analytical multipole expansion method for plasmonics-active nanosphere dimers. *Opt. Express*, **2009**, *17*, 9688-9703.
22. Luo, D.; Shi, B.; Zhu, Q.; Qian, L.; Qin, Y.; Xie, J. Optical properties of Au-Ag nanosphere dimer: influence of interparticle spacing. *Opt. Commun.*, **2020**, *458*, 124746.
23. Hatef, A.; Meunier, M. Plasma-mediated photothermal effects in ultrafast laser irradiation of gold nanoparticle dimers in water. *Opt. Express*, **2015**, *23*, 1967-1980.
24. Aćimović, S. S.; Kreuzer, M. P.; González, M. U.; Quidant, R. Plasmon near-field coupling in metal dimers as a step toward single-molecule sensing. *ACS Nano*, **2009**, *3*, 1231-1237.

25. Li, S.; He, J.; Xu, Q-H. Aggregation of metal-nanoparticle-induced fluorescence enhancement and its application in sensing. *ACS Omega*, **2020**, *5*, 41-48.
26. Thacker, V. V.; Herrmann, L. O.; Sigle, D. O.; Zhang, T.; Liedl, T.; Baumberg, J. J.; Keyser, U. F. DNA origami based assembly of gold nanoparticle dimers for surface-enhanced Raman scattering. *Nat. Commun.*, **2014**, *5*, 3448.
27. Mercadal, P. A.; Encina, E. R.; Coronado, E. A. Colloidal SERS substrate for the ultrasensitive detection of biotinylated antibodies based on near-field gradient within the gap of Au nanoparticle dimers. *J. Phys. Chem. C*, **2019**, *123*, 23577-23585.
28. Funston, A. M.; Novo, C.; Davis, T. J.; Mulvaney, P. Plasmon coupling of gold nanorods at short distances in different geometries. *Nano Lett.*, **2009**, *9*, 1651-1658.
29. Slaughter, L. S.; Wu, Y.; Willingham, B. A.; Nordlander, P.; Link, S. Effects of symmetry breaking and conductive contact on the plasmon coupling in gold nanorod dimers. *ACS Nano*, **2010**, *4*, 4657-4666.
30. Wu, J.; Lu, X.; Zhu, Q.; Zhao, J.; Shen, Q.; Zhan, L.; Ni, W. Angle-resolved plasmonic properties of single gold nanorod dimers. *Nano-Micro Lett.*, **2014**, *6*, 372-380.
31. Shao, L.; Woo, K. C.; Chen, H.; Jin, Z.; Wang, J.; Lin, H-Q. Angle- and energy resolved plasmon coupling in gold nanorod dimers. *ACS Nano*, **2010**, *4*, 3053-3062.
32. Sönnichsen, C.; Reinhard, B. M.; Liphardt, J.; Alivisatos, A. P., A molecular ruler based on plasmon coupling of single gold and silver nanoparticles. *Nat. Biotechnol.,* **2005,** *23* (6), 741-745.
33. Reinhard, B. M.; Siu, M.; Agarwal, H.; Alivisatos, A. P.; Liphardt, J. Calibration of dynamic molecular rulers based on plasmon coupling between gold nanoparticles. *Nano Lett.*, **2005**, *5(11)*, 2246-2252.
34. Tabor, C.; Murali, R.; Mahmoud, M.; El-Sayed, M. A. On the use of plasmonic nanoparticle pairs as a plasmon ruler: the dependence of the near-field dipole plasmon coupling on nanoparticle size and shape. *J. Phys. Chem. A.*, **2009**, *113*, 1946-1953.
35. Woo, K. C.; Shao, L.; Chen, H.; Liang, Y.; Wang, J.; Lin, H-Q. Universal scaling and Fano resonance in the plasmon coupling between gold nanorods. *ACS Nano,* **2011**, *5(7)*, 5976-5986.
36. Sun, Z.; Ni, W.; Kou, X.; Li, L.; Wang, J. pH-controlled reversible assembly and disassembly of gold nanorods. *Small*, **2008**, *4*, 1287-1292.
37. Hohenester, U.; Trügler, A. MNPBEM – a Matlab toolbox for the simulation of plasmonic nanoparticles. *Comp. Phys. Commun.*, **2012**, *183*, 370-381.
38. Waxenegger, J.; Trügler, A.; Hohenester, U. Plasmonic simulations with the MNPBEM toolbox: consideration of substrates and layer structures. *Comp. Phys. Commun.*, **2015**, *193*, 138-150.
39. Koohyar, F.; Rostami, A. A.; Chaichi, M. J.; Kiani, F. Study on thermodynamic properties for binary systems of water + L-cysteine hydrochloride monohydrate, glycerol, and d-sorbitol at various temperatures. *J. Chem.,* **2013**, 2013, 601751.
40. Kumar, J.; Wei, X.; Baroow, S.; Funston, A. M.; Thomas, K. G.; Mulvaney, P. Surface plasmon coupling in end-to-end linked gold nanorod dimers and trimers. *Phys. Chem. Chem. Phys.*, **2013**, *15*, 4258-4264.
41. Aćimović, S. S.; Kreuzer, M. P.; González, M. U.; Quidant, R. Plasmon near-field coupling in metal dimers as a step toward single-molecule sensing. *ACS Nano*, **2009**, *3(5)*, 1231-1237.
42. Cheng, Y.; Wang, M.; Borghs, G.; Chen, H. Gold nanoparticle dimers for plasmon sensing. *Langmuir*, **2011**, *27* 7884-7891.
43. Kawasaki, T.; Zhang, H.; Nishi, H.; Mulvaney, P.; Tatsuma, T. Potential-scanning localized plasmon sensing with single and coupled gold nanorods. *J. Phys. Chem. Lett.*, **2017**, *8*, 3637-3641.
44. Hazarika, P.; Ceyhan, B.; Niemeyer, C. M. Reversible switching of DNA-gold nanoparticle aggregation. *Angew. Chem. Int. Ed.*, **2004**, *116*, 6631-6633.
45. Li, C.; Li, S.; Qu, A.; Kuang, H.; Xu, L.; Xu, C. Directnig arrowheid nanorod dimers for microRNA in situ Raman detection in living cells. *Adv. Funct. Mater.*, **2020**, *30*, 2001451.
46. Kar, A.; Thambi, V.; Paital, D.; Joshi, G.; Khatua, S. Synthesis of solution-stable end-to-end linked gold nanorod dimers via pH-dependent surface reconfiguration. *Langmuir*, **2020**, *36*, 9894-9899.
47. Cheng, L.; Song, J.; Yin, J.; Duan, H. Self-assembled plasmonic dimers of amphiphilic gold nanocrystals. *J. Phys. Chem. Lett.*, **2011**, *2*, 2258-2262.

Chapter 6

Conclusions and Outlook

In this thesis, nanoscale assemblies at a glass-fluid interface have been investigated using correlative microscopy. Combining the imaging of sample topography using atomic force microscopy with different optical techniques has expanded the toolset to study a wide range of systems on the nanoscale. Especially because of the ability to easily shift between total internal reflection fluorescence microscopy, total internal reflection scattering microscopy and hyperspectral imaging. In this chapter we discuss the main results and conclusions of this thesis and give recommendations for future research in an outlook.

6.1 Summary of the main results

Chapter 2: peak force tapping mode is best suited for soft samples due to its direct force control. In chapter 2 we discuss multimodal correlated microscopy where we combine atomic force microscopy with multiple optical techniques to nanoscale systems. For soft samples contact force is no option due to its lateral forces and high normal forces as the tip is continuously in contact with the sample. For non-contact mode and tapping mode, where the cantilever is oscillated, lateral forces are eliminated, but high normal forces are still present when the tip intermittently contacts the surface (tapping mode) or when the tip snaps into the surface (non-contact mode). This is especially true for samples with lots of variation in height. In peak force tapping mode the maximum force is used as a feedback mechanism which minimizes sample deformation and damage.

Chapter 2: hyperspectral imaging is a high-throughput method easily implemented into a correlated microscopy setup. Spectroscopy techniques are vital in the understanding of optical properties of nanoscale molecules and particles, such as metal nanoparticles or fluorescent dyes. Measuring spectra with commonly used techniques is often time consuming, because only one particle at the time is measured (i.e. in a spectrometer), or requires low density samples and a split field of view (i.e. measurements with a grating in front of the camera). Other methods, such as Fourier transform spectroscopy, where the emitted light is split and the length of one beam is varied causing interference between the two beams, are also time consuming. On the other hand, hyperspectral imaging is easily implemented into an existing setup by adding a filter wheel. Monitoring the intensity of single particles or molecules on the sample at various wavelength when the emitted signal passes through a narrow-bandwidth filter provides spectral data of all particles in the field of view. This makes the method high-throughput and ideal for the gathering of statistics of single molecule or particle samples.

Chapter 3: when determining mechanical properties of supramolecular polymers with polymer-to-polymer variation, correlated microscopy is an ideal tool for analysis. AFM imaging of BTA polymers shows a fraction in clustered or entangled states. Analysis of all polymers with AFM is time consuming, because of the limited AFM scanning speed. Furthermore, supramolecular BTA polymers are soft and therefore easily deformed or damaged making analysis of their structure challenging using AFM. Correlating AFM topography of fluorescently labeled single polymers to their fluorescent images shows entanglement and clustering results locally in higher fluorescence intensity. Analysis of fluorescence intensity along the polymer allows us to separate single unentangled polymers from entangled and clustered ones. From these single polymers the persistence length is then determined. Analysis of the full dataset shows a higher persistence length due to entanglement and clustering showing the necessity of single polymer measurements and correlation with AFM.

Chapter 4: In plasmonic sensing the plasmon shift depends strongly on the spatial overlap between the locally enhanced electric field and the analyte. In plasmonic sensing a change in the local refractive index results in a change in the nanoparticle plasmon energy. This energy change depends on nanoparticle dimensions and binding location. Near a curved surface or protrusion the near-field is enhanced, where higher curvature is equal to higher enhancement and a larger plasmon shift. This means that binding location is crucial. For a gold nanorod the near-field is strongest at the tip and if the local refractive index changes because of a binding event the change in plasmon energy may be detectable at the tip, but not at the side. This also depends on the medium, polarization of the excitation field and the size and composition of the bound analyte. When binding position and nanoparticle dimensions are known the change in plasmon energy provides information about the analyte allowing more detailed analysis. In chapter 4 we show that when correlating structural information using AFM, i.e. nanorod dimension and binding location, to plasmon shift, there is excellent agreement between measurements and calculations. The dominant contribution to the spread in the data is the size dispersion of the analyte, i.e. gold nanospheres. When the analyte is more uniform in shape and size dispersions in nanorod volume and aspect ratio become the most important contributions. Thus, correlated imaging of single particles will result in improved understanding of sensing experiments, which will lead to improvement of single-molecule sensing.

Chapter 5: the ratio between the intensity of the bonding and antibonding mode of nanorod dimers is the most accurate method to measure dimer angle optically. Nanorod dimers often self-assemble in an end-to-end configuration, with internal angles varying between 0 degrees (nanorods are almost bound side-to-side) and 180 degrees (actual end-to-end binding). The near-field intensity in the gap region and, as a result, the Figure of Merit, depend on this angle. BEM calculations show that the

bonding mode SPR energy slightly redshifts for increasing internal angle, whereas the antibonding mode SPR energy remains more or less constant. The ratio of the intensity scattered by the bonding mode and antibonding mode varies over more than two orders of magnitude when the dimer angle changes from 15 to 165 degrees. This makes this ratio a suitable method to estimate the dimer angle. AFM imaging of the dimer is a helpful method to check the accuracy of the optical measurement and to find the average nanorod dimensions and interparticle spacing.

Chapter 5: the strongly enhanced and confined near-field in the gap region of self-assembled metal nanoparticle dimers have a high sensitivity in theory, accessibility is often restricted due to the linkers involved in the self-assembly process. The plasmonic coupling of metal nanoparticles results in bonding and antibonding modes. When the bonding mode is excited the strongly enhanced near-field in the gap region is much stronger than the near-field of single nanoparticles. BEM calculations show an enhanced sensitivity for dimers compared to single nanoparticles. However, in the self-assembly of dimers the linker molecules (e.g. DNA, polyethylene glycol or cysteine) restrict the access of analytes to this gap region, effectively reducing the sensitivity. Here, calculations also show good agreement with a smaller than expected interparticle distance, contributing to lower accessibility.

This thesis highlights that, for assemblies where the particle-to-particle or molecule-to-molecule variations influence the properties of the assembly, information about particle or molecular structure is vital to the correct interpretation of measurements. Therefore, multimodal correlative microscopy is an ideal tool for nanoscale samples on interfaces.

6.2 Outlook

We provide several recommendations for future research to further the results obtained in this thesis. Here, we recommend additional extensions to the setup for future research such as correlative super-resolution microscopy and correlative microscopy with dynamic optical and spectral imaging, as well as a rational approach to studying the relation between structure and function in self-assembled nanomaterials.

6.2.1 Super-resolution correlative microscopy

In **Chapter 3** AFM was correlated to fluorescence microscopy to identify single unentangled supramolecular polymers. For this model system diffraction limited imaging was used for the quantification of the persistence length. The addition of

super-resolution microscopy will increase the resolution allowing for a more detailed analysis of samples.

The current setup as described in **Chapter 2** can be easily adapted for wide-field super-resolution techniques, such as stochastic optical reconstruction microscopy (STORM), which has been applied to the BTA supramolecular polymer model system to map the exchange dynamics of the monomers within the polymer using two different dyes.[1] With super-resolution imaging the structural information obtained from AFM can be linked to the chemical specificity of fluorescently-labeled molecules of interest with sub-diffraction-limited resolution.

Photo-activated localization microscopy (PALM) and STORM have been correlated to AFM measurements to study fluorescently-labeled DNA,[2] actin filaments,[3,4] and amyloid-like fibrils.[5] These correlative measurements generate insight in the composition of the sample, like the structure and composition of the sample, e.g. the number of filaments in a fibril or its helicity. The sub-diffraction limit resolution allows for improved resolution, providing more detailed and chemically specific information. STORM requires specific buffers for the on and off switching of the dyes, which was observed to interact with an AFM tip. This can be solved by the sequential optical and AFM imaging[6] or by optimization of the dye and buffer.[4]

Combining super-resolution microscopy with single-molecule spectroscopy opens up exciting new possibilities. Dong *et al*. correlate single molecule localization with sub-diffraction limit resolution to spectral imaging, resulting in combined super-resolution imaging of the position and spectrum of single molecules. By stochastically switching the dyes a super-resolution image is obtained.[7] Spectral imaging provides higher resolution compared to regular super-resolution localization techniques, because different dye species spaced closely together can be spectrally resolved with a high accuracy. The increased resolution results in the ability to resolve two closely spaced polymers, which would overlap when regular stochastic imaging is applied.[7] Finally, imaging multiple dyes in a single measurement is possible, even if their emission spectra overlap significantly, by ~55%.[7,8] Combining the multi-labelled spectroscopic photon localization microscopy of microtubules and mitochondria[7] or peroxisomes, vimentin filaments, microtubules and mitochondrial membrane[8] with AFM would provide a wealth of optical information in combination with structural information.

6.2.2 Dynamic correlative microscopy

In this thesis we focus on static measurements, but an interesting next step would be to probe dynamics. Supramolecular polymers are dynamic due to non-covalent

bonding; in BTA polymers monomers are exchanged along the full length of the polymer.[1] In plasmonic sensing, dynamics are also critical. Time-resolved imaging allows for the real-time monitoring of single-molecule binding events enabling the quantification of their binding dynamics.[9] Though the current setup is equipped to perform time-dependent optical microscopy, the current implementation for spectroscopy requires the exchange of wavelength filters which is relatively slow.

In literature, correlated temporally resolved super-resolution microscopy and AFM have been performed on live cells[3] and could be combined with high-speed[10] AFM to improve the temporal resolution. Furthermore, temporally-resolved spectral measurements have been performed on gold nanorods to measure their spectral shift on single-molecule binding events,[11] as well as to spectroscopically monitor gold nanoparticles growth.[12]

We propose to adapt our current setup to focus on combined temporally-resolved spectral and wide-field imaging with correlated AFM and combine the advantages of both techniques. For plasmonic sensing applications, this novel combination is achieved by adding a grating and imaging both wide-field total internal reflection scattering images and spectra on the same EMCCD camera. AFM measurements can be performed before and after to image the structural changes. Similarly, for fluorescently-labeled samples TIRF imaging and temporally-resolved spectral imaging are combined. Correlated temporal scattering and spectral imaging can be applied to image the dynamics of nanoparticle assemblies on surfaces, whereas correlated temporal TIRF and spectral imaging can be applied to the dynamic behaviour of dye-labeled self-assemblies.

6.2.3 Rational design to study structure-function relationships

In this thesis we study different structure-function relationships with correlated microscopy techniques. In **Chapter 3** we examined the structure of BTA polymers. Their dynamic structure, partly due to defects,[13] allows for monomer exchange along the full polymer length.[1] This leads to interesting properties related to their adaptivity, allowing for the reordering of monomers within the polymer, which can be applied for selective recognition of biomolecules.[14] Furthermore, the monomer structure, with the mostly hydrophobic side-chains and tunable end-groups, self-assembles into polymers that can be used for intracellular delivery, carrying both hydrophobic and charged compounds.[15]

In **Chapter 4** and **Chapter 5** we related the structure and conformation of nanoparticle dimers to their function. A change in binding location of a nanosphere on a gold nanorod results in large variations in plasmon shift, and can be applied in

sensing experiments. Information about binding location is vital when the aim is to gather information about the analyte from the plasmon shift. For nanorod dimers the binding conformation, i.e. dimer angle, determines the enhanced field strength in the gap region and as a result the sensitivity. However, accessibility can be restricted due to the linker molecules, limiting the functioning of the dimer as a high sensitivity sensor.

Due to limited information about the system, it is often difficult to predict the best structure for optimal function. Often optimization of the functional parameters of a self-assembled system is done by trial and error. The use of correlated microscopy allows for the correlation between optical, structural, and performance information. Such rational design may find value in a large variety of fields. Using the advancements in biotechnology and immunology genes can already be delivered by artificially constructed viruses[16] and particles are being designed for vaccine delivery.[17] The use of metallocyclic bonds allows to create tunable predetermined polygonal and polyhedral structures, where the shape can be engineered to fulfill a desired function.[18] In single particle sensing an analytical model predicts the molecular detection limit and the optimal nanoparticle dimensions for the analyte of interest.[19] The properties of DNA can be utilized to build three-dimensional structures to which active groups can be bound to fulfill a large range of applications.[20]

Applying our setup, where we are able to image structure using AFM, to the optical and spectroscopic quantification of new systems is an interesting new step. Correlative methods are an ideal tool to asses structure-function relationships and with information about both it is possible to apply rational design. We therefore believe that multi-model correlative microscopy will not only benefit fundamental studies of self-assembled materials, but its ability to unravel structure-function relationships will undoubtedly accelerate applications of these tiny nanostructures

References

1. Albertazzi, L.; Van der Zwaag, D.; Leenders, C. M. A.; Fitzner, R.; Van der Hofstad, R. W.; Meijer, E. W. Probing exchange pathways in one-dimension aggregates with super-resolution microscopy. *Science*, **2014**, *344*, 491-495.
2. Monserrate, A.; Casado, S.; Flors, C. Correlative atomic force microscopy and localization-based super-resolution microscopy: revealing labelling and image reconstruction artefacts. *ChemPhysChem*, **2014**, *15*, 647-650.
3. Odermatt, P. D.; Shivanandan, A.; Deschout, H.; Jankele, R.; Nievergelt, A. P.; Feletti, L.; Davidson, M. W.; Radenovic, A.; Fantner, G. E. High resolution correlative microscopy: bridging the gap between single molecule localization microscopy and atomic force microscopy. *Nano Lett.*, **2015**, *15*, 4896-4904.
4. Hirvonen, L. M.; Cox, S. STORM without enzymatic oxygen scavenging for correlative atomic force and fluorescence superresolution microscopy. *Methods Appl. Fluores.*, **2018**, *6*, 045002.
5. Bondia, P.; Jurado, R.; Casado, S.; Domínguez-Vera, J. M.; Gálvez, N.; Flors, C. Hybrid nanoscopy of hybrid nanomaterials. *Small*, **2017**, *13*, 1603784.
6. Gómez-Varela, A. I.; Stamov, D. R.; Miranda, A.; Alves, R.; Barata-Antunes, C.; Dambournet, D.; Drubin, D. G.; Paiva, S.; De Beule, P. A. A. Simultaneous co-localized super-resolution fluorescence microscopy and atomic force microscopy: combined SIM and AFM platform for the life sciences. *Sci. Rep.*, **2020**, *10*, 1122.
7. Dong, B.; Almassalha, L.; Urban, B. E.; Nguyen, T-Q.; Khuon, S.; Chew, T-L.; Backman, V.; Sun, C.; Zhang, H. F. Super-resolution spectroscopic microscopy via photon localization. *Nat. Commun.*, **2016**, *7*, 12290.
8. Zhang, Z.; Kenny, S. J.; Hauser, M.; Li, W.; Xu, K. Ultrahigh-throughput single-molecule spectroscopy and spectrally resolved super-resolution microscopy. *Nat. Methods*, **2015**, *12*, 935-938.
9. Beuwer, M. A.; Prins, M. W. J.; Zijlstra, P. Stochastic protein interactions monitored by hundreds of single-molecule plasmonic biosensors. *Nano Lett.*, **2015**, *15*, 3507-3511.
10. Kodera, N.; Yamamoto, D.; Ishikawa, R.; Ando, T. Video imaging of walking myosin V by high-speed atomic force microscopy. *Nature*, **2010**, *468*, 72-76.
11. Ament, I.; Prasad, J.; Henkel, A.; Schmachtel, S.; Sönnichsen, C. Single unlabeled protein detection on individual plasmonic nanoparticles. *Nano Lett.*, **2012**, *12*, 1092-1095.
12. Becker, J.; Schubert, O.; Sönnichsen, C. Gold nanoparticle growth monitored in situ using a novel fast optical single-particle spectroscopy method. *Nano Lett.*, **2007**, *7*, 1664-1669.
13. Baker, M. B.; Albertazzi, L.; Voets, I. K.; Leenders, C. M. A.; Palmans, A. R. A.; Pavan, G. M.; Meijer, E. W. Consequences of chirality on the dynamics of a water-soluble supramolecular polymer. *Nat. Commun.*, **2015**, *6*, 6234.
14. Albertazzi, L.; Martinez-Veracoechea, F. J.; Leenders, C. M. A.; Voets, I. K.; Frenkel, D.; Meijer, E. W. Spatiotemporal control and superselectivity in supramolecular polymers using multivalency. *Proc. Natl. Acad. Sci. U.S.A.*, **2013**, *110*, 12203-12208.
15. Bakker, M. H.; Lee, C. C.; Meijer, E. W.; Dankers, P. Y. W.; Albertazzi, L. Multicomponent supramolecular polymers as a modular platform for intracellular delivery. *ACS Nano*, **2016**, *10*, 1845-1852.
16. Miyata, K.; Nishiyama, N.; Kataoka, K. Rational design of smart supramolecular assemblies for gene delivery: chemical challenges in the creation of artificial viruses. *Chem. Soc. Rev.*, **2012**, *41*, 2562-2574.
17. Gause, K. T.; Wheatley, A. K.; Cui J.; Yan, Y.; Kent, S. J.; Caruso, F. Immunological principles guiding the rational design of particles for vaccine delivery. *ACS Nano*, **2017**, *11*, 54-68.
18. Stang, P. J.; Olenyuk, B.; Self-assembly, symmetry, and molecular architecture: coordination as the motif in the rational design of supramolecular metallacyclic polygons and polyhedral. *Acc. Chem. Res.*, **1997**, *30*, 502-518.
19. Nusz, G. J.; Curry, A. C.; Marinakos, S. M.; Wax, A.; Chilkoti, A. Rational selection of gold nanorod geometry for label-free plasmonic biosensors. *ACS Nano*, **2009**, *3*, 795-806.

20. Feldkamp, U.; Niemeyer, C. M. Rational design of DNA nanoarchitectures. *Angew. Chem. Int. Ed.*, **2006**, *45*, 1856-1876.

About the author

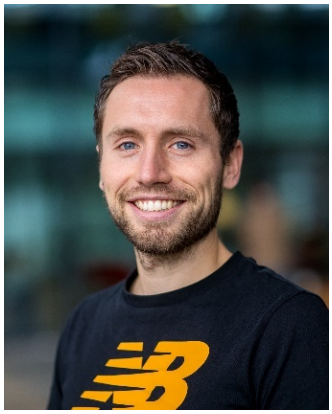

Michael Beuwer was born as the son of Alfred Beuwer and Ellen Beuwer-Hondeveld on the 4th of December 1991 in Eindhoven, the Netherlands. Together with his younger sister Daisy he grew up in Eindhoven and attended primary school St. Antonius Abt in Acht. He completed his secondary education in Eindhoven in 2008 at the Stedelijk College Eindhoven, where he followed a bilingual program, obtaining an IGSCE diploma in five subjects, as well as an IB diploma in English. The profile 'Nature and Technology' allowed him to pursue a scientific study, which led him to enroll at the Eindhoven University of Technology.

Michael obtained his Bachelor's (2011) and Master's degree (2013) in Applied Physics, where he followed the 'Functional Nano Materials' track. During his Master's program, Michael completed an external internship at Yale University in the Enrique M. De La Cruz Lab on the flexibility of myosin-bound actin molecules. His graduation project at the Molecular Biosensing for Medical Diagnostics (MBx) group was on plasmonic single-molecule detection, focusing on high-throughput detection by monitoring hundreds of gold nanorods at once. During his Bachelor studies Michael worked a side job performing and explaining physics experiments for first-year students.

In October 2013, he started his PhD in the MBx group under the supervision of dr. ir. Peter Zijlstra as a member of the Institute for Complex Molecular Systems. During his PhD, he worked on correlated microscopy of nanoscale assemblies on interfaces, combining and correlating optical and atomic force microscopy to study supramolecular polymers and gold nanoparticle dimers. The main results of the work during his PhD are summarized in this thesis.

List of publications

Journal papers

- **Beuwer, M.A.**; Zijlstra, P. Self-assembled dimers for refractive-index sensing - *in preparation as a manuscript*

- **Beuwer, M.A.**; Van Hoof, B.; Zijlstra, P. Spatially resolved sensitivity of single-particle plasmon sensors. *J. Phys. Chem. C*, **2018**, *122 (8)*, 4615-4621.

- Taylor, A.B.; Verhoek, R.; **Beuwer, M.A.**; Wang, Y.; Zijlstra, P. All-optical imaging of gold nanoparticle geometry using super-resolution microscopy. *J. Phys. Chem. C*, **2018**, *122* (4), 2336-2342.

- **Beuwer, M.A.**; Knopper, M.F.; Albertazzi, L.; Van der Zwaag, D.; Ellenbroek, W.G.; Meijer, E.W.; Prins, M.W.J.; Zijlstra, P. Mechanical properties of single supramolecular polymers from correlative AFM and fluorescence microscopy. *Polym. Chem.*, **2016**, *7 (47)*, 7260-7268.

- **Beuwer, M.A.**; Prins, M.W.J.; Zijlstra, P. Stochastic protein interactions monitored by hundreds of single-molecule plasmonic biosensors. *Nano Lett.*, **2015**, *15 (5)*, 3507-3511.

Conference presentations

- **Eindhoven Multiscale Institute Symposium 2017** (oral) - Mechanical properties of single supramolecular polymers from correlative AFM and fluorescence microscopy
- **FOM Physics 2017** (poster) - Mechanical properties of single supramolecular fibers from correlative AFM and TIRF microscopy
- **Dutch Biophysics 2016** (oral) – Mechanical properties of single supramolecular polymers from correlative AFM and fluorescence microscopy
- **Physics meets Biology 2015** (poster) - Mechanical Properties of Single Supramolecular Fibers from Correlative AFM and Fluorescence Microscopy
- **Dutch Biophysics 2015** (oral) – Mechanical properties of single supramolecular polymers from correlative AFM and fluorescence microscopy
- **Nanocity 2015** (oral) – Mechanical properties of single supramolecular polymers from correlative AFM and fluorescence microscopy
- **Dutch Biophysics 2014** (poster) – Correlated fluorescence and AFM imaging of supramolecular fibers

Acknowledgements

This thesis marks the end of a period. One that was a bit longer than anticipated, but one that was full of both challenging and great moments, all of which have contributed to me being a different person than I was when I started. In this section I would like to express my gratitude to all the people that were there along the way.

First of all, I would like to thank all the committee members for taking the time to critically read and review my thesis and for being part of the PhD committee.

Secondly, and most importantly, I want to thank you, Peter. When you joined the MBx group I was your first Master's student and later I was also the first to start a PhD under your supervision. Though things did not always go the way I (and probably you) wanted to, you always had another suggestion, another angle and another idea to fix any trouble that lay ahead. Thank you for your patience, your advice and all your help during the past years. Also, lots of success and luck for the coming years, in which I'm certain you'll continue to grow as an excellent scientist and mentor.

Menno, as my co-promotor and group leader, I'd like to thank you for creating and maintaining an excellent group with a great atmosphere. In our meetings, I especially valued your ability to always boost my morals with your can-do-attitude combined with some great metaphors.

For the Chapter on correlative microscopy on the BTA polymers I would like to thank Daan and Lorenzo for their help with the very tricky polymers and Wouter for his analysis of the persistence length.

The MBx staff – Leo, Arthur, Lorenzo, Khulan and of course Claudia, I'd like to thank for their input during the group meetings and discussions, but also for the colloquial conversations during lunch or a tea break. Especially Leo, with whom our shared interest for a wide range of sports was always a great conversation starter. Thanks to Claudia and Arthur as well for their help on all matters related to the chemical lab and to Claudia especially for exchanging tips (pun intended) on how to get the AFM to work the way we wanted it to.

During my PhD there have been a lot of PhD students in the group. I was welcomed by Matthias, Fabiola, Stefano, Emiel and Roland. They helped me getting started, especially Emiel, who was also an office mate at the time. Later Christian, Yuyang,

Matěj and Max started, and in the end also Rafiq, Tina, Laura, Paul, Sjoerd, Natalia, Laura W., Roger and Manos joined, increasing the group size and of course the atmosphere. Adam, Rachel and Junhong joined as postdocs, and were always available for any questions. Thanks you all! I specifically want to thank Yuyang, Matěj and Rachel, for all their help with anything related to plasmonics. Thank you Rachel as well for being a great lunch buddy and all our conversations ranging from American politics to sports. And thank you Matěj, for being a great neighbor in the office!

During my PhD I also supervised four students. Daan, Stan, Floris, Bas, thank you for your contributions to my research and this thesis!

Ik wil ook graag de personen bedanken die niet inhoudelijk bij hebben gedragen maar wel enorm belangrijk waren tijdens de afgelopen jaren. Zoals iedereen weet is hardlopen mijn grootste hobby en naast mijn promotie was het eerst bij Asterix en later bij Eindhoven Atletiek dan ook altijd een heerlijke uitlaatklep om samen te trainen en te lopen. Marco, met wie ik een groot deel van mijn promotie bijna alle trainingen samen heb gedaan, mijn mede-bestuursleden Joep, Sander, Kees, Yorma en Tomas, en natuurlijk iedereen van Archaix wil ik dan ook graag bedanken voor alle heerlijke gelopen kilometers en de vele uren die we niet lopend doorbrachten. Zeker met Joep, Sander en Mark ontspoorden onze gesprekken en ideeën altijd enorm. Tijdens deze jaren heb ik ook Ben leren kennen. Wat begon met een wederzijdse interesse in hardlopen werd een vriendschap én een partnerschap als eigenaars van Gewoon Lekker Rennen. Vanaf onze trip naar Schotland werd al snel duidelijk dat zelfs voedseltekort, bergen en kapotte voeten ons enthousiasme niet kon inperken. Gewoon Lekker Rennen is daarnaast ook altijd een hele mooie toevoeging geweest, het was en is genieten om mijn enthousiasme voor het hardlopen te kunnen overbrengen. Ook daaruit zijn inmiddels mooie vriendschappen ontstaan!

Als laatste wil de personen bedanken die me altijd onvoorwaardelijk hebben gesteund in mijn beslissingen. Natuurlijk mijn ouders, dank jullie dat jullie altijd voor me klaar staan en me altijd hebben ondersteund, dat waardeer ik enorm. Daisy, ik ben heel blij dat je zo gegroeid bent en jezelf weer bent geworden, en dat je dat met mij hebt gedeeld. En natuurlijk Stefanie, je hebt vooral de laatste loodjes meegemaakt, maar dat hielp enorm. Ik ben enorm blij met jou!